Search for light dark matter using the resonant cavity in the frequency under 500 MHz

Dissertation

zur Erlangung des Doktorgrades

des Department Physik
der Universität Hamburg

vorgelegt von

Le Hoang Nguyen

aus Saigon (Vietnam)

Hamburg 2018

Gutachter der Dissertation:	Prof. Dr. Dieter Horns Dr. Andrei Lobanov
Zusammensetzung der Prüfungskommission:	Prof. Dr. Dieter Horns Prof. Dr. Grünter Sigl Prof. Dr. Erika Garutti Prof. Dr. Caren Hanger Dr. Andrei Lobanov
Vorsitzende der Prüfungskommission:	Prof. Dr. Caren Hanger
Datum der Disputation:	26. April 2018
Vorsitzender Fach-Promotionsausschusses PHYSIK:	Prof. Dr. Wolfgang Hansen
Leiter des Fachbereichs PHYSIK:	Prof. Dr. Michael Potthoff
Dekan der Fakultät MIN:	Prof. Dr. Heinrich Graener

Abstract

In the recent years, the light dark matter particles or Weakly Interacting Slim Particles (WISPs) have received attention from the community as an alternative particle candidate for dark matter. Among this theoretical particle class are axions, axion-like-particles (ALPs), and hidden photons. The hidden photon is a well-motivated candidate for dark matter and retains a vast parameter space. With the goal to search for hidden photons, a new detection method was developed using the broadband radio-frequency acquisition to cover a large parameter space.

This thesis presents an experiment using the haloscope resonant cavity technique for the search for hidden photons in the unexplored mass range below 2.08 μeV named WISPDMX, the acronym for **W**eakly **I**nteracting **S**lim **P**artcle **D**ark **M**atter **Ex**periment. The experiment is located at the Institut für Experimentalphysik of Hamburg Universität, Hamburg. The experiment consists of a refurbished accelerator resonant cavity, two modified tuning plungers, and a unique real-time acquisition system. At the moment, the readout system of WISPDMX can return the broadband spectrum up to 500 MHz with a very high resolution (50 Hz). In the first science run, WISPDMX is able to detect a signal at the power level of 10^{-20} Watt/$\sqrt{\text{Hz}}$.

WISPDMX is the very first haloscope type experiments searching for hidden photon and possible light dark matter candidates. Thus the theoretical foundation for such kind of experiment has to be studied such as the power developed inside the hidden photon haloscope resonator. Extended studies of the expected linewidth of the hidden photons conversions and of the broadband gain are carried out.

With the fully functional experiment, the first science run of WISPDMX has been executed from 23rd October 2017 to 2nd November 2017, with the total acquisition time is 61.1 hours. An algorithm for the signal scan was developed for different ranges and applied to the instantaneous and time-averaged spectra.

Finally, the result from the first science run of WISPDMX is presented and demonstrates that WISPDMX is currently the most sensitive experiment in the allowed parameter ranges of the hidden photon.

Kurzfassung

Schwach wechselwirkende leichte Teilchen (Engl. Weakly Interacting Slim Particles (WISPs) sind als alternative Kandidaten für dunkle Materie in den vergangenen Jahren näher in den Blickpunkt gerückt. Zu diesen Teilchen zählen Axionen, unter diesen Teilchen sind Axionen, Axion-ähnliche Teilchen (Axion-like particles, ALPs) und versteckte Photonen (Hidden Photons, HP). Das versteckte Photon ist ein gut motivierter Kandidat für dunkle Materie und deckt einen breiten Parameterraum ab. Mit dem Ziel nach versteckten Photonen zu suchen, wurde eine neue, breitbandige Detektionsmethode entwickelt.

Diese Arbeit befasst sich mit einem Experiment, das die Haloskop-Resonanztechnik verwendet, um nach versteckten Photonen im bisher nicht untersuchten Massenbereich unterhalb 2.08 μeV zu suchen: WISPDMX (Weakly Interacting Slim Particle Dark Matter Experiment). Das Experiment befindet sich am Institut für Experimentalphysik der Universität Hamburg. Es besteht aus einem wiederverwendeten Hohlraumresonator, der mit zwei mechanischen Vorrichtungen zur Frequenzeinstellung und einem einzigartigen Echtzeit-Datennahmesystem betrieben wird. Zum heutigen Zeitpunkt kann das Auslesesystem von WISPDMX ein Breitbandspektrum bis zu einer Frequenz von 500 MHz mit einer guten Auflösung von 50 Hz aufnehmen. Mit der ersten Datennahmeperiode (1st science run) ist dieses System ist in der Lage, ein Signal mit einem Leistungslevel von 10^{-20} Watt/$\sqrt{\text{Hz}}$ zu detektieren.

WISPDMX ist eines der ersten Haloskop-Experimente für die Suche nach versteckten Photonen. Daher müssen die technisch-experimentellen Grundlagen, wie die im Haloskop-Resonator entwickelte Leistung bei Konversion eines versteckten Photons, untersucht werden. Umfangreiche Studien der erwarteten Linienbreite konvertierter versteckter Photonen und der Breitbandverstärkung wurden ausgeführt.

Mit einem voll einsatzbereiten Experiment wurde die erste wissenschaftliche Datennahme mit einer Gesamtdauer von 61.1 Stunden zwischen dem 23ten Oktober und

dem 2ten November durchgeführt. Ein Algorithmus für eine Signalsuche (signalscan) wurde für unterschiedliche Frequenzbereiche entwickelt und auf die instantanen (Einzelspektren) und zeit-gemittelten Spektren angewendet.

Schließlich wird die Auswertung der ersten Datennahme von WISPDMX vorgestellt. Die Ergebnisse demonstrieren, dass WISPDMX derzeit das empfindlichste Experiment zum Nachweis versteckter Photonen im erlaubten Parameterraum ist.

"Empty your mind. Be formless, shapeless like water. Now you put water into a cup, it becomes the cup. You put water into a bottle, it becomes the bottle. You put water in a teapot, it becomes the teapot. Now water can flow or it can crash. Be water my friend."

Bruce Lee

To my brother, Nguyen Le Hai.

Contents

Chapter 1

From Dark Matter to Hidden Photon

Abstract

This chapter will present a brief introduction to the concept of dark matter, its general characteristics, and one of the light dark matter particle candidates: the hidden photon. Section 1.1 will discuss briefly the observational evidence for the existence of dark matter, ranging from interplanetary-scale to universe-scale. In section 1.2 the three classes of dark matter candidates which are suggested in models beyond the standard model of particle physics will be dicussed. Section 1.3 will present the direct and indirect search method for dark matter particles which depend on the distribution of dark matter in the Galaxy. The two last sections will present the properties of the hidden photons, related experiments, and observations.

1.1 On the Properties of Dark Matter

1.1.1 Origin of Dark Matter Concept

The term "Dark Matter" was firstly introduced by Fritz Zwicky in the early 1930s. Zwicky was the first one to apply the virial theorem to estimate the total mass of the Coma Cluster [1]. The variance of projection velocities of visible matter (stars,

galaxies) in the Coma cluster is measured via spectral measurements. Under the assumption that the structure is in virial equilibrium, one can then determine the mass of the structure:

$$M = \frac{\sigma^2 R}{G}, \tag{1.1}$$

where R is the radius of the structure, G is the gravitational constant. Zwicky's study shows that the total gravitational mass in the Coma cluster is about two orders of magnitude larger than the visible mass in galaxies. Therefore, Zwicky concluded, that an unknown and invisible form of matter exists in the Coma cluster.

Similar to the velocity dispersion measurement in the galaxy cluster, measurements on the rotational curves of the spiral galaxies show that the outer parts of the disk are rotating with an unexpected high velocity [2, 3]. This is contrary to the expected result from Newtonian gravitation where the velocity at the radius r should decline with increasing distance from the nucleus of the the galaxy:

$$v = \sqrt{\frac{GM(r)}{r}}, \tag{1.2}$$

where $M(r)$ is the mass contained in the sphere of radius r. Further studies on high luminosity spiral galaxies lead to the conclusion that the rotational curves are flat, at nucleus distances as great as 50 kpc [4, 5]. The profiles of the rotation curve show flat distributions as in Fig. 1.1. The high outer velocity shows that there exists an invisible mass distributed in the outer region of the spiral galaxies. The lack of visible mass is another evidence for dark matter and their halo which extends beyond the visible disk of the spiral galaxy.

Independent from the dynamical argument provided by the velocity dispersion and velocity curves, X-ray observations provide an additional insight into the gravitational properties and invisible mass of the cluster of galaxies. The intracluster medium maintains a hot-gas with temperature of $\sim 10^7 - 10^8$K visible in thermal X-ray emission. Studies on the distribution and temperature of the hot gas allow the determination of the gravitational potential of the cluster, and eventually, its total mass. These studies have shown that the mass of the hot gas in the cluster dominates over the mass of the stellar objects (stars and galaxies). However, the total observable mass is still not sufficient compared with the mass required to confine the hot gas [6–9]. Clusters of galaxies have typically a high fraction of

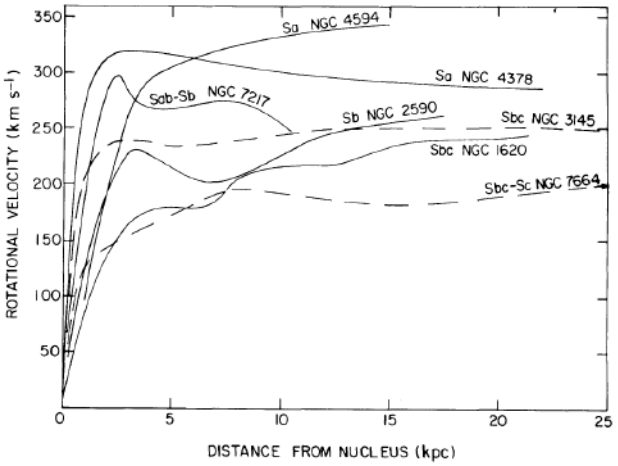

FIGURE 1.1: Rotational velocity curves of seven high-luminosity spiral galaxies. The rotational curves show flat profiles to large distances [5].

dark matter at $\sim 84\%$, hot gas of $\sim 14\%$ with the rest composed of stars and galaxies [9].

The gravitational lensing effect is a complementary probe of dark matter and cosmological models. Gravitational lensing observations are categorized into two types: strong lensing and weak lensing. In the case of strong lensing, multiple images are created or even the so-called Einstein's ring is formed when the source and the massive lens are located in the same line of sight of the observer. The first full ring was observed from B1938+666 where the mass of the lens inferred from the lensing is $\sim 2 \times 10^{10} M_{\odot}$ and much larger than the visible mass [10].

The weak lensing follows the statistical analysis of background objects in which their images are stretched due to the gravitational lensing from the matter distribution along the line of sight. Thus this method requires a large dataset in order to apply the statistical methods. The most well-known application, and also the most famous evidence for dark matter, is the Bullet cluster 1E 0657-558. The Fig. 1.2 (left) shows the two subclusters after collision. The mass distribution inferred from weak lensing (green contour) shows that the clumps of mass distribution follows the distribution of member galaxies. However, the X-ray mapping of the hot gas shows the bow shock, and the hot gas is separated by the ram-pressure-stripping during the collision [11]. The separation is possible if only the dominant mass is in the collisionless components which are the dark matter contents of the two subclusters [12].

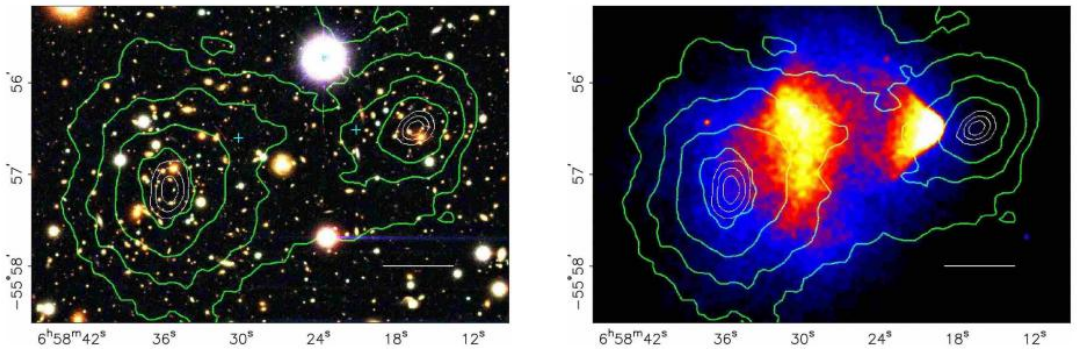

FIGURE 1.2: *Left*: Optical stellar components overlapped with green contours mapping representing the mass distribution obtained from gravitational lensing. *Right*: Gas distribution reconstructed from Chandra X-ray satellite, the centre of gas distribution could be determined and presented as the blue cross in the left image. Image from [12]

Lastly, on the cosmological scale, the cosmic microwave background (CMB [13]) observations provide evidence for the hot Big Bang and for dark matter [13]. The CMB photons represent the radiation coming directly from the epoch when matter and radiation decoupled. In the last four decades, observational satellites such as the COsmic Background Explorer (COBE - [14, 15]), the Wilkinson Microwave Anisotropy Probe (WMAP - [16]) and the recent Planck satellite have continuously refined their measurements of the CMB anisotropies. The result shows a near perfect black body spectrum with temperature of 2.726K with higher order anisotropies [16, 17]. The inflationary stage of the early Universe causes small fluctuations in the cosmic matter distribution. The fluctuations are predicted to increase by gravity and become the seed for the large scale structure. At the stage where the matter and radiation are coupled, traces of fluctuation in the matter distribution also prevails in the radiation distribution. The radiation fluctuation from gravity instabilities are visible as the CMB anisotropy. In the framework of the standard Big Bang cosmological model, as known as Lambda cold dark matter model (ΛCDM), the study on the power spectrum of the anisotropies provides an estimates of parameters of the ΛCMD. From the WMAP 9 Years Results [16] and Planck Satellite [18], the main parameters are listed in Table [1.1]

The component abundance $\Omega_i = \frac{\rho_i}{\rho_c}$ is the normalised ratio between the component density (ρ_i), and the critical density ($\rho_c = \frac{3H^2}{8\pi G}$). These parameters show that total matter content $\Omega_b + \Omega_c$ is dominated by cold non-baryonic dark matter since $\Omega_b \ll \Omega_c$. The study of CMB provides an additional method to understand the nature of dark matter and their abundance in the Universe.

TABLE 1.1: ΛCDM Parameters from WMAP 9 Years [16] and Planck 2015 Result [18]: the density of the baryonic matter, the density of non-baryonic matter, and the Hubble Constant. h is the reduced Hubble Constant defined as $H_0 = 100h$ km s^{-1} Mpc^{-1}.

	WMAP	**Planck**
$100\Omega_b h^2$	2.26 ± 0.04	2.21 ± 0.03
$100\Omega_c h^2$	11.46 ± 0.43	11.99 ± 0.27
H_0	68.0 ± 0.70	67.31 ± 0.96

In conclusion, there are properties required for a particle to be considered a candidate for the dark matter [19, 3]

- It has to have a finite mass.
- Dark matter must be non-baryonic from the CMB observations.
- It has a weak coupling with photon or even no coupling with the photon. However, under extreme conditions, like plasma resonance or magnetic field, the coupling between the dark matter and photon could be revealed.

Search for the dark matter particle is an effort that has been lasting for 70-80 years, but the identity of the particle is still unknown. Many theories have been proposed for the solution of the dark matter particle. In the following section, the possible extensions of the standard model of particle physics and its candidate particles are reviewed.

1.2 Dark Matter Particle Candidates

The standard model in particle physics (SM) is the theory describing three of the four known fundamental forces: electromagnetic, weak force, and strong force, but it does not include the gravitational interaction [20–22]. The Lagrangian of the SM contains all the kinetic terms defining the motions of the field, the mass terms to represent the particle masses, and coupling terms to describe the interaction between the particles. The SM explains the relationship between elementary particles and their interaction surprisingly accurate, hence make the SM the most successful physics theory. Still, there are problems with the SM. The SM can not provide a tool to approach the gravitational force, neutrinos mass, matter

anti-matter asymmetry, and does not include candidate particle for dark matter. Physicists are therefore forced to expand the SM model to include additional particles and invent theory beyond standard model (BSM): Supersymmetry (SUSY) is the most widely considered BSM theory with axions and the hidden sector.

1.2.1 Neutrino

On the explanation for the dark matter, the neutrino is the only candidate within the SM of particle physics that could satisfy the criteria introduced in the previous section. Neutrino oscillation experiments during the last three decades show that the neutrinos carry a small mass and could be the dark matter particles. However, the CMB observation gives a different constraint on the role of the neutrino in which it provides a much lower contribution to the density $100\Omega_\nu h^2 < 0.25$ [18]. The free streaming length of the neutrino dark matter does not support the large-scale structure. Observation shows the "bottom-up" formation in contrast with the "top-down" formation with the presence of neutrino dark matter.
A sterile neutrino is a theoretical particle which is connected to and can mix with the known SM neutrinos. The sterile neutrino has a mass that does not depend on the Higgs mechanism but a so-called Majorana mass. In particular, the Majorana mass can have an arbitrary scale that is very different from all other fermion masses. This lead to the case that the sterile neutrino could have a higher mass than the SM neutrino and solves the obstacles which SM neutrino can not.

1.2.2 Weakly Interacting Massive Particles (WIMP)

Supersymmetry (SUSY)relates between fermions and bosons, introducing a condition for each particle in the SM must have one or more "superpartner" with equal mass but with a spin different of 1/2 [23–27]. SUSY is one of the extensions of the SM that could be discovered at TeV-colliders or with astrophysical observations. Recent possible signals have been seen in observations with AMS-02 and Fermi-LAT [28]. Low-energy SUSY could support a stable supersymmetric particle that could play a role in explaining the dark matter in the universe. The lightest SUSY particles (LSP) is stable against its decay and thus becomes a candidate for dark matter[29]. The LSP is so-called a weakly interacting massive particle (WIMP).
The WIMPs can also arise from the extra-dimensional theory which is motivated

by string theory. However, as LHC has reached the TeV energy scale with upgrades in the statistical analysis method. Method and together with many decades of experiments and search techniques development, none of the SUSY or WIMPs have been detected.

1.2.3 Weakly Interacting Slim Particles

There is a hypothesis of an additional set of neutral SM particles but charged under a $U(1)$ symmetry. This set of particle is located in the *hidden sector*. The hidden sector field does not have sufficient similarity with the gauge group of the SM ($SU(3) \times SU(2) \times U(1)$) of the *visible sector*. The hidden sector is similar to a black box with limited interaction with the visible sector.
The hidden sector theory has been predicted in string theory or higher dimensional theory where the hidden field is located on the brane. Nevertheless, hidden sector theory remains irrelevant to the normal world, but in different contexts, the hidden sector could produce signatures that can be observed via high energy physics experiment and astrophysics.

- Visible sector and the hidden sector could interact via a messenger particle which makes the hidden sector detectable. A simple model of hidden sector contains an extra $U(1)$ gauge symmetry with the equivalent gauge boson. The messenger particle is the so-called hidden photon (γ').
- The visible sector field could be charged under the gauge field of the hidden sector. Thus would exist a "fifth force" (or dark force) interacting with the SM particles which are well-known.
- The hidden sector could have a completely different set of physical laws, which may appear hideous in comparison to SM physics.

The hidden sector is solely detectable via the messenger particle. In the simplest model, the hidden photon has a weak coupling with the SM field, effectively making this type of dark matter not detectable with classic experiment approaches.
The QCD axion, the theoretical pseudo-Nambu-Goldstone boson from the Peccei-Quinn solution to the strong CP problem [30–33], is a profoundly motivated particle candidate for the dark matter. In the early universe, cold axion populations arise from vacuum realignment in which Peccei-Quinn symmetry breaks before or

after the inflation. These cold axions were never in thermal equilibrium with the baryonic matter and could provide the dark matter.
Besides the QCD axions, other axion-like particles (ALPs) arise from various BSM models [34]. In these models, the ALPs are not necessarily related to the strong CP problem. Nevertheless, ALPs could couple to photons similar to axions. Differently from axions, mass and coupling constant of ALPs are not necessarily related to each other. In either astrophysical or laboratory conditions, searches for these particles share similar techniques.
The three types of particles previously mentioned: the hidden photon, axion, and ALP as grouped into a new particle class which is the so-called weakly interacting slim particles (WISPs).

1.3 Dark Matter Candidate Searches

In general, there are three methods currently employed in the experimental search for dark matter: direct detection, indirect detection, and collider searches.

1.3.1 Direct Dark Matter Searches

As described in further detail in section 1.3.4, the Earth travels through the dark matter halo of the Galaxy, the dark matter particle bombarding the Earth continuously. Direct dark matter search experiments look for the dark matter interaction with the ordinary matter in the detector, e.g., by measuring the elastic scattering between the dark matter particle and the nucleus of the target material. The signal event is expected to be rare because of the weakly interacting characteristic of the dark matter. Experiments with large target mass must be placed deep underground to reduce the background from cosmic rays (mostly neutrons produced in the interaction of cosmic rays and atmosphere, and they show similar signal as expected from dark matter). However, to unambiguously identify this low-energy interaction, a detailed knowledge of the signal signatures is needed [29, 35, 36].The rate of interaction depends on the dark matter density and its velocity distribution, as well as the outcome of scattering, which is model dependent. On the hardware side, the careful use of the radio-pure material is necessary to have low background noise.
For the last five decades, experiments have been constructed to look for the dark

matter signal from nuclear scattering. The null results of these experiments keep lowering the limit of the cross-section and widening the the particle mass range. XENON100 [37, 38], XENON1T [39], and CDMS-II [40] experiments have the highest mass for detection, they provide strong limit and constraints on spin-independent scattering, though the results are still null. DAMA (DAMA/LIBRA) in Italy [41, 42] presents the first evidence for the annual modulation and cumulatively reaches the significance of 9σ by observing more than 15 cycles [43, 44], but XENON100 shows a negative result. Further experiments of the same type with DAMA are under construction or in the data taking process. The CoGeNT experiment has claimed an annual modulation which is compatible with a light dark matter particle in the mass range of $(7-11)$ GeV/c^2 [45, 46]. The CDMS-II collaboration reported the observation of 3 events of their silicon detectors [47].

Direct dark matter detection by observing the elastic scattering applies mostly for WIMPs. In the case of WISPs, due to their very light mass, the recoil energy is much lower below the energy threshold of detection. Different to WIMP searches, WISP searches are based on very diverse methods, including radio, optical, X-ray detection technique. E.g., ADMX [48] searches for the radio signal from the conversion of axions to photons, CAST and SHIPS [49–52] search for the WISPs from the Sun.

1.3.2 Indirect Dark Matter Searches

Indirect dark matter detection is a technique that utilizes astrophysical observations of SM particles to detect the products of the annihilation or decay of dark matter particles from galactic to cosmological scale. This method is different from the observation of large-scale structure and CMB mentioned in section 1.1 which proves the existence of dark matter, and relies on general relativity. The signature in indirect search are the SM products of dark matter annihilation and decay. Most of the final states result in the unstable SM particles which quickly decay and hadronize into stable states. There are channels where dark matter particles could decay into stable SM particles like photons, neutrinos, protons and antiprotons, electron and positions. These stable final states set apart the three main messenger particles for indirect search: signal from gamma-ray photons, neutrinos, and cosmic rays.

- Gamma-rays are an excellent messenger for indirect searches for WIMPs. Gamma-ray searches allow to reveal the origin of the signals, and high dynamic ranged instruments allow to resolve spatially the dark matter source in the case of detection. Main challenge of this method is the astrophysical background emission. Experiments being used are *Fermi* LAT [53, 54], H.E.S.S [55], MAGIC [56], VERITAS [57].

- Neutrinos preserve directional information and point back to the source, making them a useful particle for indirect searches. Experiments being used are IceCube, DeepCore [58, 59], ANTARES [60].

- Cosmic-ray hadronic particles could be created by the annihilation and decay of dark matter. The local charged cosmic-ray fluxes can be highly sensitive thanks to the low backgrounds for anti-matter produced by ordinary astrophysical processes. Due to the diffusion processes in the Galaxy, tracking of the source is a challenge. Experiments being used are PAMELA [61], AMS-02 [62, 63].

The astrophysical searches could be apply for WISPs dark matter candidates. ALPs can mix with photons and consequently be searched for in astrophysical observations, where the energy-depenedent modulations of gamma-ray spectrum is the signature of ALPs-photon mixing [54].

1.3.3 Accelerator Searches

Dark matter particles can be created in colliders. The Large Hadron Collider (LHC) accelerates two proton beams for collision with a center-of-mass energy of 14 TeV. Collided protons can produce dark matter particle with the mass ranges from GeV to several TeV. This assumption depends strongly on the hypothesis that dark matter couples to SM at the very high energy. The production could occur at the moment of collision or in the reaction chain. After the discovery of the Higgs particle in 2012, ATLAS and CMS detector collaboration, together with LHCb and ALICE, have been searching for extradimensional and BSM signals. Dark matter could be searched via missing energy due to the weakly interaction of dark matter and the baryonic detector material. An example of a candidate event that could be picked for analysis is a single jet or for signatures with missing

transverse momentum (energy) photon, or hadronic jet or leptonically decaying W to Z boson.

1.3.4 Dark Matter Distribution in the Galaxy

Direct dark matter search, which is described in the section 1.3.1, requires an understanding of the distribution and density of the dark matter at the Earth's position in the Galaxy. The understanding of the halo composition could determine the velocity of the dark matter particle in the rest frame of the laboratory. Thus determine the signal shape that could be observed in the spectrum. A general result could be applied for both WIMPs and WISPs searches but vary significantly for different experiment type. The velocity relative to the local rest frame distribution of dark matter is widely described by Maxwell-Boltzmann distribution:

$$f(\mathbf{v})d\mathbf{v} = \frac{d\mathbf{v}}{(2\pi)^{3/2}\sigma^3} \exp\left(-\frac{|\mathbf{v}|^2}{2\sigma^2}\right). \tag{1.3}$$

The dispersion velocity $\sigma = \sqrt{3/2}v_c$ with v_c the local circular speed which recent studies show values ranging from (200 ± 20) kms^{-1} to (279 ± 33) kms^{-1} [64]. The commonly used value is 270km/s as an average result from different analyses [65]. The velocity profile (1.3) is truncated at the velocities exceeding the escape velocity of the Galaxy [36] which defines a cut-off in the description of the halo velocity profile. The value of the escape velocity in the 90% confidence interval ranges from 498 kms^{-1} to 608 kms^{-1} [66]. One can choose the model for the dark matter density profile, which leaves the density in the range of $(0.2 - 0.6)$ GeVcm^{-3}. The value widely used is 0.3 GeVcm^{-3} derived from the mass modelling of the Milky Way and observational results [64, 67, 68]. The underlying assumption (dark matter distribution to be Maxwellian, its truncation, and related parameters) are not necessarily true for all considered types of dark matter particles. The local inhomogeneities of the dark matter distribution can be mapped with a large scale observation (GAIA satellite).

The mapping of star movement, e.g., rotation velocity is the indirect observation for the dark matter density. N-body numerical simulations have been performed to understand the halo formation and structure. The simulation usually contains only dark matter and shows the triaxial velocity distribution [69–72]. The predicted halo structure presents cusped profiles with steep variations towards the center of the halo, while the observations show generally a flat-core profile. Moreover

the prediction of sub-haloes is not consistent with observations. The emptiness of baryonic matter can play an important role in the result of the simulation. The large scale structure simulation with the presence of baryonic particles give a better match result with the observation, and gas outflows change the distribution of gas and star [73]. Simulation with the presence of Super Massive Black Hole gives a good constraint on the halo density and information of sub-halo structure. ROMULUS [74] is a state-of-the-art cosmological N-body+Smoothed-Particle Hydrodynamics simulation to develop an improved signal model for direct dark matter searches.

One should notice the freedom of picking the value of the parameters (circular velocity, escape velocity, and dark matter density) which are relevant to the interpretation of the experimental results. Above all, the adoption of the Maxwell-Boltzmann profile (1.3) is widely used to the early stage of signal shape spectrum prediction.

1.4 Hidden Photon

The most straightforward and prominent model of hidden sectors theory is the introduction of a hidden photon as an additional gauge field $U(1)$ which kinetically mixes with the eminent electromagnetic gauge field $U(1)$ of the SM. The hidden photon γ' at sufficiently low mass could be so-far undetected, it would be long-lived and as a DM candidate [75]. In contrary, the hidden photon couples weakly with the SM particles renders themselves very light or even massless. The very low energy approach such as an extremely sensitive detector or low noise cryogenic experiment would be practical.

1.4.1 Lagrangian and Kinetic Mixing

The extent SM Lagrangian with the hidden $U(1)$ is given by:

$$\begin{aligned}\mathcal{L} = \quad & -\frac{1}{4}W^a_{\mu\nu}W^{a,\mu\nu} - \frac{1}{4}B_{\mu\nu}B^{\mu\nu} - \boxed{\frac{1}{4}X_{\mu\nu}X^{\mu\nu}}^{1} + \boxed{\frac{m_\chi^2}{2}X_\mu X^\mu}^{2} \\ & - \boxed{\frac{\chi_Y}{2}B_{\mu\nu}X^{\mu\nu}}^{3} + \frac{1}{2}\frac{m_W^2}{g^2} + \frac{1}{2}m_W^2(W^1_\mu W^{1,\mu} + W^1_\mu W^{1,\mu}). \\ & + \text{mass terms.}\end{aligned} \tag{1.4}$$

In the Lagrangian (1.4), the X_μ and g stands for the hidden photon field $U(1)$ and gauge coupling respectively, the $W_{\mu\nu}$ and $B_{\mu\nu}$ are the familiar electroweak terms from the SM. The term (1),(2), and (3) from Lagrangian (1.4) are the self-interacting term, the mass term of the hidden photon, and the interacting term between the hidden field and the electroweak field via the kinetic mixing. Meanwhile the mass of the hidden photon could arise from either Higgs or Stückelberg mechanism.

From a field theory perspective, the kinetic mixing can be generated from loops of heavy charged particles [76, 77]. Integrating out these particles, the size of the kinetic mixing χ_Y can be estimated as a loop factor, for two heavy fermions (charged particles) with mass m_i and charges $Q_{i,v}, Q_{i,h}$ with $i = 1, 2$ for each particle. The kinetic mixing can be infered from the gauge coupling g_h in the hidden sector by [77]:

$$\chi_Y = -\frac{4}{3}\frac{g_Y g_h}{\pi^2} Q_v Q_h \ln\frac{m_1}{m_2}. \tag{1.5}$$

At a lower mass of the hidden photon and lower energy regime, with the condition $m_{\gamma'} \ll m_W$, Lagrangian (1.4) reduced to a simpler form with the self-interaction of the hidden field (and its mass term), the electromagnetic field, and the interaction between them:

$$\mathcal{L} = -\frac{1}{4}F_{\mu\nu}F^{\mu\nu} - \frac{1}{4}X_{\mu\nu}X^{\mu\nu} - \frac{\chi}{2}F_{\mu\nu}X^{\mu\nu} + \frac{m_X^2}{2}X_\mu X^\mu + ej_\mu A^\mu. \tag{1.6}$$

The mixing with photon at lower energy is given by $\chi = \chi_Y cos(\theta_W)$ in which θ_W is Weinberg angle, $F_{\mu\nu} = \partial_\mu A_\nu - \partial_\nu A_\mu$ is the field strength of the regular electromagnetic field, correspondingly the $X_{\mu\nu} = \partial_\mu X_\nu - \partial_\nu X_\mu$ for the field strength tensor of the hidden field. The physical corollary of the kinetic mixing term could be shown by displaying the Lagrangian in the diagonal eigenbasis, since the hidden $U(1)$ is assumed to be spontaneously broken (by two mechanism mentioned above), the hidden photon field has a mass [75]. In order to simplify the Lagrangian (1.6) to get rid of the kinetic mixing term by introducing two ways of re-defintion either the ordinary photon field or the hidden photon field.

1.4.2 Shifting the A_μ

Inserting the shift

$$A^\mu \to A^\mu - \chi X^\mu \tag{1.7}$$

into (1.6), the mixing term could be cancelled but the *new* electromagnetic currents followed by the kinetic mixing parameter.

$$\mathcal{L} = -\frac{1}{4}F_{\mu\nu}F^{\mu\nu} - \frac{1}{4}X_{\mu\nu}X^{\mu\nu} + \frac{m_X^2}{2}X_\mu X^\mu + ej_\mu(A^\mu - \chi X^\mu). \tag{1.8}$$

Undoubtedly, the Lagrangian above provides a massless boson A which couples to electromagnetic current ej_μ, and an uncharged vector boson X with mass m_X coupled to the SM current via $-e\chi j_\mu$. The extended Coulomb interaction is given by [75, 78]:

$$V(r) = q_1 q_2 \frac{\alpha}{r}\left(1 + \chi^2 e^{-m_X r}\right). \tag{1.9}$$

With q_1, q_2, r, α, respectively, are the charge of particle 1 and particle 2, the distance between them, and the fine-structure constant. The first term of the potential (1.9) is the Coulomb interaction, the second term stands for a new force, as mentioned "fifth force" or "dark force" mediated by the massive boson X. In this scenario, the new force at a short distance could not be distinguished because $m_X \gg 1/r$, these conditions shorten the interacting distance of force and couldn't be observed. On the other hand, if the χ is small, the force becomes frail and unable to observe.

1.4.3 Shifting the X_μ

There is an additional method to remove the kinetic mixing term by the shifting

$$X^\mu \to X^\mu - \chi A^\mu. \tag{1.10}$$

The shift leaves our Lagrangian (1.6):

$$\mathcal{L} = -\frac{1}{4}F_{\mu\nu}F^{\mu\nu} - \frac{1}{4}X_{\mu\nu}X^{\mu\nu} + \frac{m_X^2}{2}(X_\mu X^\mu - 2\chi X_\mu A^\mu + \chi^2 A_\mu A^\mu) + ej_\mu A^\mu. \tag{1.11}$$

The physical phenomena inferred from this Lagrangian is different and independent from the previous approach. Again, the kinetic mixing term is removed but the charged particles are charged under the regular electromagnetic field from the previous section, and there is no substitute component that modified the charge. Thus the approach of the prior section is inapplicable. Nevertheless, by rewriting the mass term of the Lagrangian (1.11)

$$-\frac{m^2}{2}\begin{bmatrix} X_\mu & A_\mu \end{bmatrix}\begin{bmatrix} 1 & \chi \\ \chi & \chi^2 \end{bmatrix} = \begin{bmatrix} X^\mu \\ A^\mu \end{bmatrix}. \tag{1.12}$$

One can show there is a mixing or an oscillation between the hidden photon and the hidden field with the ordinary photon $A \leftrightarrow X$. This mixing is analogous to the non-diagonal mass term of the neutrino oscillation, e.g. the oscillation matrix for Dirac neutrinos (ν_1, ν_2):

$$\begin{bmatrix} \nu_1 \\ \nu_2 \end{bmatrix} = \begin{bmatrix} \cos\theta & \sin\theta \\ -\sin\theta & \cos\theta \end{bmatrix}\begin{bmatrix} \nu_1 \\ \nu_2 \end{bmatrix}. \tag{1.13}$$

Taking the same similarity from neutrino experiments, to observe the oscillation, one requires an intense photon field as the source of the photon field, a distance preserved for the oscillation could take place and a sensitive detector. On the Earth laboratory, a source of the high-intensity laser could be created and ranging in a broad wavelength which could cover a wide mass range of hidden photon.

1.5 Search for Hidden Photon

In the previous section, one has seen the brief theoretical foundation of the hidden photon as the mediator or messenger particle between the hidden sector and visible sector. From the same Lagrangian, but following different approaches, one can infer different physical interpretation and related phenomena. The following subsections explain the hidden photon search techniques and related experiments, together with their results presented in Fig. 1.3 as exclusion limits for the kinetic mixing constant χ and mass of the hidden photon.

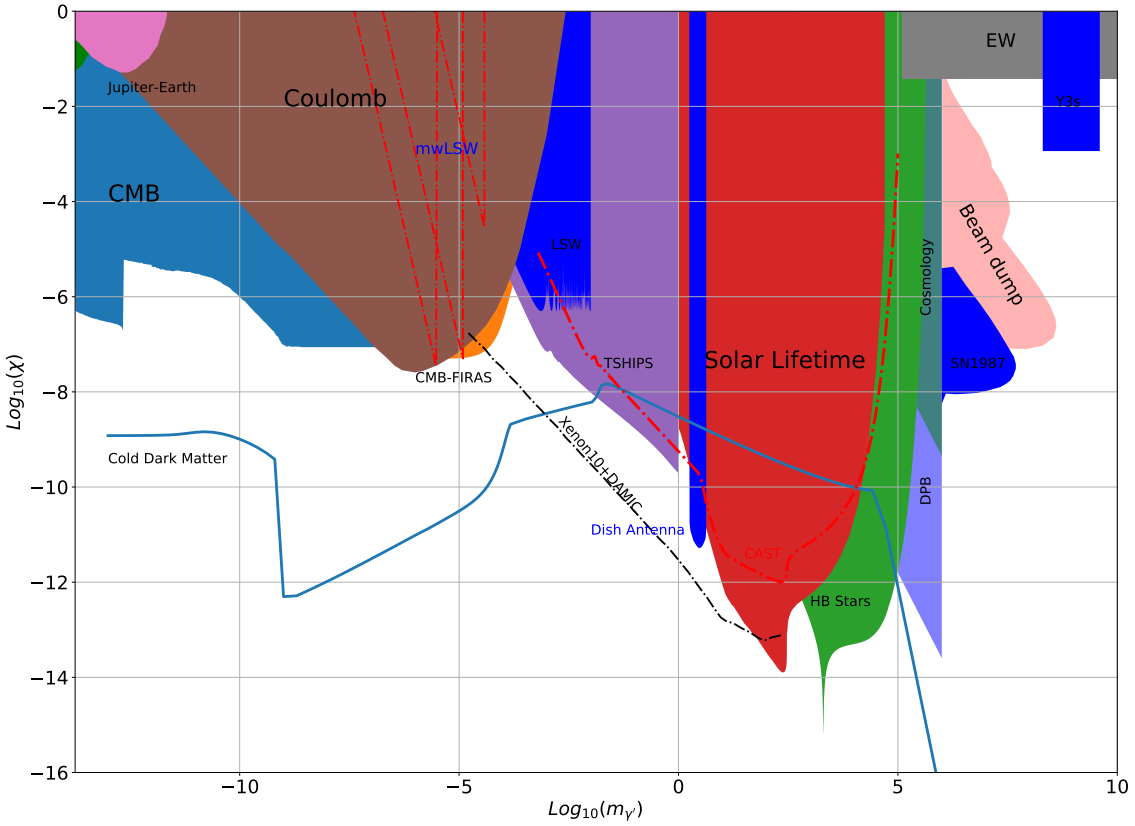

FIGURE 1.3: The exclusion limit of the kinetic mixing constant χ to the mass of hidden photon $m_{\gamma'}$ from the combination of direct and indirect searches.

The oscillation/conversion from hidden photon to photon (and vice versa) is one of the main mechanism which is widely adopted in many direct and indirect searches.

1.5.1 Indirect Search for the Hidden Photon

- Following the approach from section 1.4.2 in observing the extended Coulomb interaction or the "fifth force". High precision measurements of the Coulomb law has been done to search for a "fifth force". The Cavendish type experiments have been done since a half-century ago with an accuracy of about one part in 10^{16} [78–80]. Spectroscopy can provide a sensitive tool to test Coulomb's law on atomic at much shorter scales by observing the atomic transitions [81, 82]. On the larger length scale, one can also look at magnetic fields of Earth and Jupiter which have been mapped with great precision. These experiments result in the top left corner and the labelled "Coulomb" part of Fig. 1.3.

- Several stellar objects (Sun, Horizontal Branch stars) show a mild difference to the standard theoretical model for stellar cooling. Observations have shown deviations from the expected behavior, indicating in all cases more rapid cooling. The hidden photon, likewise WISPs, could explain this non-standard cooling mechanism: hidden photons produced in the high luminosity core would leave the star interior without interaction with the medium due to weak interaction with baryonic matter. The hidden photon carries away the energy can not be detected directly but could explain the over-efficient cooling [83]. In Fig. 1.3, the regions "Solar Lifetime" and "HB Stars" are the exclusion limits from the observations of the cooling abnormality.

- Observations of CMB anisotropy also constrain the hidden photon parameter [84, 17]. By taking into account the refractive properties of the primordial plasma showing that the medium effects are significant when a resonant hidden photons and photons conversion is possible. This is similar to the Mikheev-Smirnov-Wolfenstein effect (MSW) in neutrino physics which leaves the imprint of neutrinos on the CMB [85]. The observationals result from CMB [86] set a large exclusion range in Fig. 1.3.

- The observation of SN1987A constrain the hidden photon which kinetically mixes with the photon. The constraints are realized because the excessive Bremsstrahlung radiation of the hidden photons can lead to a rapid cooling of the SN1987A progenitor core, in contradiction to the observed neutrinos from that event [87].

1.5.2 Direct Search for Hidden Photon

- Instead of looking for the extended force, one could directly search for the new exchange particle. From the previous section, the charge particle Q (concerning normal $U(1)$) carries a hidden charge $Q_X = -\chi Q$ coupled to the hidden photon. This charged particle can be produced in scattering experiments where the hidden photon at GeV mass range can hide, e.g., with fixed target experiments [88, 89], beam dumb experiment [90, 91]. Hidden photons are produced in a process similar to ordinary Bremsstrahlung off an electron beam incident on a target. They are emitted at a small angle in forward direction and carry most of the beam energy. Because of their feeble

interaction with SM particles, they can traverse the beam dump and can be observed in a detector behind the beam dump by their decay into fermions.

- Scattering experiment built for WIMPs mentioned in section 1.3.1 could also be utilized to search for hidden photon. Similar to the ordinary photons, hidden photons can be absorbed by electrons in the bulk of a silicon device and lead to an ionization signal.

- **Helioscope Experiment** The Sun is a well-known laboratory with an extremely high number of photons which is produced at its centre. The photons could oscillate to hidden photons and escape to the outer stellar surface of the Sun. In this environment the oscillation is enhanced by the plasma resonances (similar to MSW effect). The oscillation could lead to a more efficient cooling. Helioscope uses a similar setup as the LSW type experiments but replace the laser source with the Sun [92–94, 49]. CAST in CERN [50] and SHIPS experiment in Hamburg Sternwarte [52] are the two helioscope experiment that have set constraints on the hidden photon.

- **Light-shinning-through-wall** The light-shining-through-wall (LSW) is a type of experiment could be used to detect either hidden photons, axions or ALPs. In the LSW experiment, an intense laser beam is shot into an optically thick wall with the photon detection type system located on the other side of the wall. The oscillation happens firstly during the path from the laser source to the wall ($A \rightsquigarrow X$), the hidden photon would pass through the wall and subsequently, restore into detectable photon by the second oscillation ($X \rightsquigarrow A$). In the case of LSW, there are two oscillations taking place in one to produce a "shining" photon, thus the probability for the two conversions would be smaller than a single oscillation detection [95–97]. This simple concept is improved with two resonator cavities, one plays a role of converting the photon to hidden photon. This hidden photon travels "through the wall" to the other cavity and has the resonant conversion to an observable photon [48, 98].

- **Dish Antenna** A newly developed concept uses a dish antenna to detect the photon from the converted hidden photon [99]. The faint electromagnetic waves which are emitted perpendicularly to the conducting surfaces are focused using a spherically shaped mirror. The hidden photon-induced light emerging from any part of the mirror is gathered at the center of the sphere

where various detectors (e.g., PMT) can be suitably placed. Representation for this type of experiment is the Dish Antenna experiment in Tokyo [100] and FUNK at KIT [101].

1.5.3 Hidden Photon as Cold Dark Matter

One can consider the hidden photon as a candidate for the cold dark matter particle [102]. The parameter space of hidden photon as a CDM particle is limited to the region below the CDM line in Fig. 1.3. There are very few experiments and observations could contrain the hidden photon below the CDM line. Especially from the mass range of $10^{-16} - 10^{-4}$ eV there is no measurement which can cover this parameter range. WISPDMX is the only experiment which could cover a large fraction of this mass range. In the next chapter, the underlying foundation of WISPDMX is presented.

Chapter 2

Haloscope Experiment for Hidden Photon Search

Abstract

The haloscope type experiment described in the following is a direct search method for hidden photons, and it was inspired by the axion haloscope. This chapter will present the principles of the hidden photon haloscope experiment. The first section will describe briefly the motivation of the hidden photon haloscope experiment and the second section will present the expected power developed inside the cavity from the conversion of hidden photons to SM photons. Section 2.3 will present the broadband sensitivity to hidden photon which includes the off-resonance regions. In section 2.4, the relation between the hidden photon signal profile and the spectral resolution of the WISPDMX is considered. Finally, section 2.5 will discuss the sensitivity of the haloscope experiment, and, in particular, WISPDMX with its broadband sensitivity.

2.1 Introduction

The search of axion dark matter has been carried out for more than three decades, from direct to indirect search, with numerous detection techniques were used and new ones are being developed. The experiments exploit the coupling of axion to photon by observing the conversion of the axions into photons which can be detected. One type of experiment that has been widely used in searches for axions

and axion-like-particles (ALPs) dark matter are so-called axion haloscope [103]. The conversion between axions and photons in the presence of a strong magnetic field can be made more efficient by employing a resonator with the resonance at the frequency corresponding to the energy of the produced photons. The energy of the converted photons equals the total energy of the axion. The expected axion signal is located at the frequency equivalent with the rest mass energy while the signal profile spreads accordingly to its kinetic feature. A similar analogy is applied to hidden photon but with a small modification of the form factor $\mathcal{G}$ and the fact that the hidden photon does not require the magnetic field for the conversion. The oscillation between the hidden photon and photon is amplified by the electrical field structure of the resonator without the ambient magnetic field unlike the case of the axion. The following sections will present the theoretical basis of the haloscope type experiment such as the power developed in the resonant powered by the hidden photon conversion.

2.2 Search of Hidden Photon in the Resonant Cavity

Section 1.4.3 has shown that the oscillation between the hidden photon to the SM photon which is similar to the neutrino oscillation. In the resonator, the conversion between the hidden photon to photon is similar to the case of axion conversion [102]. From the Lagrangian 1.11, the equation of motion for the photon field A in the first order of the kinetic mixing term is given by:

$$\partial_\mu \partial^\mu A^\nu = \chi m_{\gamma'}^2 X^\nu, \tag{2.1}$$

with χ the kinetic mixing constant between hidden photon and photon, and $m_{\gamma'}$ the mass of the hidden photon. It is trivial to see that the hidden photon acts as a source for the SM photon. Under the assumption that the hidden photon is cold dark matter, the energy density of the hidden photon is equal to cold dark matter density ρ_{CDM}

$$\rho_{CDM} = \frac{m_{\gamma'}^2}{2} |\mathbf{X}|^2, \tag{2.2}$$

with $|\mathbf{X}|$ the spatial component of hidden photon field X^μ. Because the structure of dark matter in the galatic scale is clumped, the local dark matter density on

Earth ($\frac{0.3\text{GeV}}{\text{cm}^3}$) is higher than the average density in the Universe ($\sim \frac{\text{keV}}{\text{cm}^3}$). In general, the structure formation has a significant influence on the local hidden photon condensate. However, in this context, two possible scenarios can describe the behavior of the hidden photon field which is limited in the region where the laboratory is located [102].

1. The hidden photon field has the same direction (at least in the local region of the laboratory). The direction of the field is presented by the vector $\hat{\mathbf{n}}$ given by:
$$\mathbf{X} = \hat{\mathbf{n}}\frac{\sqrt{2\rho_{CDM}}}{m_{\gamma'}}. \tag{2.3}$$
2. The hidden photon field behaves like gas, homogeneous and isotropic. The argument in equation 2.3 is still valid, however, the final result must be averaged in all the direction.

The search for hidden photons in scenario (1) requires the knowledge on the relative orientation of the cavity to the unknown direction of the field. Inside the resonator, the electromagnetic field could be written in terms of the resonant electric field:

$$\mathbf{A}(\mathbf{x}) = \sum_i \alpha_i \mathbf{A}_i(\mathbf{x}), \tag{2.4}$$
$$C_i = \int d^3\mathbf{x}|\mathbf{A}_i(\mathbf{x})|^2, \tag{2.5}$$

with C_i is the normalization coefficients, α_i is the expansion coefficient which could be retrieved by solving the resonant cavity equation with the source and loss by the absorption of cavity walls:

$$\left(\frac{d^2}{dt^2} + \frac{\omega_0}{Q}\frac{d}{dt} + \omega_0^2\right)\alpha_i(t) = b_i \exp(-i\omega t), \tag{2.6}$$

ω_0 and Q are the resonant frequency and quality factor of the resonance i. The hidden photon which oscillates to the electromagnetic field take the role of the source b_i:

$$b_i = \frac{\chi m_{\gamma'}^2}{C_i}\int dV\, \mathbf{A}_i \cdot \mathbf{X} \tag{2.7}$$

Hence the expansion α_i coefficient could be retrieved by solving the equation 2.6:

$$\alpha_i = \frac{b_i}{\omega_0^2 - \omega^2 - i\frac{\omega\omega_0}{Q}} \exp(-i\omega t), \tag{2.8}$$

with ω is the frequency given by the energy of the hidden photon: $\omega = E_{\gamma'}$. The power developed at the resonance of the cavity is:

$$P = \frac{U}{Q}\omega_0 \tag{2.9}$$

While U is the total energy stored in the cavity and given by

$$U = \frac{|\alpha_i|^2\omega^2}{2} \int d^3\mathbf{x}|\mathbf{A}_i|^2. \tag{2.10}$$

By replacing the $\omega_0 = m_{\gamma'}$ as the conversion of hidden photon with the mass equal to the resonant frequency, one can obtain the power measurablemeasurable with an antenna in a resonant cavity powered by the conversion of hidden photon to photon:

$$P_{\text{out}} = \kappa\chi^2 m_{\gamma'}\rho_{\text{CDM}}QV\mathcal{G}. \tag{2.11}$$

with V the volume of the cavity, κ is the coupling factor between the probe and the antenna. The maximum value of κ is 0.5 at the critical coupling state between the antenna and the cavity where the antenna absorbs half of the energy at the resonance while the other half of the power dissipates inside the cavity's resistive walls. The $\mathcal{G}$ is the form factor of resonance which characterizes the sensitivity of a resonant mode to the hidden photon field, given by

$$\mathcal{G} = \frac{|\int dV\mathbf{A}(\mathbf{x})\cdot\hat{\mathbf{n}}|^2}{V\int d^3\mathbf{x}|\mathbf{A}(\mathbf{x})|^2}. \tag{2.12}$$

For the scenario (1), the angle θ between the $\mathbf{A}(\mathbf{x})$ and $\hat{\mathbf{n}}$ must be known or assumed to vary over time. On the scenario (2), the angle is averaged and the form factor $\mathcal{G}$ can be calculated intuitively from the electric field of the resonance given by

$$\mathcal{G} = \frac{1}{3}\frac{|\int dV A(\mathbf{x})|^2}{V\int d^3\mathbf{x}|\mathbf{A}(\mathbf{x})|^2} \tag{2.13}$$

given $\langle\cos^2(\theta)\rangle = 1/3$.

2.3 Broadband Gain

In most of the axion haloscope experiments, the frequency region surrounding the resonance is considered. The experimental setup is built to benefit for the resonant amplification of this particular region. However, in the hidden photon haloscope experiment, it is possible to search for the hidden signal at the frequency off-resonance by having the broadband scan cover a wide range of frequency. The experiment which performs the broadband search, e.g., WISPDMX, could have the off-resonance spectrum to characterize the coupling of hidden photon and photon. The equation 2.11 shows the power output of the cavity with the hidden photon mass at the resonant frequency, the term $Q\mathcal{G}$ denotes the gain of the hidden photon signal at the resonance frequency[1]. The $Q(\omega)$ factor follows the Lorentzian profile with the peak at the value of $Q(\omega_0)$. One can conservatively imply the form factor $\mathcal{G}$ under the amplification of the resonance is constant as the off-resonance field structure follows equation 2.13. The gain at the frequency ω under the influence of resonant modes i is given by $Q_i(\omega)G_i$, and with the existence of multiple resonances, the total gain at the frequency is given by:

$$\mathcal{G}(\omega) = \sum_i Q_i(\omega)G_i. \tag{2.14}$$

The broadband gain provides the possibility of hidden photon search in a wide mass range outside of the resonance. Especially for the case of the WISPDMX that the spectrum covers the broadband frequency of 0-500 MHz. Fig. 2.1 shows the broadband gain from a single resonance and the total gain contributed from the four resonant modes which have the high form factor ($\mathcal{G} > 0.1$).

[1] it is important to keep in mind that in this section "the resonance" is sensitive to the hidden photon, with $\mathcal{G} > 0.01$

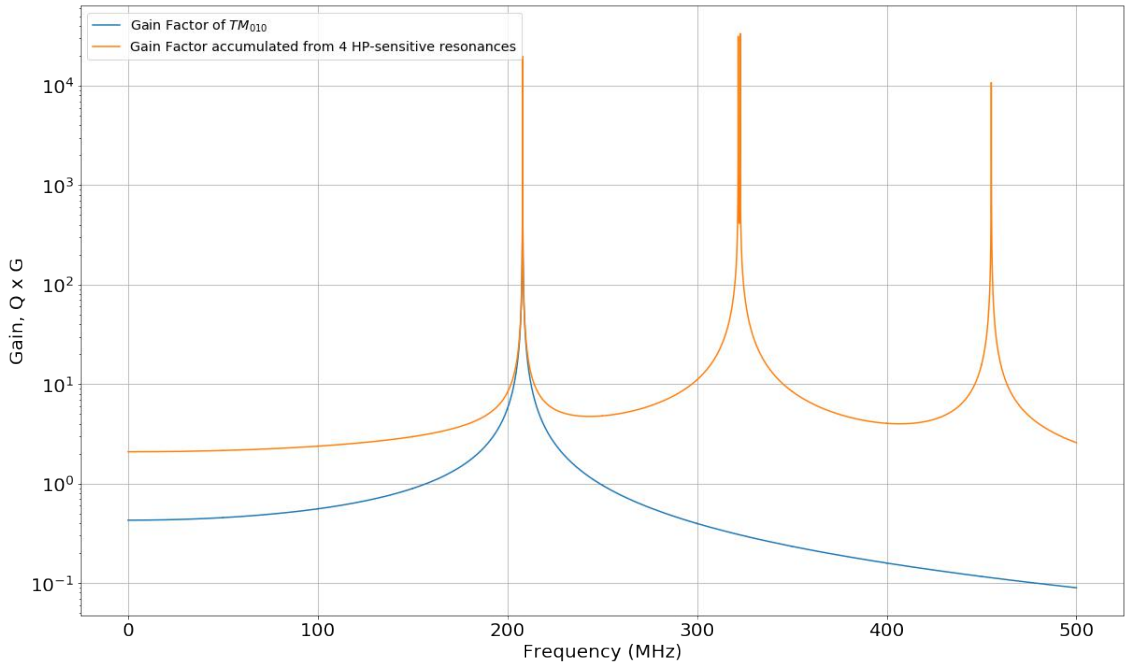

FIGURE 2.1: The broadband gain in the coverage of the WISPDMX. The blue line is the gain of the ground mode TM_{010} and the orange line is the total gain of all four hidden photon sensitive resonances. The gain at the off-resonant frequency is developed by accumulating the gain from the other modes.

2.4 Hidden Photon Signal Profile

In section 1.3.4, the distribution of dark matter in the Galaxy have been discussed. The requirements of dark matter particles discussed in 1.3.4 are equally applied to the hidden photon dark matter particles. In the haloscope experiment searches for hidden photon, one assumption is considered is that the Solar system travels in the region with the CDM density of $\rho_{CDM}0.39\text{GeVcm}^{-3}$. In the scenario (2), where the hidden photon CDM behaves like a gas, the mean kinetic energy of the particles to the local frame of the CDM halo is given by $\frac{1}{2}m_{\gamma'}\bar{v}^2$; where $\bar{v}$ is the velocity dispersion of the hidden photons in the halo. The total energy of non-relativistic hidden photons is the total rest mass energy and kinetic energy of the particle:

$$E = m_{\gamma'}c^2 + \frac{1}{2}m_{\gamma'}\bar{v}^2. \tag{2.15}$$

By considering the signal of the hidden photon without the kinetic energy in the spectrum, one could expect a peak in a single channel at the frequency of the

particle mass. However, the kinetic energy of the hidden photon determines the signal line shape on the spectrum as the hidden photons follow a Maxwellian velocity profile centered at the frequency of the particle's mass. In the Galaxy's halo frame, the laboratory's motion is the combination of the Earth's motions (orbital-$\mathbf{v_o}$ and rotational motion-$\mathbf{v_R}$) to the Solar System and the Solar system's motion to the halo ($\mathbf{v_S}$):

$$\mathbf{v}_{\rm lab} = \mathbf{v_S} + \mathbf{v_o} + \mathbf{v_R}. \tag{2.16}$$

The Maxwellian profile would modulate between the maximum and minimum values of $\mathbf{v}_{\rm lab}$ due to the Earth having its yearly revolution and daily rotation. The Maxwellian energy distribution $f(E)$ and the parameterized energy distribution $f(u)$ of hidden photons are [104, 105]:

$$f(E)dE = \sqrt{\frac{3}{2\pi}}\frac{dE}{r}\frac{1}{\frac{1}{2}m\bar{v}^2}\exp\left[-1.5(r^2+\frac{E}{\frac{1}{2}m\bar{v}^2})\right]\sinh\left(3r\sqrt{\frac{E}{\frac{1}{2}m\bar{v}^2}}\right), \tag{2.17}$$

or

$$f(u)du = \sqrt{\frac{3}{2\pi}}\frac{du}{r}\exp\left[-3(r^2+u)/2\right]\sinh(3r\sqrt{u}), \tag{2.18}$$

$r = v_{\rm lab}/\bar{v}$ is the ratio between the laboratory velocity and the halo's rms velocity (270 km/s). The unit $u = \frac{E}{\frac{1}{2}m\bar{v}^2}$ reflects the relation between the DM particle mass and the physical width of the distribution as following:

$$u = \frac{m_{\gamma'}v_{\gamma'}^2/2c^2}{98{\rm Hz}(m_{\gamma'}c^2/\mu{\rm eV})} = \frac{\Delta f}{98{\rm Hz}(m_{\gamma'}c^2/\mu{\rm eV})}. \tag{2.19}$$

The distribution and the width of the hidden photon line depend on the ratio r or $\mathbf{v}_{\rm lab}$ given by equation 2.16. One can safely neglect the contribution of the rotational velocity of the Earth but maintain the term on the orbital motion of the Earth around the Sun ($\mathbf{v}_{\rm lab} = \mathbf{v}_{\rm E}$). The signal profile modulates between the lineshapes of the highest $\mathbf{v_E}$ and lowest $\mathbf{v_E}$ in absolute value.

$$\mathbf{v_E} = \mathbf{v_S} + \mathbf{v_0}, \tag{2.20}$$

$$v_E^2 = v_S^2 + v_o^2 + 2v_S v_o \hat{v}_S \cdot \hat{v}_o. \tag{2.21}$$

The magnitude of the Sun velocity is 230 km/s with respect to the Galaxy center, and in the direction of 60° above the ecliptic plane of the Earth's orbit, given the $\hat{v}_S \cdot \hat{v}_o = \cos(60°)$. Hence the ratio r modulates between two equivalent values of

two maximum and minimum v_E :

$$v_E = \begin{cases} 246.256 \text{ km/s - max velocity} \\ 216.642 \text{ km/s - min velocity} \end{cases} \tag{2.22}$$

$$r = \begin{cases} 0.912 \text{ - max r} \\ 0.802 \text{ - min r} \end{cases} . \tag{2.23}$$

However, the variation in relative velocity of the lab to the halo does not show any significant afteration in the derived results. From this point, the value of r is assumed to be 0.85 as the contribution from the orbital velocity is negligible ($\mathbf{v}_{\text{lab}} = \mathbf{v_S}$). Fig. 2.2 shows the ideal profile of the hidden photon signal to the maximum and minimum of the Earth velocity in the Halo rest frame. However, the exact lineshape must describe hidden photon CDM particle limited to the escape velocity of the Sun and higher than the escape velocity of the Galaxy. The first case defines the lower end of the line shape, where the Sun captures the particle with $v_{\gamma'} < v_{\text{Escape Sun}}$ [106]. Any hidden photon dark matter particles are fallen into the Sun and could not travel to the Earth. Nevertheless, the $v_{\text{Escape Sun}}$ is equivalent with $u = 0.16$ and it is negligible, one could adopt $u = 0$ as the lower limit. In the second case, the hidden photon particle can escape the gravitation potential of the galaxy $v_{\gamma'} > v_{\text{Escape Galaxy}}$, and does not contribute to the tail of the Maxwellian lineshape. Numerical simulations indicate that the upper-end truncation occurs at velocities of 450–650 km/s [68, 107], which corresponds to $u = 2.78$–5.80. In the following calculations, the truncation velocity of 550 km/s ($u = 4.15$) as well as the ratio $r = 0.85$ are assumed.

The final profile must follow the Maxwellian profile and includes the truncation of the escape velocity at $u = 4.15$. One can determine the power that can be recovered in a bandwidth δu by an integration around the peak of the profile ($u = 0.76$ for a profile with $r = 0.85$). The optimal bandwidth is the one which has the largest fraction of energy which could be recovered. One can see in Fig. 2.2, the signal profile spreads on mutiple value of u, the total energy which could be recovered inside a bandwidth Δu is given by integrating around the maximum value of the profile within the range of Δu. A qualitative example can provides an insight to the bandwidth effect.

- If the bandwidth is high, e.g., $6u$, it will cover most of the signal, but the noise floor will also increase due to the size of bandwidth. The undersampling

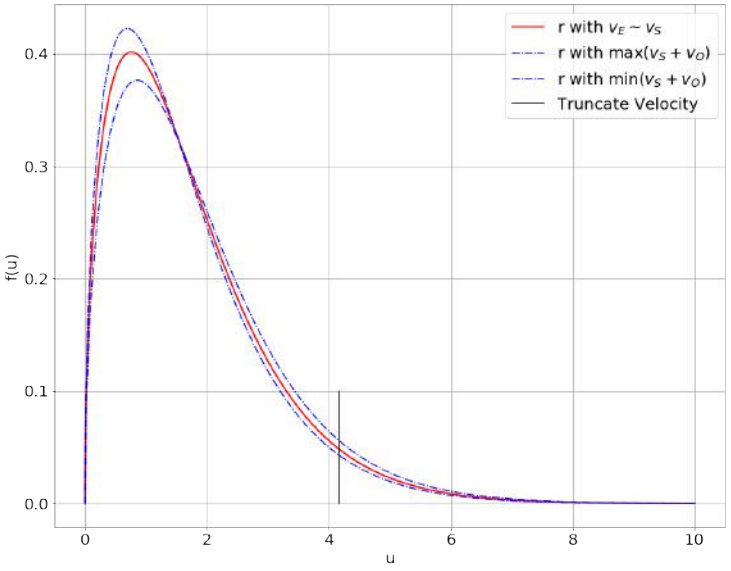

FIGURE 2.2: The profile of the hidden photon signal. The profile follows the modulation between the lineshapes of the maximum and minimum $\mathbf{v_S + v_o}$

of the signal will result in a low SNR.

- If the bandwidth is narrow, e.g., $1u$, and only a single channel is under attention. One can see that the bandwidth covers only a small fraction of the signal.

The optimal bandwidth is determined from the a function which could reflect both the fraction of signal recovered and the width of bandwidth (which is proportional to the noise).

$$\mathcal{F}(\Delta u) = \frac{\text{Energy in the bandwidth}}{\text{Total energy of the signal}} \times \frac{1}{\text{Width of bandwidth}} \tag{2.24}$$

$$= \frac{\int_{\Delta u} f(u)du}{\Delta u \int_0^\infty f(u)du} \tag{2.25}$$

with $f(u)$ is given by 2.18, the optimal bandwidth result in a highest value of $\mathcal{F}$. From the calculation, the optimal bandwidth is $\Delta u = 3.03$ as shown in Fig. 2.3.

Fig. 2.4 shows the value of u and the optimal width ($3.03u$) to the mass and equivalence frequency of the hidden photon. A hidden photon with high mass (e.g., 2μeV) needs a wider optimal bandwidth (600 Hz) while a lighter hidden photon requires a more narrow bandwidth. In WISPDMX, the width of a channel is 50 Hz, this width is optimal in resolving the signal at the frequency of 40.54

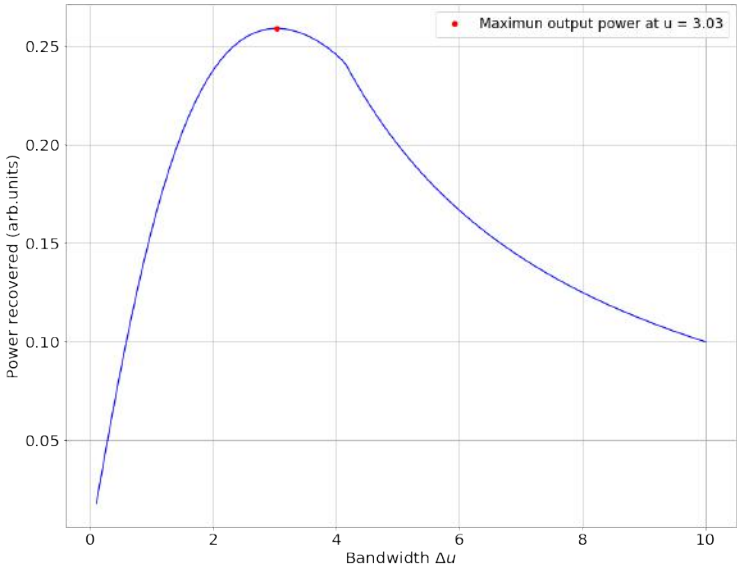

FIGURE 2.3: The fraction of signal energy recovered concerning the size of the bandwidth. The optimal width ($u = 3.03$) returns the largest fraction (the red indicator).

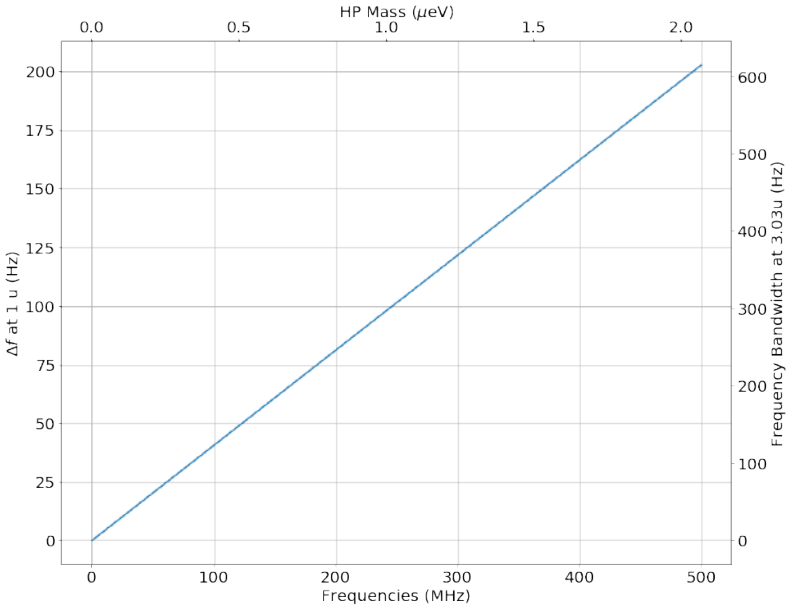

FIGURE 2.4: The value of u to the mass of hidden photon in Hz, together with the optimal bandwidth 3.03u .

MHz, oversampled at a higher frequency, but undersampling at lower frequency. At the resolution of WISPDMX and lower frequency, the recovered signal suffer from the undersampling and causes the sensitivity to decrease proportionally with the $\sqrt{f}$. The oversampling problem is resolved by scanning multiple channels with the total width equal to the optimal bandwidth, e.g., the two channels scan is more effective than the single channel scan at the frequency range of 59.059-100.6 MHz. The optimum sensitivity achieved with the multiple channel scan is shown in Fig. 2.5 which shows an effective gain factor for the hidden photon signal received in multiple channels of WISPDMX measurements. The frequency ranges for achieving the optimal sensitivity by summing over a given number of channels are given in Table 2.1. This factor can be utilized to modify the term stand for local dark matter density in equation 2.11 and determines the equivalence sensitivity of WISPDMX.

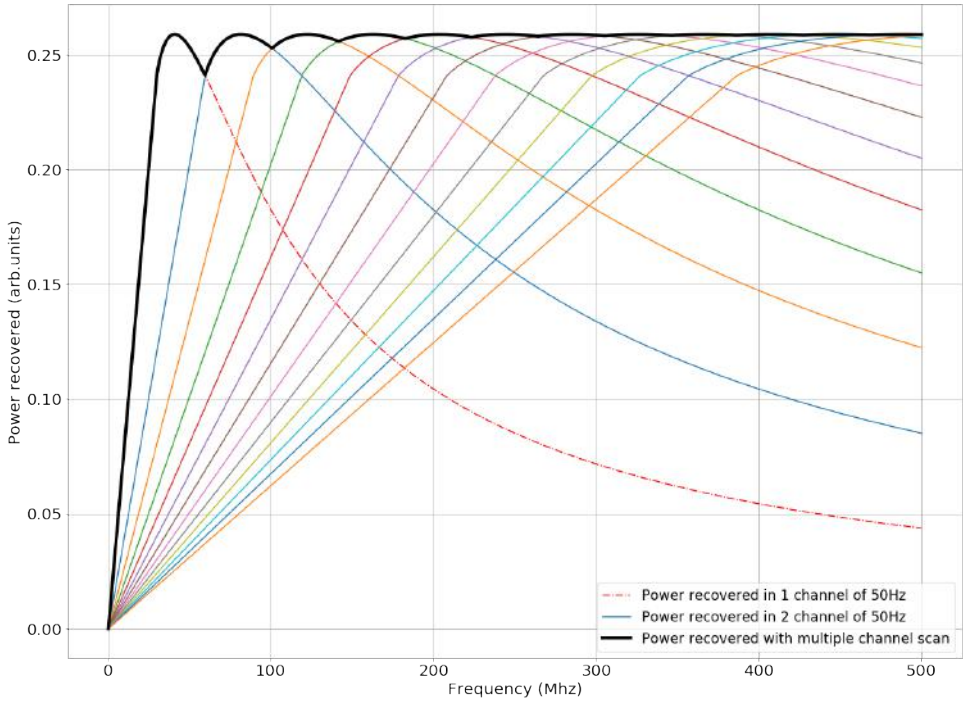

FIGURE 2.5: The power recovered from a single channel scan to multiple channel scan. The colored lines illustrate the signal's energy recovered with the scanning over a fixed number of spectral channels, from one to twelve. The upper black envelope line describes the recovered energy of the WISPDMX with the strategy of multiple channel scan.

In conclusion, one can either search for the signal in the conservative method of single channel scan under the assumption that the particle energy is concentrated

in one channel or multiple channel scan. The concept of the signal profile presented in this section provides an efficient method to optimizing the signal bandwidth.

TABLE 2.1: The number of channels required for the scan on the different range of frequency.

Nr. of Channels	**Range (MHz)**	**Number of Channels**	**Range (MHz)**
1	0.000 - 59.059	7	263.763 - 304.804
2	59.059 - 100.600	8	304.804 - 345.345
3	100.600 - 141.641	9	345.345 - 386.386
4	141.641-182.182	10	386.386 - 426.926
5	182.182 - 223.223	11	426.926 - 467.967
6	223.223 - 263.763	12	467.967 - 500.000

2.5 Sensitivity of the WISPDMX

In section 2.2, the power output from the conversion of hidden photon to SM photon in a haloscope type experiment has been presented. Under the circumstance of the experiment, it is necessary to determine the sensitivity of the hidden photon haloscope type experiment. By converting the equation 2.11 from natural units to SI units, one can obtain

$$P_{\text{output}}/\text{W} = 2.434 \times 10^{8} \chi^{2} \kappa Q \frac{V}{\text{liter}} \mathcal{G}_{\gamma'} \frac{m_{\gamma'}}{eV} \frac{\rho_0}{\text{GeV/cm}^3}. \tag{2.26}$$

The power output in a hidden photon haloscope with typical WISPDMX parameters is:

$$P_{\text{output}}/\text{W} = 1.632 \times 10^{-16} \left(\frac{\chi}{10^{-12}}\right)^{2} \frac{\kappa}{0.1} \frac{Q}{50000} \frac{V}{447\ \text{liter}} \frac{\mathcal{G}_{\gamma'}}{0.3} \frac{m_{\gamma'}}{\mu eV} \frac{\rho_0}{\text{GeV/cm}^3} \tag{2.27}$$

The values of the parameters are given in the Table 2.2. In the haloscope experiment, the primary sources of background noise are from the cavity walls and the amplifier chain. The walls of the cavity produce a spectrum of thermal blackbody photons which is comparable with the power spectrum of the white noise generated from a resistor at the same temperature while the noise from the amplifier mostly depends on the amplifier's specification. The signal-to-noise ratio (SNR)

TABLE 2.2: The values of parameters typical for WISPDMX.

Parameter	Value	Note
Antenna Coupling -κ	0.1	0.5 at Critical Coupling
Cavity Volume -V	447	
Local DM Density -ρ_0	0.4 GeV/cm^3	
Quality Factor -Q	$\sim 10^4$	$Q = 50000$ for TM_{010}
Mass of HP -$m_{\gamma'}$	up to 2.2μeV	
Form Factor - $\mathcal{G}$	$\sim 0.3 - 0.6$	

is characterized by the Dicke radiometer equation:

$$SNR = \frac{P_{\text{output}}\sqrt{t}}{k_B(T_{\text{cavity}} + T_{\text{amplifier}})}, \tag{2.28}$$

with k_B the Boltzmann constant, T_{cavity} and $T_{\text{amplifier}}$ are the effective thermal temperature of the cavity walls and the amplifier chain, and t is the integration time. On a different approach using the Dicke radiometer equation, the more extended the integration time, the noise power decreases proportionally with $\sqrt{t}$. From the equation 2.27, one could derive the sensitivity of the WISPDMX in the language of SNR:

$$\begin{aligned}\chi &= 2.9 \cdot 10^{-15}\sqrt{\text{SNR}}\left(\frac{t}{1\text{s}}\right)^{-1/4} \\ &\left(\frac{T}{100\text{K}}\right)^{1/2}\left(\frac{\kappa}{0.1}\frac{Q}{50000}\frac{V}{447\text{ liter}}\frac{\mathcal{G}_{\gamma'}}{0.3}\frac{m_{\gamma'}}{\mu eV}\frac{\rho_0}{\text{GeV/cm}^3}\right)^{-1/2}.\end{aligned} \tag{2.29}$$

The function 2.30 is the sensitivity calculated only at the resonance. The characterization of the broadband sensitivity requires the terms that can describe the broadband properties of the experiment. In section 2.4, it has been shown that the signal at lower masses (below 60 MHz) will be undersampled and lead to decrease the sensitivity. One can introduce an term which modified the sensitivity at lower mass $\epsilon(m_{\gamma'})$ in which this term can be deduced from Fig. 2.5. While in section 2.3, the total gain $Q\mathcal{G}$ has been generalize for the production of hidden photon signal in the off-resonant regions. Therefore, the gain $Q\mathcal{G}$ and $\epsilon(m_{\gamma'})$ of the bandwidth sensitivity are the function of frequency or hidden photon mass. The coupling κ can be measured using the reflection parameter of the antenna and it generally is

a function of frequency. The broadband sensitivity is given by:

$$\begin{aligned}\chi(m_{\gamma'}) &= 2.9\cdot 10^{-15}\sqrt{\mathrm{SNR}}\left(\frac{t}{1\mathrm{s}}\right)^{-1/4} \\ &\left(\frac{T}{100\mathrm{K}}\right)^{1/2}\left(\frac{\kappa(m_{\gamma'})}{0.1}\frac{(Q\cdot\mathcal{G})(m_{\gamma'})}{50000\cdot 0.3}\frac{V}{447\ \mathrm{liter}}\frac{m_{\gamma'}}{\mu eV}\frac{\rho_0\epsilon(m_{\gamma'})}{\mathrm{GeV/cm}^3}\right)^{-1/2} \quad (2.30)\end{aligned}$$

From a spectrum obtained by a single instantaneous acquisition, the scan for the hidden photon signal can be performed over the noise power of a single spectrum. The averaging of these single spectra decreases the noise power by a factor of $1/\sqrt{N}$ with N is the number of the single spectra or number of acquisitons during a science run. Hence he sensitivity of the averaged spectrum increases[2] by the factor of $N^{1/4}$.

During the science run of the experiment, the haloscope type experiment allows the resonator tuned to shift the resonant frequencies. Thus in each acquisition, the profile of the gain changes with respect to the new resonant frequencies. The gain of the averaged spectrum is given

$$(Q\mathcal{G})_{\mathrm{averaging}} = \frac{1}{N}\sum_j\sum_i(Q_{i,j}\mathcal{G}_{i,j}). \quad (2.31)$$

With $(Q_{i,j}\mathcal{G}_{i,j})$ is the gain of the resonance j at the acquisition i with the total number of measurements is N. On the sensitivity, the averaging process decreases χ by the factor of $\sqrt{N}$ as the noise floor decrease with the same factor. The result sensitivity of the averaged datas is:

$$\chi(m_{\gamma'})_{\mathrm{averaged}} \propto \left(\frac{\sigma_{\mathrm{single}}}{\sqrt{N}}\frac{N}{\sum_j\sum_i(Q_{i,j}\mathcal{G}_{i,j})}\right)^{1/2} \quad (2.32)$$

$$\sim \frac{N^{1/4}}{\left(\sum_j\sum_i(Q_{i,j}\mathcal{G}_{i,j})\right)^{1/2}}. \quad (2.33)$$

[2]The increase of sensitivity mean the lower value of χ the experiment can constrain.

Chapter 3

On WISPDMX - The Hidden Photon Detector

Abstract

From the theoretical foundation of the haloscope type experiment mentioned in the previous chapter, the WISPDMX (WISP Dark Matter Experiment) was created as an experiment searching for the hidden photon cold dark matter in the broadband mass range up to 2.07 μeV. WISPDMX operates at room temperature but still achieves sufficient sensitivity with the high efficiency and sensitivity as a result of the acquisition system and the amplification factor from the resonant cavity. This chapter will present the grand structure of WISPDMX. Together with the development of the acquisition system, the frequency calibration system, and the acquisition system followed up by the detailed information of each component.

3.1 WISPDMX Components

The WISPDMX experiment is located in the Institut für Experimentalphysik of Hamburg Universität. The first development started in 2013. Fig. 3.1 shows the reduced setup of the WISPDMX with the resonant cavity and two tuning plungers. WISPDMX consists of three primary systems: The mechanical system (MS), the frequency calibration system (FCS), and the acquisition system (AS). Fig. 3.2

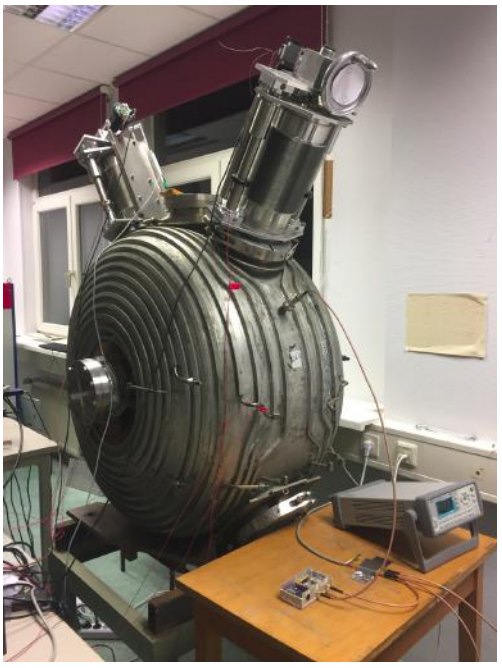

FIGURE 3.1: A photo of WISPDMX experiment with the 208 MHz resonant cavity with two modified plungers. The experiment is located at Institut für Experimentalphysik of Hamburg Universität, Hamburg.

shows the schematic structure of WISPDMX with the three aforementioned component groups. The mechanical system includes the mechanical components of the experiment: the resonant cavity, the two plungers with the gearbox, and two stepper motors. The frequency calibration system provides the information of the resonant modes during the tuning, and data taking, It measures the critical coupling of the magnetic loop antenna. Finally, the acquisition system plays an essential role in recording the broadband spectrum of the cavity field at very high resolution. Table 3.1 shows the components and functions of each system previously mentioned.

3.2 The Mechanical System

The mechanical system consists of the 208 MHz resonant cavity, two plungers and their driving motors. This section presents the structure of each component and the simulation for the understanding of the field configurations of the cavity. The simulation not only reveals the field structure at the resonant modes, but also provides their behaviours during the plungers tuning.

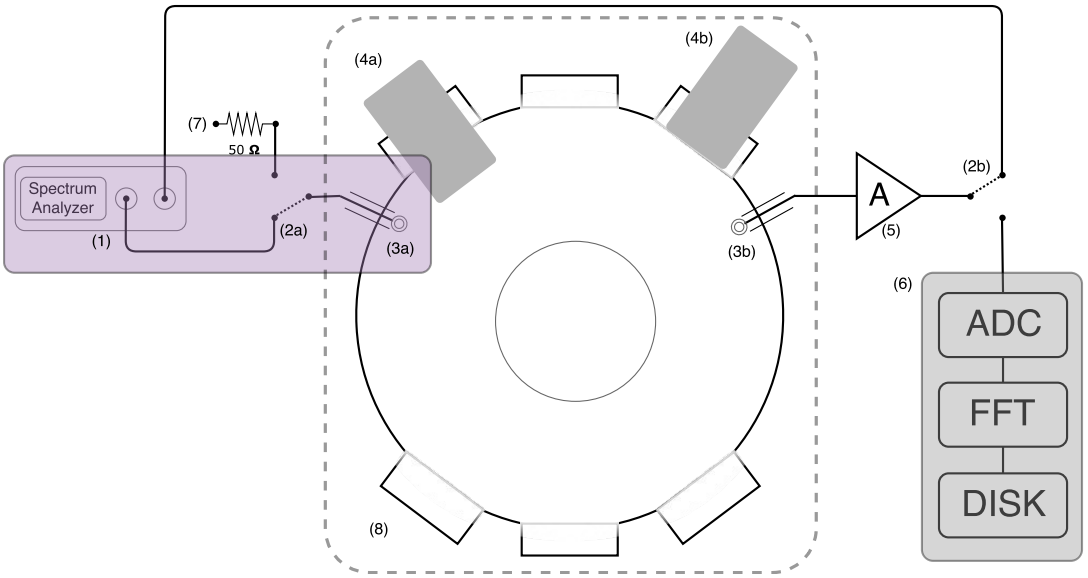

FIGURE 3.2: Schematic diagram of the WISPDMX, divided into three groups. **The Mechanical Components** (box with dash-line border) contain the 208 MHz cavity designed for SPS accelerator (8), and two tuning plungers (4a, 4b). **The Frequency Calibration System** (the blue box) contains radio switches (2a, 2b), Spectrum Analyzer (1), and two loop antenna ($L1$ and $L2$ as 3a and 3b) coupled with the cavity. Moreover, **The Acquisition System** (the gray box) contains the antenna $L2$, amplifier chain of 80 dB (5), ADC (Alazar ATS9360), and the CUDA FFT Unit (Nvidia GPU) (6). The antenna (3b) and the amplifier chain are shared between the calibration system and acquisition system.

TABLE 3.1: The components and missions of three main groups of component in WISPDMX.

	Components	Function
Mechanical System	- Cavity - Two plungers with gearbox - Stepper Motors	- Medium of the conversion - Frequency Tuning
Frequency Calibration System	- Magnetic loop antenna - Cables - Amplifier chains - Network Analyzer - Spectrum Analyzer	- f_i, Q_i tracking. - Antenna development - Measure the antenna coupling
Acquisition System	- Magnetic loop antenna - Cables - Amplifier chains - Analog Digital Digitizer - GPU	- Acquire the cavity spectrum. - FFT
Additional Component	- Radio switches and driver. - Power supply - Host computer - Thermometer	- Control signal flow to FCS or AS. - Powering the stepper motors. - Controlling driver and interface. - Record temperature.

3.2.1 The Cavity

The resonant cavity of WISPDMX was first designed as a 200 MHz resonator for the SPS Accelerator at CERN, and later modified into a 208 Mhz resonator used in the acceleration ring of HERA experiment [108–110]. WISPDMX utilizes the 208 MHz version of the resonant cavity. The 208 MHz HERA resonance cavity is made by the similar technique of the SPS, the two cold-form copper shells with the nose cone line are welded together to form the main body. The main body has a diameter of 96 cm and a volume of 447 liters, with the wall thickness of 8 mm to 10 mm at the nose cone. There are six ports created by cold-forming with the diameter of 20cm and oriented perpendicular with the former beam-line axis. These six ports were used to install the tuning plungers and powering couplers (Fig. 3.1 and Fig. 3.3).

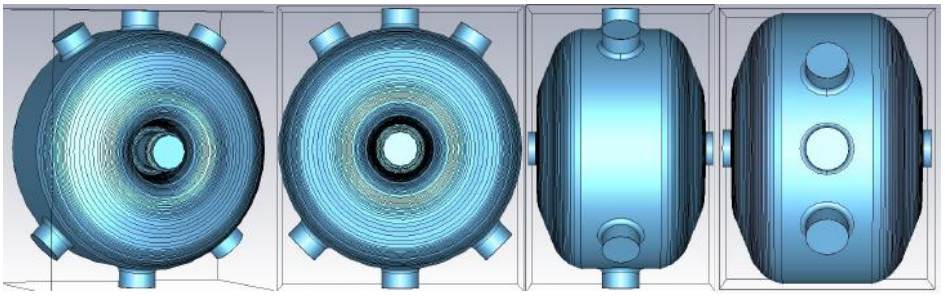

FIGURE 3.3: The 3D rendering image of the 208 MHz resonant cavity at different view angles. The simulation study in CST uses this model for further calculation.

The inner surface of the cavity, and the joint surface of the injected ports are polished to maintain the high electromagnetic reflectivity (Fig. 3.4). The water-cooling pipes are welded to the outer walls of the cavity to dispense the heat from the cavity wall during cavity operation for particle acceleration. However, the cooling pipes are not used for the current stage of WISPDMX.

FIGURE 3.4: The photo of the inner surface inside the cavity. The surface is polished to maintain the high electromagnetic reflection, one can see the two nose cones preserved for the beam line.

In the frequency of interest below 500 MHz, there are ten resonant modes (Table 3.2 - TE and TM are the acronyms of Transverse Electric Mode and Transverse Magnetic Mode) with four of them are highly sensitive with the hidden photon field. Any deformation of the cavity due to ambient temperature and atmospheric fluctuation could lead to a noticeable shift of these resonant frequencies.

TABLE 3.2: The ten resonant modes in the range of 500 MHz. The resonant frequency of each mode is calculated with the FCS[1].

Mode	**Frequency (MHz)**
TM_{010}	207.992 ± 0.002
TM_{011}	314.875 ± 0.002
$TE_{111\text{-}1}$	321.639 ± 0.002
$TE_{111\text{-}2}$	322.688 ± 0.002
$TM_{110\text{-}1}$	390.987 ± 0.002
$TM_{110\text{-}2}$	392.278 ± 0.002
$TE_{210\text{-}1}$	397.843 ± 0.002
$TE_{210\text{-}2}$	399.020 ± 0.002
TM_{020}	455.074 ± 0.002
TM_{012}	461.730 ± 0.002

A test on the temperature dependence has been conducted by monitoring the resonant frequencies of four modes: $\mathrm{TM}_{010}, \mathrm{TE}_{111\text{-}1}, \mathrm{TE}_{111\text{-}2}, \mathrm{TM}_{020}$. Without cavity tuning, the four modes are monitored continuously in 24 hours with the FCS. The cavity is located in the laboratory with the heater turned off to get rid of the temperature fluctuation from the heater's operation. Outside of the laboratory, the temperature decreased until the morning of the day after. The day-night temperature variation gradually changes the laboratory's temperature and leads to the contraction/expansion of the cavity and causes the resonant frequency shift. There are three thermosensors attached to the outer wall of the cavity to track the cavity's temperature. The reference temperature is the average of the three thermosensors's output. Fig. 3.5 shows the progression of four resonant frequencies when the temperature decreases and decline when the temperature increases. The isolating walls of the laboratory significantly reduce and delay the influence of outside temperature change. Whenever the temperature of the laboratory decreases, the cavity contracts and thus leads to the variation of the resonant frequency into higher value, and vice versa in case of expansion. The shifting rate of each mode is given in Table 3.3.

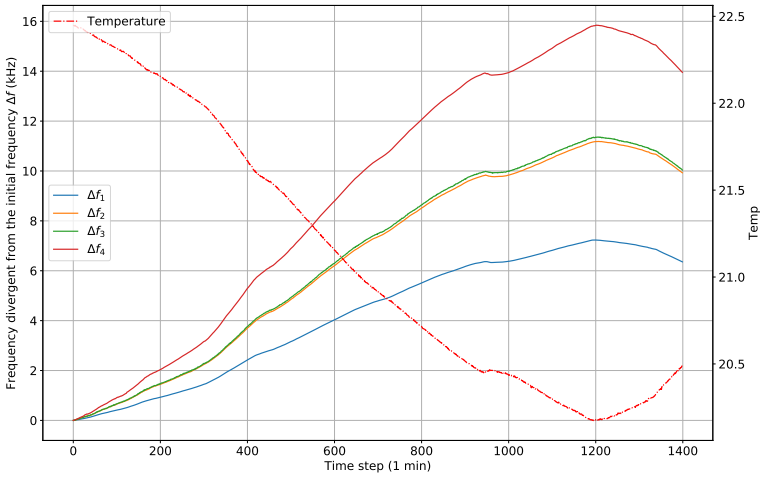

FIGURE 3.5: The ambient temperature shift in compare the resonant frequencies shift. The Δf_i stands for the shifting of the four modes to their initial value: $\mathrm{TM}_{010}, \mathrm{TE}_{111\text{-}1}, \mathrm{TE}_{111\text{-}2}, \mathrm{TM}_{020}$.

TABLE 3.3: The shifting rate (kHz) of each resonant mode per Kelvin.

Mode	**Shifting Rate (kHz/K)**
TM_{010}	3.2 ± 0.1
$TE_{111\text{-}1}$	4.9 ± 0.2
$TE_{111\text{-}1}$	5.0 ± 0.2
TM_{020}	7.0 ± 0.3

3.2.2 The Tuning Plungers

The primary function of the plungers in WISPDMX is to tune the resonant frequencies. With the insertion of plungers, the field inside the cavity is deformed and (mostly) tuned into higher frequency, allowing the search of hidden photon at higher masses. WISPDMX uses two plungers for tuning. The plungers are installed into the cavity via the preserved insertion ports in the main body of the cavity. The Institute of Experimental Physics modeled the plungers. The plungers are manufactured by Mechanical Workshop, Hamburg Universität. The inner rod is made from polished copper which distorts the cavity field with the tuning range from 0 mm to 110 mm. The aluminum outer shield covers the tuning rod and works as a frame of the plunger. The entire plunger is solid-built and even ready to work in vacuum condition. The gearbox, placed on top of the plunger, controls the inner cylindrical thread to push the inner rob to cavity. The inner rod moves in/out 1 mm for every four rotations of the motor/handle. The gearbox is attached to a handle for manual control and shares the same axis with the stepper motor (Trinamic QSH6018). The stepper motor has 200 steps per revolution (1.8° for a step angle) but can be driven at 2000 micro steps at 5% accuracy. Fig. 3.7 is the 3D rendered image of the plunger, the Fig. 3.6 shows one of two plungers. Fig. 3.1 shows the final setup of the WISPDMX with two plungers on two insertion ports.

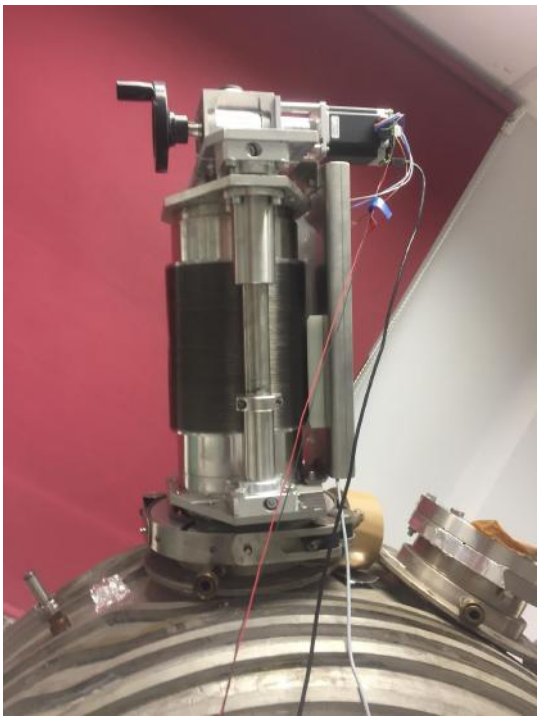

FIGURE 3.6: One of the two plungers used for tuning the cavity. The handle and the stepper motor are attach directly to the gearbox located on the top of the frame.

FIGURE 3.7: The 3D rendered photo of the plunger. One can see the inner rod in blue color, the plunger frame, and the gearbox on the top.

During the calibration of the first plunger, a small fault has been detected in the operation of the first plunger: the gear-slip caused by imperfect gears placement. A potential meter is used to measure the slip, the gearbox moves the plunger to

an arbitrary position and returns to the initial position with the same number of rotations. The gear-slip causes the shift of 0.1-0.2 mm from the initial position, and the slip happens at the turning point where the gearbox changes the turning direction. The solution for the gear-slip is elementary: the slip occurs at the turning point after the plunger did its insertion, by turning the plunger to negative position (e.g., -1 mm) and having the second slip at negative position before traveling back to the initial position. The two gear-slips are automatically canceled.

3.2.3 Simulation in Computer Simulation Technology

The simulation of the cavity and the plungers is implemented in the simulation program Computer Simulation Technology (CST). The CST uses the Finite-Difference Time-Domain (FDTD) as a numerical analysis technique used to computational electrodynamics. Since it works in the time domain, FDTD solutions covers a wide frequency range within a single simulation and treats nonlinear material naturally. The CST Microwave Studio (CST MWS) is the framework which is used to perform the simulation. The most powerful tool of CST MWS is its time domain solver. Generally, the time domain solver is faster and takes less memory as compared to frequency domain solver. It is important to note that the speed and memory requirements for computation may vary for diffrent structure and its complexity. In some cases, the frequency domain solver takes less time than other depending on the transient behavior of the excitation source, or number of eigen modes. The following steps show the process of the simulation:

1. Modeling of the object and setting up boundary conditions of the model. CST offers a wide range of modeling tools and accepts 3D input from well-known modeling applications.

2. Creating the mesh grid for the FDTD with either types of mesh's geometry: hexahedron or tetrahedron. The mesh density affects the quality of final result significantly, and a higher density means higher accuracy of the field during simulation. However, the computation time eventually increases as the density increases.

3. Choosing the solver and exporting the results. The solver solves the Maxwell's equations on each mesh cell and depends on the geometry of the simulated model.

For WISPDMX, the model used in the simulation is the SPS 200 MHz resonator with the simple cavity walls and the plungers with no frame and gearbox. Fig 3.8 shows the 3D modeling of the cavity and its cross-section with two plungers at the initial position and at the depth of 150 mm.

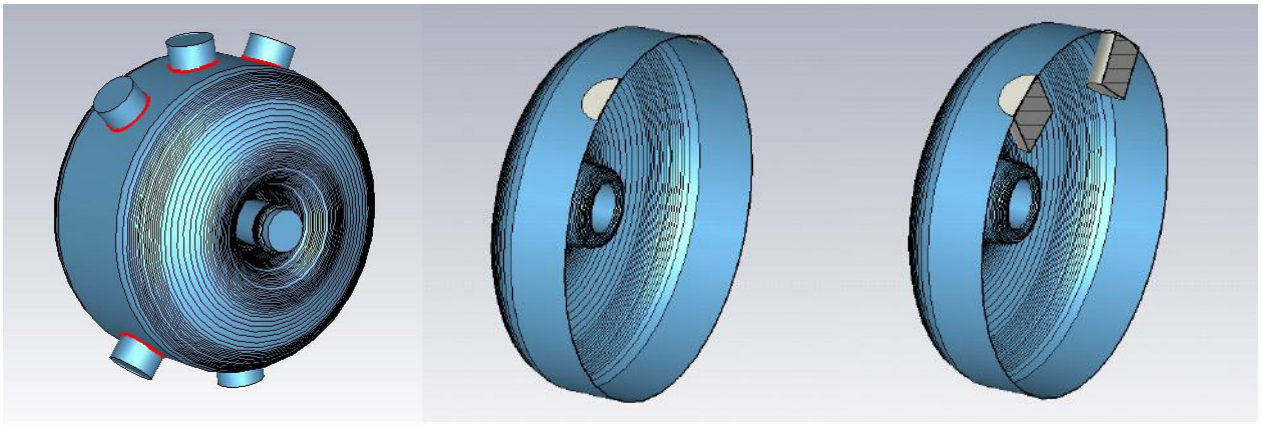

FIGURE 3.8: **Left**: The cavity model created in the CTS for simulation. One can see the six insertion ports where the tuning plungers or the power couplers could be inserted **Middle**: The simple cavity model for simulation with two plungers at the zero positons. **Right**: Similar to middle model but with two tuning plungers at a depth of 150 mm.

The WISPDMX has two plungers installed on the two top ports at $35°$ and $-35°$. There are two inputs for each simulation run: the depths of plunger I and plunger II. The range of plunger depth is from 0 mm to 150 mm, with each step size of 10 mm leads to a total of 16^2 simulation runs. The mesh grid is created locally inside the cavity but neglected outside of the cavity to reduce calculation cost. The mesh density is increased at the edges and sharp corners of the model to achieve high precision of field calculation, for each simulation run there are more than 5000 mesh cells created. Fig. 3.11 shows the mesh grid created for the middle model of Fig. 3.8. The output of each simulation run is ten resonant frequencies of the modes located in the 0-500 MHz together with their equivalent electromagnetic field configuration. The electric field structure determines the sensitivity of a resonant mode to the hidden photon field. Meanwhile, the magnetic field structure provides an insight to the field density inside the cavity and supports the study of antenna location for optimal coupling.

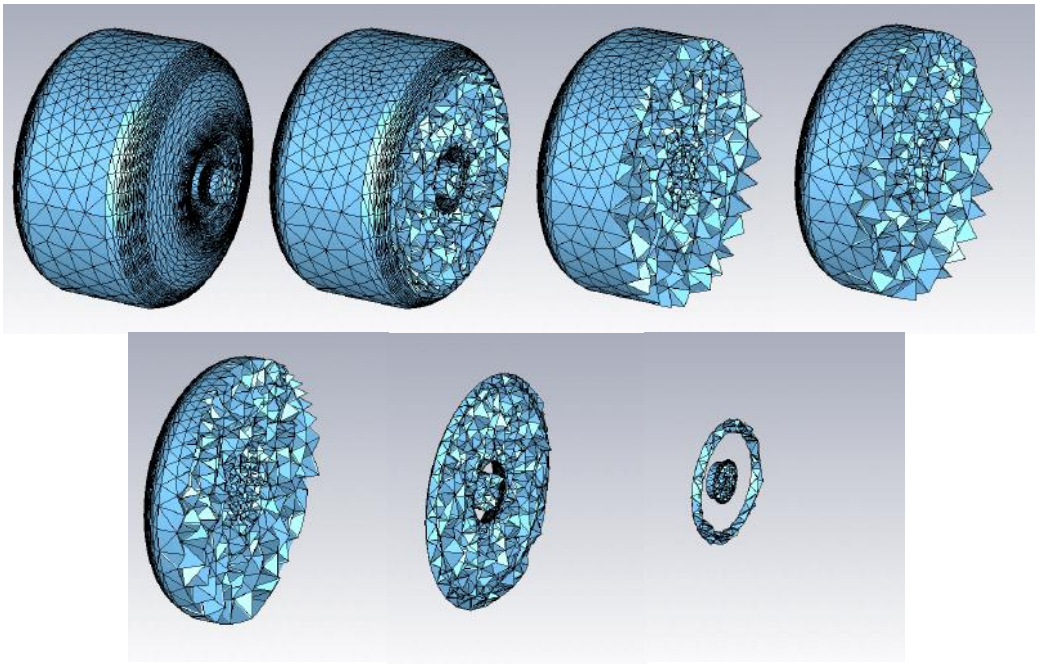

FIGURE 3.9: The mesh grid of middle model given in the Fig. 3.8.

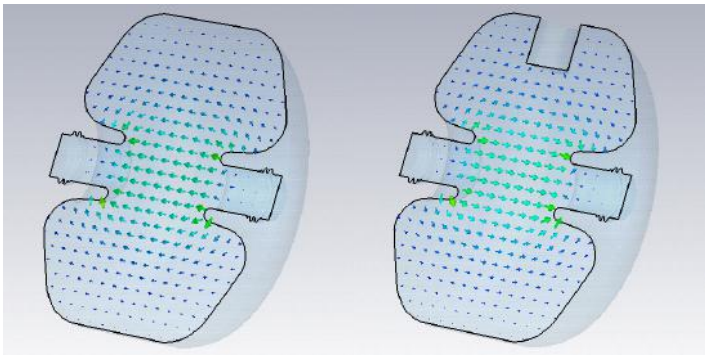

FIGURE 3.10: The electric field configuration of TM_{010} with the plungers's position of (0,0) and (150,150). The reference models are middle and right model in Fig. 3.8.

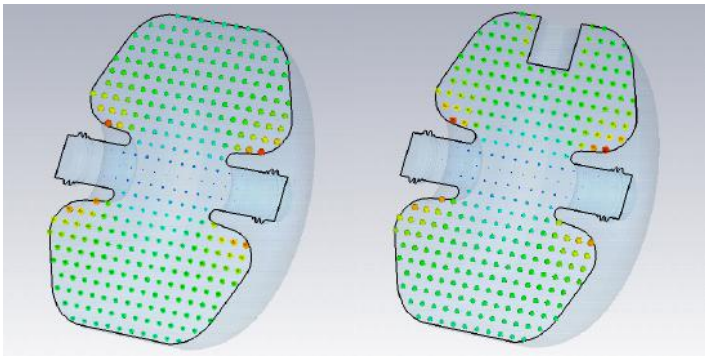

FIGURE 3.11: The magnetic field configuration of TM_{010} with the plungers's position of (0,0) and (150,150). The reference models are middle and right model in Fig. 3.8.

Despite the fact that physical working depth of plunger is 0 mm to 110 mm, the simulation input of plunger depth is extended up to 150 mm to exploit any possibility of field enhancement sensitivity.

3.2.4 Results From Simulation and Measurement

The preliminary results are used to scan for the frequency location of actual resonant modes at the position (0 mm,0 mm) of the plungers. The result from the simulation of 200 MHz cavity with plunger depths at (0 mm, 0 mm) and measurement are given in Table 3.4. One can see the difference from simulation and measurement result which arise from input model of the simulation: the 200 MHz resonant cavity of SPS while the measured cavity is 208 MHz. However, the results of 208 MHz cavity could be inferred from simulation's result by scaling the output from the simulated model due to their similarity in geometry. The modes TM_{111}, TM_{110}, and TM_{210} are decoupled into two modes with different polarizations, and their locations are fairly close, the simulation does not realize the split due to fact that the solver treats each mode independently. On the other hand, the output of these modes still apparently shows correct evolution of each mode during the tuning.

TABLE 3.4: The frequencies of the ten resonant modes as outputs from simulation and results from measurement.

Mode	**Simulation**	**Measurement**
TM_{010}	199.2039 ± 0.0001	207.992 ± 0.002
TM_{011}	293.4276 ± 0.0001	314.875 ± 0.002
$TE_{111\text{-}1}$	308.4336 ± 0.0001	321.639 ± 0.002
$TE_{111\text{-}2}$	308.4381 ± 0.0003	322.688 ± 0.002
$TM_{110\text{-}1}$	387.58757 ± 0.00001	390.987 ± 0.002
$TM_{110\text{-}2}$	387.58930 ± 0.00003	392.278 ± 0.002
$TE_{210\text{-}1}$	388.49400 ± 0.00006	397.843 ± 0.002
$TE_{210\text{-}2}$	388.49798 ± 0.00004	399.02 ± 0.002
TM_{020}	430.66557 ± 0.00003	455.074 ± 0.002
TM_{012}	452.8291 ± 0.0007	461.73 ± 0.002

The electric field configuration is used to calculate the form factor $\mathcal{G}$ using the formula:

$$\mathcal{G}_i = \frac{|\int dV \mathbf{E_i}(\mathbf{x}) \cdot \hat{\mathbf{n}}|^\mathbf{2}}{V \int d^3\mathbf{x} |\mathbf{E_i}(\mathbf{x})|^\mathbf{2}}, \tag{3.1}$$

with i is indicating the resonant mode. The grand simulation with a total of 16^2 runs, with each run producing ten electric field configurations. With a total of 2560 value of $\mathcal{G}$, one can see which resonant modes are sensitive to the hidden photon field. The hidden photon sensitive modes are set under the scope of the comparison between the simulation and measurement. Within the range from 100 MHz to 500 MHz there are four out of ten modes which are sensitive to the hidden photon: TM_{010}, $TE_{111\text{-}1}$, $TE_{111\text{-}2}$ and TM_{020} given in the Table 3.5. At the lower position of the plungers, the hidden photon sensitivity of six other modes increase as the depth of the plunger increase.

TABLE 3.5: The form factor $\mathcal{G}$ of resonance modes with different plunger setup. One can see there are four hidden photon sensitive modes: TM_{010}, $TE_{111\text{-}1}$, $TE_{111\text{-}2}$ and TM_{020}.

Plungers	**TM_{010}**	TM_{011}	**$TE_{111\text{-}1}$**	**$TE_{111\text{-}2}$**	$TM_{110\text{-}1}$	$TM_{110\text{-}2}$	$TE_{210\text{-}1}$	$TE_{210\text{-}2}$	**TM_{020}**	TM_{012}
0 - 0	**0.433**	0.000	**0.679**	**0.679**	0.000	0.000	0.000	0.000	**0.321**	0.000
0 - 110	**0.431**	0.09	**0.521**	**0.677**	0.035	0.000	0.000	0.000	**0.323**	0.018
110-110	**0.429**	0.1	**0.5204**	**0.622**	0.040	0.008	0.000	0.001	**0.324**	0.009
150-150	**0.428**	*0.1809*	**0.383**	**0.369**	*0.265*	*0.048*	0.000	0.001	**0.326**	*0.014*

The tuning of the cavity shifts resonant modes to different frequencies. It is not necessarily shift to higher frequencies but could lower the frequencies as well. The simulation provides estimates to understand the behavior of resonant modes during measurement. The subsequent measurement of these four modes is necessary to have a better understanding of the tuned field configuration and confirms the result from the simulation. As the plunger moves to the desired positions, the frequency of the four resonant modes is extracted using the FCS. The plunger is tuned with a step size of 10 mm and from 0 mm to 110 mm. As a result from the symmetry of the two plungers positions, it is needless to turn two plungers to a position which yields the same field, e.g., 20 mm of plunger I and 50 mm of plunger II produces the same field as 50 mm plunger I and 20 mm plungers II. The simulation's result from a 200 MHz cavity is scaled to compare the result with measurements of the

208 MHz cavity. The scale factor is given by the formula:

$$f_j = \frac{f_0(\text{200 MHz cavity simulation})}{f_0(\text{208 MHz cavity measurement})} \times f_j(\text{200 MHz cavity simulation}). \quad (3.2)$$

The scaling is necessary because the geometry of the real 208 MHz cavity is not known to a sufficient accuracy to predict the resonant frequencies. One can assume the scaling is intolerable despite of the similarity in geometry of two models. But it is important to keep in mind that simulation is to study mainly the field configuration and obtain the evolution trend of resonances during tuning. Fig. 3.12 shows the comparison of the resonant frequencies between simulation and measurement. The difference is larger at high tuning position but shows a similar evolution trend of frequency shift for varying the postions of the plungers.

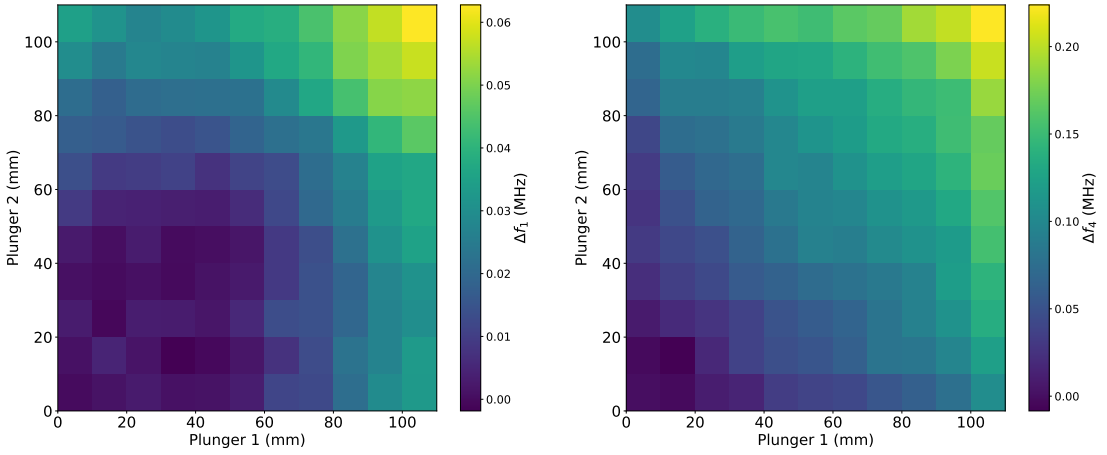

FIGURE 3.12: **Left**: TM_{010}. **Right**: TM_{020}. The comparison between the results from simulation and measurement, the quantity shown in the color bar is given by $\Delta f = f_{\text{measurement}} - f_{\text{scaled-simulation}}$.

The measurement also confirms the simulated results of the quality factor Q. During the frequency calibration, the fitting of Lorentzian functions to the resonant spectrum returns the resonant frequency and quality factor of the mode. In the measurement, a loop antenna under coupling with the cavity is connected to the cavity and measure the field amplitude as a function of frequency. The weakly coupled antenna ensures that the quality factor is preserved. Table 3.6 shows the quality factor from simulation and measurement. One can see that the measurement result has a good agreement with the simulation's with relative derivation below 5%. Section 3.3 explains further details on the Lorentzian fitting function and the antenna coupling state to quality factor.

TABLE 3.6: The quality factor of four important resonant modes resulted from simulation and measurement.

	$\mathbf{TM_{010}}$	$\mathbf{TE_{111\text{-}1}}$	$\mathbf{TE_{111\text{-}2}}$	$\mathbf{TM_{020}}$
Simulation	53082	62076	62080	47920
Measurement	55405 ± 6	59772 ± 9	58896 ± 114	44338 ± 2

The measurement of the cavity with multiple plunger positions also provides the optimal tuning scenario which the four hidden photon sensitive modes cover the widest frequency range. The optimal scenario is so-called the "L-shape" where plunger I is tuned from 0 mm to 110 mm, and consecutively plunger II from 0 mm to 110 mm. In this optimal track, the four modes cover a range of 1.07 MHz, 5.161 MHz, 3.782 MHz, and 3.794 MHz respectively. Table 3.7 shows the resonant frequency of four modes at different positions of plunger, and the frequency range these modes cover.

TABLE 3.7: The resonant frequency of the four hidden photon sensitive modes at the begining, middle, and the end of the "L-shape" scenario.

Plungers (I-II)	$\mathbf{TM_{010}}$	$\mathbf{TE_{111\text{-}1}}$	$\mathbf{TE_{111\text{-}2}}$	$\mathbf{TM_{020}}$
0 mm-0 mm	207.992 ± 0.002	321.639 ± 0.002	322.688 ± 0.002	455.074 ± 0.002
110 mm-0 mm	208.532 ± 0.002	318.13 ± 0.002	323.196 ± 0.002	456.916 ± 0.002
110 mm-110 mm	209.062 ± 0.002	316.478 ± 0.002	319.214 ± 0.002	458.8677 ± 0.002
Range	1.07 ± 0.003	5.161 ± 0.003	3.782 ± 0.003	3.794 ± 0.003

Fig. 3.13 shows the evolution of the four hidden photon sensitive modes during the plungers tuning following the "L-shape".

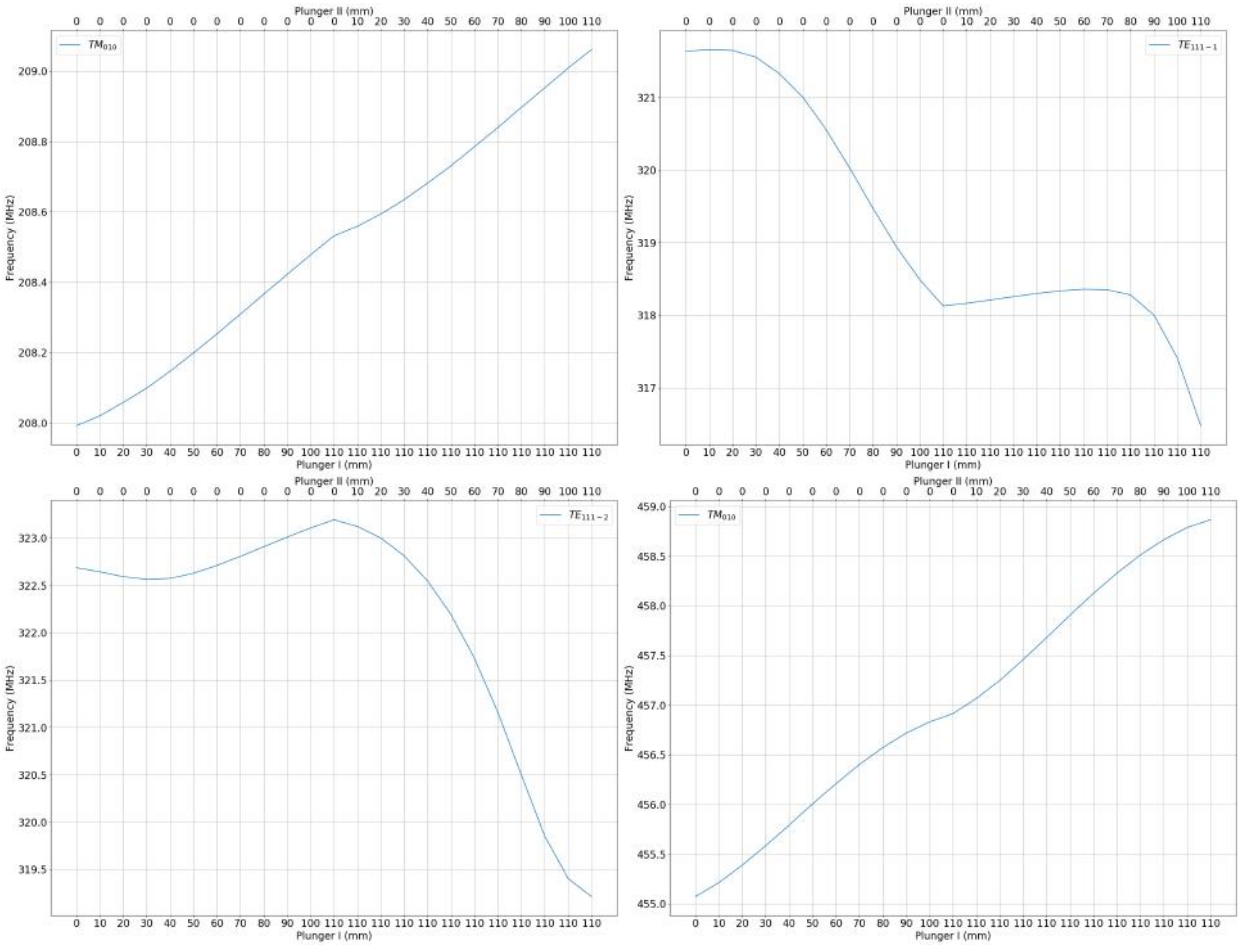

FIGURE 3.13: The evolution of four hidden photon sensitive modes concerning the position of two plungers which is tuned following the "L-shape".

In this section, one can see that the mechanical system is the heart of WISPDMX and irreplaceable obviously. The study on simulation is essential to learn about the field behaviors during tuning and to collect the electric field configurations to calculate the form factor $\mathcal{G}$. The tuning measurement strongly confirmed the result from simulation despite the setback on adoption of 200 MHz cavity modeling.

3.3 Frequency Calibration System

In the last section on the mechanical system, one can realize the plunger tuning and ambient factor (room temperature, atmospheric pressure) could shift the resonant modes and decrease the sensitivity of the experiment. Monitoring the resonant modes is essential and results in many inputs for later signal search, these are

the targets for the development the frequency calibration system (FCS). Antenna calibration and development are also one mission of the FCS.

3.3.1 Setup of the Frequency Calibration System

The schematic setup of the FCS in WISPDMX is shown in Fig. 3.2. It contains a spectrum analyzer with tracking function (Rohde-Schwarz FSP7), two magnetic loop antennas, and the amplifier chain. However, the development of FCS also covers the study of antenna coupling to the cavity, and an antenna development which required a network analyzer (Anritsu 73769A). To characterize the feedback of cavity at resonance, one can send and record a trackable signal to the cavity from either a network analyzer or a spectrum analyzer with tracking function. The observed parameter is the transmission or S21. On the contrary, the coupling between probe/antenna and cavity can only be exploited by network analyzer (spectrum analyzer does not record reflected signal) - observed parameter is the peflection or S11. The coupling previously mentioned is handy in interpreting the proportion of the injected signal sent into cavity or received from the cavity. However, the spectrum analyzer is more efficient and has higher resolution in recording transmission parameter. Hence the spectrum analyzer is used in the science run of the WISPDMX. The network analyzer has advantage in recording and analyzing the reflection parameter is adopted into the development of antenna. In general, the FCS has two main developments depend on target parameter. Fig. 3.14 shows the schematic setup to measure transmission parameter (S21) and reflection parameter (S11).

3.3.2 Transmission Parameter: Quality Factor and Resonant Frequency Tracking

The setup of transmission measurement is: The sweep signal (at -20 dBm) is send from spectrum analyzer (with tracking function) to the cavity. The response signal is pickup by the magnetic loop antenna, amplified by amplifier chain, and sent to the input of the spectrum analyzer. The spectrum analyzer collects 10 sweep-and-record spectrums at the resonance with resolution of 300 Hz, then averaging and exported into disk. Fig. 3.15 shows the output of the spectrum analyzer after at each resonant mode.

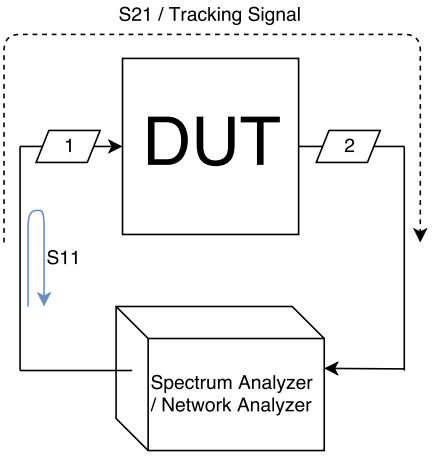

FIGURE 3.14: The general setup to measure transmission or reflection parameter. DUT is a technical term for Device Under Test, for WISPDMX, DUT is the cavity-antenna complex.

The load quality factor -Q_0- of the cavity range from 30000 to 70000 for different resonant modes, the quality factor primarily depends on resistive skin losses of the inner plating surface. The oscillating electric field of the resonance penetrates copper wall, for a classical conductor at room temperature, the electrons behaves classically, the penetrating depth is given by

$$\delta = \sqrt{\frac{2\rho_{\text{copper}}}{\omega\mu_{\text{copper}}}} \tag{3.3}$$

with ω is the angular frequency of field ($\sim 2\pi \times 10^8$ Hz), ρ_{copper} is the resistivity of copper $1.68 \times 10^{-8}\Omega m$, and μ_{copper} is the permeability of copper ($1.26 \times 10^{-6} H/m$). At TM_{010} of the cavity at 208 MHz, skin effect depth is 4.5 μm while in higher mode TM_{020} at 454 MHz, skin effect depth is 3.06 μm. The unload quality factor at TM_{010} (208 MHz) can be estimated as:

$$Q_0 \sim \frac{\mu_0 V}{\mu_{\text{copper}} S \delta_{208\text{ Mhz}}} \tag{3.4}$$

One can estimate the volume of cavity is $0.44m^3$ and total surface of $\sim 3.3m^2$. The expected Q_0 at room temperature is approximately ~ 30000.

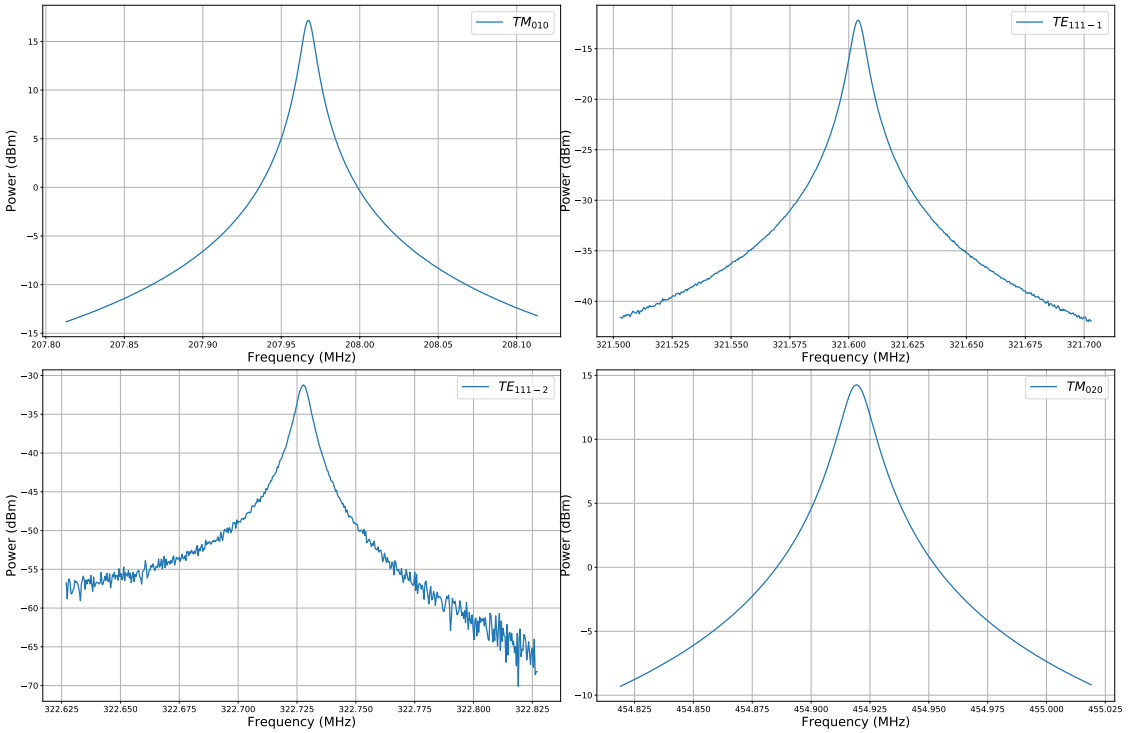

FIGURE 3.15: The average spectrum output of four hidden photon sensitive modes. From these spectrums, the quality factor is obtained by fitting a Lorentzian function to sweep spectrum returned by the spectrum analyzer.

The quality factor could be obtained by several methods using the transmission measurement [111]: "3dB Method", "Resonance Curve Area Method", and "Lorentzian Fit". The Lorentzian Fit is chosen to calculate not only the quality factor but also resonant frequency (f_0). The power spectrum to frequency is fit to a Lorentzian profile given by

$$P(f) = \frac{A_0}{4\left(\frac{f}{f_0} - 1\right)^2 Q^2 + 1} + A_1, \tag{3.5}$$

where f_0 and Q are resonant frequency and quality factor of the mode, A_0 and A_1 as maximum power and constant background of the field after excitation caused by the sweep from spectrum analyzer. The curve fit is used to determine the value of f_0 and Q [2]. This method is substantially more robust in presence of noise and useful in a sense that the fit also returns resonant frequency which is an input for "3dB Method". The results from the fit have high accuracy and are very optimistic due to many sweeping points and spectrum averaging function (as noise reducing)

[2]The Lorentzian function given in 3.5 which can be used to fit the power spectrum. While the formula in [111] is used to fit the transmission parameter S21 output from a network analyzer.

of the spectrum analyzer. Fig. 3.18 shows the Lorentzian profile fit perfecly to the power spectrum of TM_{010} and TE_{111-1}.

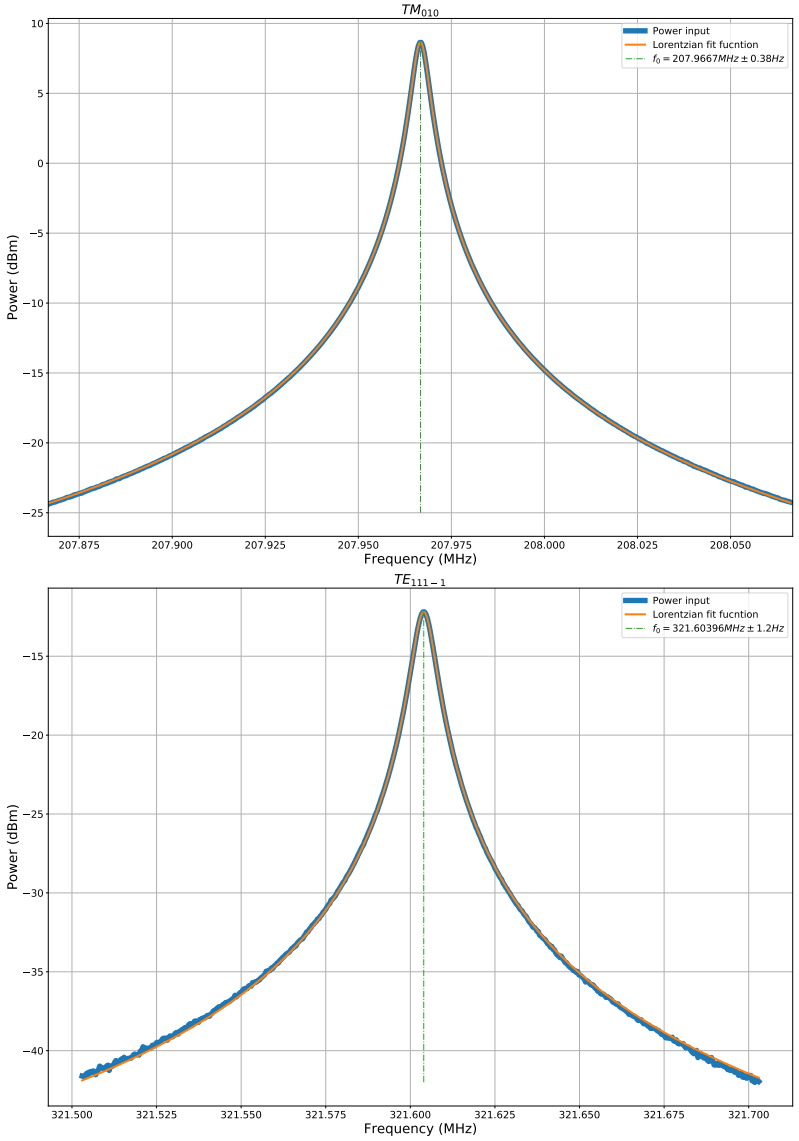

FIGURE 3.16: Lorentzian Fit on the sweeping spectrum at TM_{010} and TE_{111-1} from Fig. 3.15.

TABLE 3.8: The resonant frequency and quality factor of four hidden photon sensitive modes. The error from curve fit indicates high accuracy from the fit function and clean power spectrum data.

Mode	f_0 **(MHz)**	Δf_0 **(Hz)**	Q	ΔQ
$\mathbf{TM_{010}}$	207.992	0.38	46451.455	0.08
$\mathbf{TE_{111\text{-}1}}$	321.639	1.2	48693.477	0.23
$\mathbf{TE_{111\text{-}2}}$	322.688	1.01	51106.787	0.30
$\mathbf{TM_{020}}$	455.074	0.56	33955.64	0.05

Transmission measurement using spectrum analyzer is the latest development of FCS and currently applied in the science run of WISPDMX. The advantage of this approach provides the WISPDMX the ability to track the smallest change in the resonance frequency with high precision during the cavity tuning or under the ambient environmental factors. At the moment of writing this thesis, there is no downside on this setup apparently.

3.3.3 Reflection Parameter: Backbone of the Antenna Measurement

The power built-up inside cavity emerges from the injection of signal via antenna or, in the case of WISPDMX, the hidden photon is converted into electromagnetic radiation and excited the cavity. The antenna coupling κ is a quantity need to be determined or increased for higher sensitivity. The reflection parameter (S11) provides a method of measuring the strength of coupling between the probe and cavity's field. The S11 is the backbone of antenna development, but there is one point reader must take into concern that the noise generated by antenna or the insertion format of the probe to the cavity also play important roles on the endorsement of the antenna in a science run of WISPDMX. A noisy but high coupled probe would not be referred over a quite one. The coupling state of antenna with cavity allocated in three stage: under coupling (UC), critical coupling (CC), and over coupling (OC). In the CC, the probe collects half the energy from resonant mode and causes the broadening of resonant profile. In the language of the S11, at CC, there is no reflection when a signal is sent to the antenna, and antenna radiates full signal into cavity. The reciprocity symmetry ascertains the same gain and frequency for both transmitting and receiving behavior. Hence the CC state assures that the probe collects most of possible signal/energy from cavity.

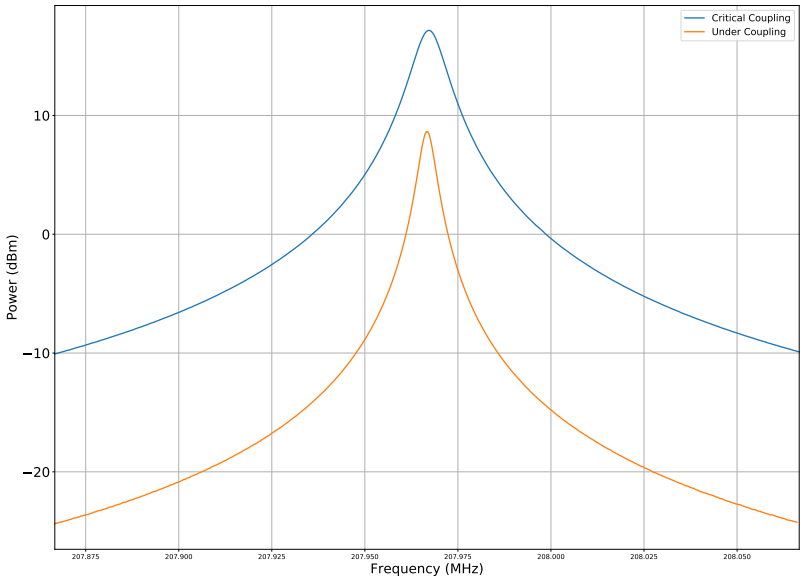

FIGURE 3.17: The Lorentzian profiles of TM_{010} at Critical Coupling and Under Coupling of the antenna.

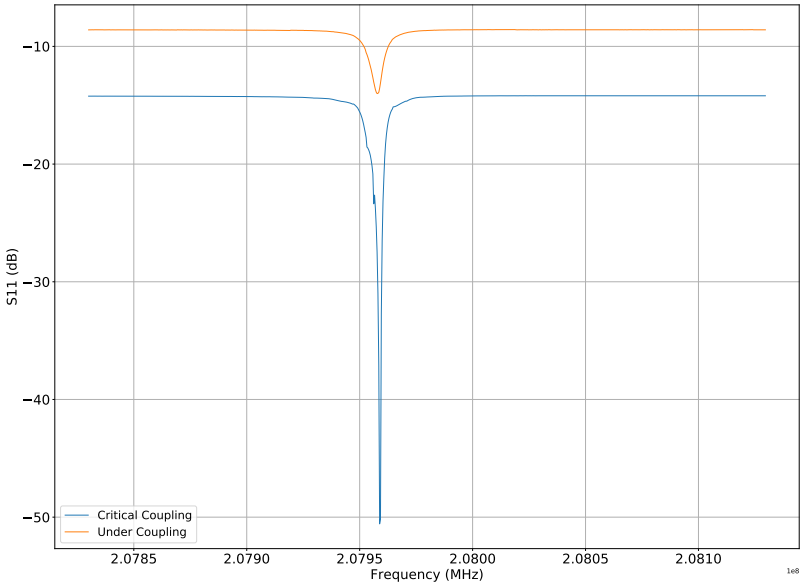

FIGURE 3.18: The reflection parameter S11 of TM_{010} at Critical Coupling and Under Coupling of the antenna.

The coupling factor κ required to calculate the hidden photon and photon coupling χ could be infered from here. The coupling factor has the maximum value of 0.5 at Critical Coupling (as the probe draws half of energy built-up inside cavity) and equivalent to this, S11 must be close to 0. The coupling factor is given by

$$\kappa = 0.5 \times (1 - \text{S11}). \tag{3.6}$$

The type of probe used in WISPDMX is the magnetic loop antenna. The signal received by the antenna is enhanced if a higher magnetic flux flows through it. The CST simulation output provides the magnetic field configuration so one could obtain a geometrical position of probe for the higher sensitivity. Fig. 3.19 shows the magnetic field lines of TM_{010} and TE_{111-2}, the magnetic field lines of the TM_{010} and TE_{111-2}'s are perpendicular and parallel with beam axis. If an antenna is fed to cavity in the area indicated by the red box, and the loop's plane is perpendicular with the field line of TM_{010}, the gain of the antenna for TM_{010} is larger than the TE_{111-2}. Hence, one can create a probe critical coupled with TM_{010} but under coupled with TE_{111-2} and vice versa. This inconvenience results in multiple sciences runs with different antenna setup.

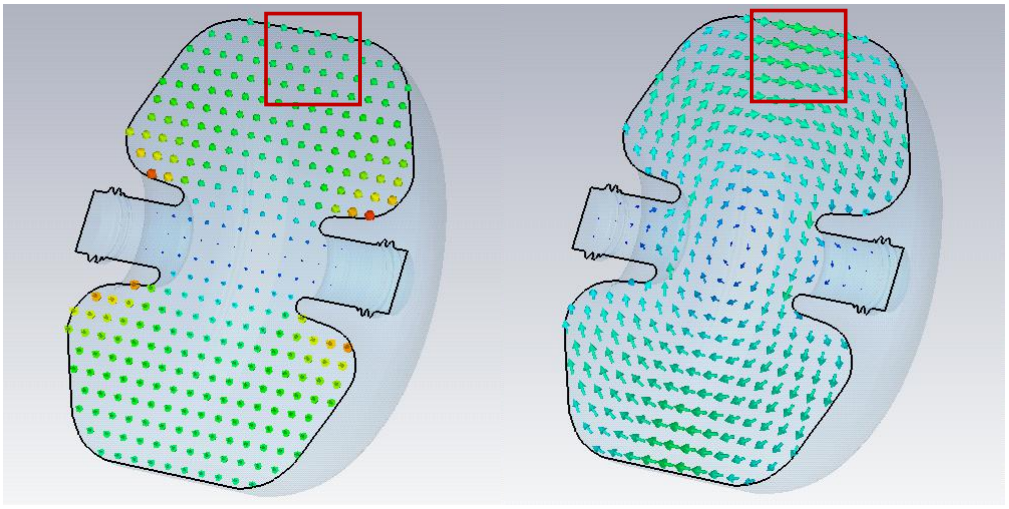

FIGURE 3.19: The magnetic field configuration of TM_{010} and TE_{111-2}. The indicated red box is the region where antenna is fed into cavity. The magnetic field lines in the red box of TM_{010} are perpendicular to beam axis while in other modes, the magnetic field is parallel with the beam axis.

3.3.4 Antenna Design

There are three main developments for an optimal antenna of WISPDMX. Fig. 3.20 shows the three main antenna designs for WISPDMX experiment: AN-1, AN-2, AN-3, and the antenna AN-0 is built to calibrate the 208 MHz cavity. Fig. 3.20 shows four representative antennas previously mentioned.

The **AN-0** is the antenna arrived together with cavity, it is solid built and connected to a the N-output flange which can be connected to the antenna port preserved in the body of cavity. The antenna loop is made from cooper with the diameter of 1.2cm, the end of the loop is grounded to the wall of the cavity.

The AN-0 has the broadband coupling (homogeneous coupled with all over the frequency) with the cavity. However, the geometrical shape of the AN-0 is a disadvantage of this antenna, which its loop does not fully position inside the cavity (Fig. 3.22). The shallow length of antenna causes the decreasing of magnetic flux and reduces the coupling of AN-0 antenna, notwithstanding the S11's response is moderately beneficial.

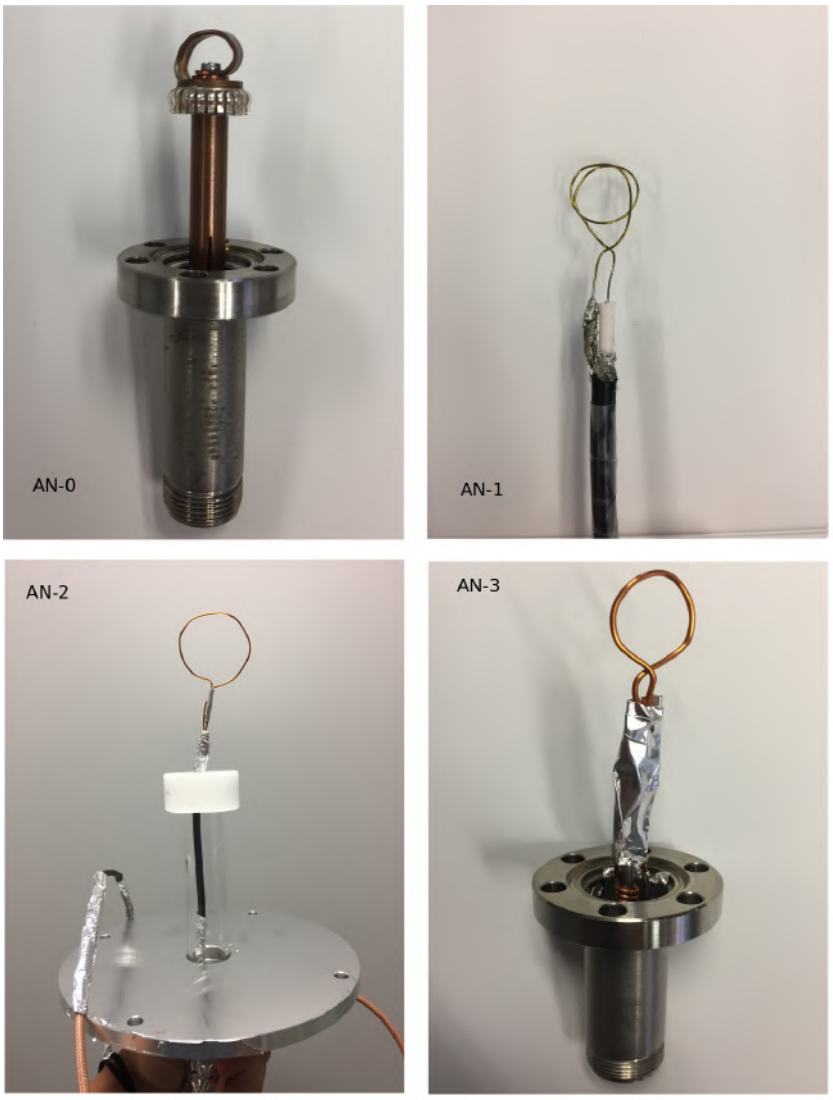

FIGURE 3.20: The four antennas used in the development of the WISPDMX: AN-0, AN-1, AN-2, and AN-3.

The AN-1 is the first development of a magnetic loop antenna to increase κ. The motivation of AN-1 is injecting the antenna deeper into the cavity to reach a higher flux and obtain CC state. The AN-1 is created by tearing away the outer insulation and metallic shield of a RG-59 coaxial cable, then the bare copper core

is shaped into a loop and connected to the metallic shield to form a closed system. The AN-1 locates itself at a deeper position than AN-0 and provide a higher signal (from the sweeping of network analyzer).

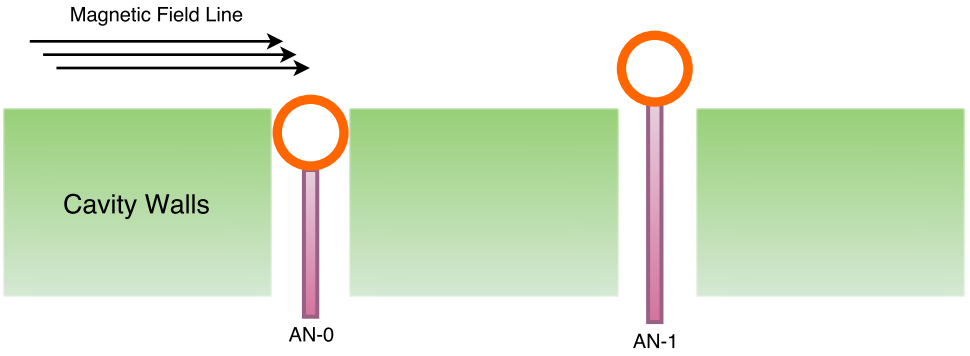

FIGURE 3.21: The relative positons of the AN-0 and AN-1.

The AN-2 is the next development of AN-1, AN-2 is a composition of antennas with each of them has different loop diameter. Notably, AN-2 is built with an "antenna plunger". One can inject the antenna into cavity and adjust either the depth of antenna or the direction of the loop to approach CC state. The "antenna plunger" has a flange to mount onto top port of the cavity.
Both of the AN-1 and AN-2 has a significant high coupling with resonances, but unfortunately, these antennas result in a spectrum with high noise floor (Fig. 3.22). The source noise could arise from :

1. The self-generated noise from antenna: the metallic shield connection with copper wire is fragile, small current travels through mesh wire could self-radiate (as micro loop antennas) and increases the noise floor in multiple frequencies.

2. The insertion method of the AN-1 and AN-2 is insecured and renders the cavity unsealed under stray electromagnetic field. The structure of AN-1 and AN-2 is one of the foremost reason that increases noise floor.

The sealed mechanism of the AN-0 could prevent the stray field entering into cavity. Furthermore, one can learn the structure of AN-0 to mimic the design of the next antenna.
The AN-3 is the hybird of between AN-0 and AN-1. The loop is created from the a copper wire and connected to the N-port-flange of AN-0. AN-3 provides

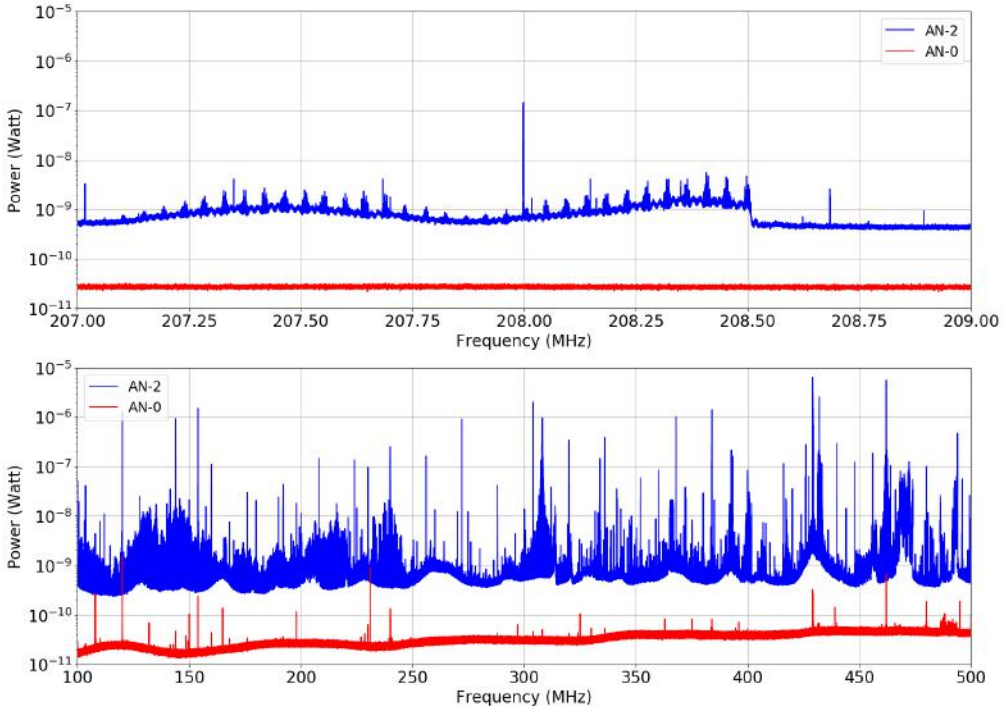

FIGURE 3.22: The spectrum of AN-0 and AN-2. One can see that AN-2 introduces into the power spectrum a significant amount of noise which decreases the sensitivity of WISPDMX by a factor of 10.

a remarkable lower noise power spectrum but still maintain high coupling. The AN-3's loop stands on the base of AN-0 which optimally blocks stray field from entering the cavity. Fig. 3.23 shows the power spectrum of AN-0 and AN-1 in which AN-3 produces a same level noise floor as AN-0, the noise peaks at 200 MHz is suspected to arise from the insecured connection between the loop and core of AN-0 base.

The reflection parameter plays an important role during the antenna development. However, noise performance of these antennas rejects several antenna designs from being used in the WISPDMX experiment. The main antenna used in the first science run is the AN-0. The principles of antenna design presented in this section have laid a foundation for future development of a high coupling and low noise antenna.

One can retrieve the κ of the AN-0 at the frequency below 500 MHz by measuring the reflection parameter of the AN-0. The κ is calculated from the equation 3.6. Fig. 3.24 shows the κ of the AN-0 to the frequency under 500 MHz.

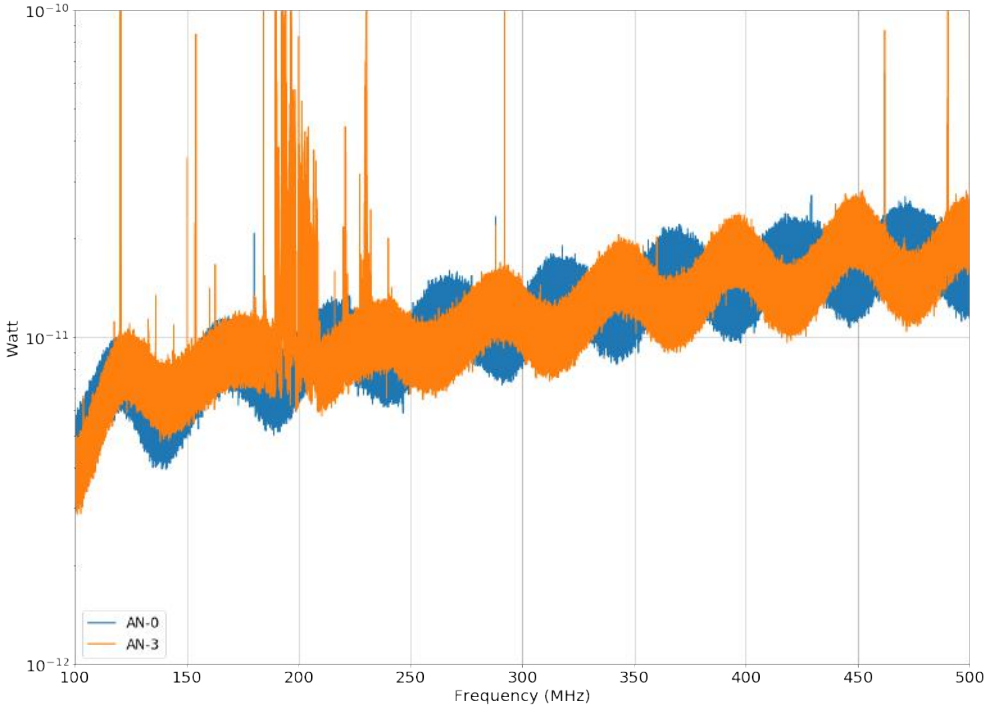

FIGURE 3.23: The power spectrum of AN-0 and AN-3. One can see the noise floor is significant reduced.

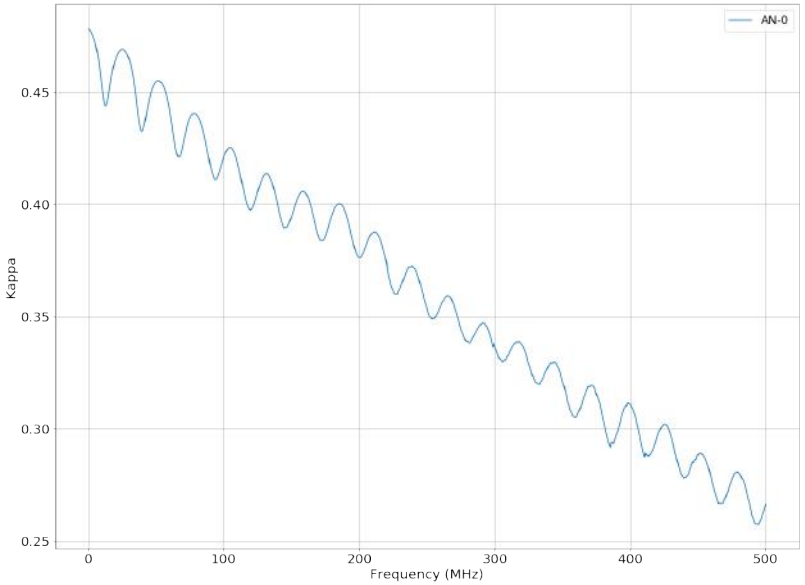

FIGURE 3.24: The coupling of the AN-0 to the cavity to the frequency under 500 MHz.

3.4 The Acquisition System

The acquisition system (AS) is the most important group of components which acquiring the power spectrum of cavity's field. The signal from the magnetic loop antenna is amplified by two room temperature low noise amplifiers, WBA0105-45R and WBA0105B, with a overall gain of $80dB$, noise figure $NF = 0.518$ [3]. After amplification, the signal is fed through a 1m coaxial cable to input of the digitizer. The digitizer converts the analog voltage signal in the output to digital sample with the sampling rate of 1GS/S[4]. After 10 seconds of acquisition, the data is transfered to GPU for Fast Fourier Transform (FFT) at resolution of 50 Hz. The final sum spectrum is exported to hard drive for offline data analysing. Diagram 3.25 presents the structure of AS.

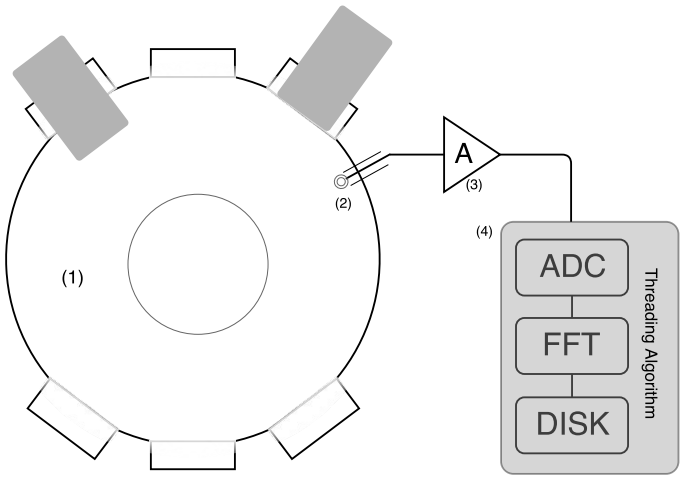

FIGURE 3.25: The simplify diagram on the structure of the acquisition system.

3.4.1 The Central Signal Digitizer

An off-the-rack ADC has built-in memory and on-board FFT processor provides direct output spectrum. From analog input signal to the final FFT power spectrum, the entire operation regularly follows three following steps:

1. Converting the analog signal to digital signal is the main function of an ADC. The output samples stored in a memory buffer represents time-domain evolution of the input signal. An acqusition with higher bit rate (BR) and

[3]The calculation of the noise figure is given in the Appendix A
[4]the prefix **M** and **G** denotes a factor of 10^6 and 10^9 respectively.

sampling rate produces the smoother digital signal. The bit rate increases SNR[5] of the ADC given in the following formula: SNR = 6.02 BR + 1.76 dB.

2. Storing the buffer on device memory: the number of samples can be stored proportional to memory size. A higher sampling rate fills device memory faster.

3. Fast Fourier Transforming: the sample buffer in time-domain is transformed into frequency-domain and constructs the frequency/power spectrum. The CPU or FPGA board could perform transformation.

The common ADC in the market has three features built-in. However, the WISPDMX's requirement of a high-resolution broadband spectrum output demands an essential upgrade from the common one to a tailored signal digitizer. WISPDMX's acquisition system has the Alazar ATS9360 modified by manufacturer to stream the data directly to host memory which can store up to 20 GS with a sampling rate of 1 GS/s (20 seconds of acquisition returns 40 GBytes of data). Subsequently, data at the host memory is streamed to GPU. Inside GPU, the CUDA-powered function prepares an extended buffer for FFT-CUDA. The FFT-CUDA transforms the prepared buffer into frequency domain. Finally, a spectrum stacking function sums the spectrums, returns it to host memory, and exported to disk. The accelerated CUDA-FFT together with others CUDA-powered functions are specialized in the intensive array manipulation which significantly reduces the time of each process. The schematic diagram of the system is illustrated in Fig. 3.26. The introduction of GPU separates the traditional linear work managed by host CPU into the parallel and repeated processes managed by GPU.

[5]The SNR of the ADC mentioned here is understand as the dynamic range of ADC

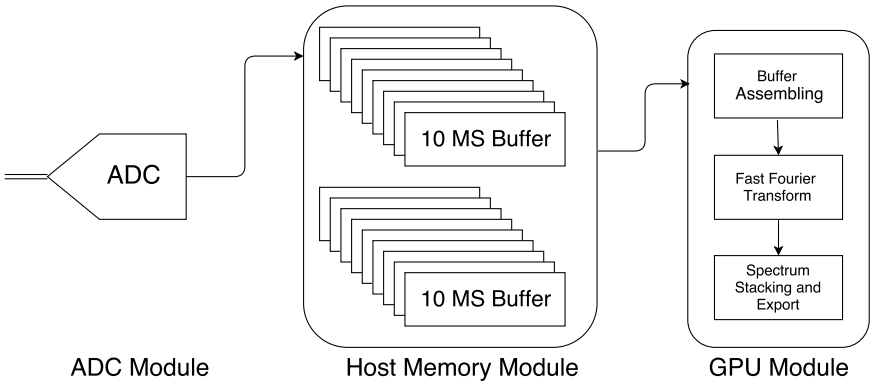

FIGURE 3.26: Schematic Diagram of the acquisition system. The ADC converts analog input signal into the digital signal at sampling rate of 1 GS/s. The sample is streamed directly to host memory grid which is reformed into two memory grids. Once the memory grid is filled, GPU starts getting data from memory grid, assembles the sample arrays, FFT, and stacks the spectrums.

3.4.2 Output Data from ADC

At each acquisition, output data from the ADC (Alazar ATS9360) is streamed continuously to host memory. In general, the output contains all of the physical result embedded in the time domain samples. The data quality test is necessary to ensure the physical input from streamed sample from ADC to host memory can be reconstructed. The quality test contains three steps: 1) Send the input signal from a Signal Generator to input port of ADC. 2) Acquire the raw data from ADC and export into a independent binary file for later analyzing. 3) Recover time-domain data from raw sample and transform into frequency domain to obtain the spectrum of the input signal. The setup is given as follows:

1. A signal generator (Tektronix AFG 3252) sends a signal of at -10 dBm (or 200 mVolt peak-to-peak) [6] at the frequency of 1 MHz and 200 MHz to ADC input port.

2. The Alazar takes 20 MS at the sampling rate of 1 GS/s, and the 12-bit sample code is stored in the most significant bit of in 2-byte format. These 20 MS raw data are exported into a binary file.

3. Reconstruct raw data from the binary file into physical time-domain data, then transform into frequency domain as voltage/power spectrum. The signal read from spectrum is compared with output of the signal generator.

[6] $P = \frac{V^2}{2\times 50\Omega}$

The input range of ADC is ±400 mV and covered in the full 16-bit sample value, the data encoded inside the binary file has equivalent value for 400 mV and -400 mV are $2^{16} - 1$ and 0. Thus the physical value measured is proportional to the 16-bit value, conversion from direct output data to physical input given by

$$V = \frac{\text{16-bit value}}{2^{16} - 1} \times 0.8 \text{ Volt} - 0.4 \text{ Volt} \tag{3.7}$$

The reconstructed input signal of each measurement is given in the left panel of Fig. 3.27, the peak-to-peak amplitude of the 200 MHz signal is slightly lower than 200 mV caused by skin effect at a higher frequency while the amplitude at 1 MHz shows more identical value with output from the signal generator. An oscilloscope is connected to output side of the coaxial cable to measure the amplitude and power of the actual input which the ADC records, given in Table 3.9.

TABLE 3.9: The value of actual input recorded by ADC from a 200 mVpp from a signal generator. The skin effect at high frequency causes the power decline during transmission from signal generator's output to input port of ADC/Oscilloscope.

Frequencies	**1 MHz**	**200 MHz**
Mean (mVpp)	196.109	183.3
Min (mVpp)	192.7	180.7
Max (mVpp)	198.4	193.2
σ (μVpp)	699.2	772
Equivalent Power	$9.613 \cdot 10^{-5}$ W	$8.4 \cdot 10^{-5}$ W

The Fourier transform is applied to the time-domain data to recover the power of test signals. The result is given in the right panel of Fig. 3.27. The powers read at the designated frequency are $9.722 \cdot 10^{-5} Watt$ and $8.55 \cdot 10^{-5} Watt$ for a signal of 1 MHz and 200 MHz respective. The slight aberrations in the results (Table 3.9) is caused by the loss from cables and ports at the inputs of oscilloscope or ADC.

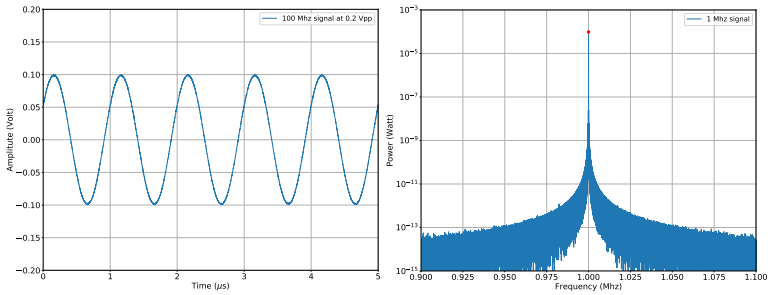

(A) **Left** The time domain and **Right** Frequency domain signal of 1 MHz signal at -10 dBm (10^{-4} Watt) power.

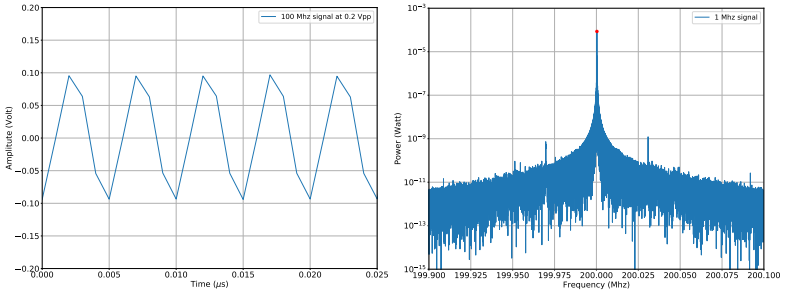

(B) **Left** The time domain and **Right** Frequency domain signal of 200 MHz signal at -10 dBm (10^{-4} Watt) power. The signal at high frequency losts their sinodial shape due to the low sampling rate.

FIGURE 3.27: The time domain output from the ADC is transformed into frequency domain as a power spectrum to inspect the quality of raw signal.

Despite of slight contrary, the raw output data from ADC has a good agreement with input signal and retains the physical characteristic of input. The test with input signal from a signal generator confirms the output data from ADC is well maintained before hitting GPU for parallel processing acceleration.

3.4.3 Data Handling Process

There are two main algorithms adopted to create the high-efficiency signal digitizer: large memory grid allocation and multi-threading. The massive memory grid is designed to stream the largest sample chunk possible (10MS) from the ADC to a buffer element of a memory grid. A grid of memory comprises of 1000 buffers takes up to 20GBytes of memory, which are equivalent to 10 seconds of acquisition. The program allocates two memory grid to optimize with the multi-threading programming. The threading is created to have one thread managing the ADC while the other handling the GPU, thread communication ensures the two threads can synchronize perfectly after any event finished in one thread. On

the memory management, the two thread share host memory for output storage of thread-I and input source of thread-II. In conclusion, the first thread (thread-I) administrates ADC and write data to memory, while the other thread (thread-II) waits and copies data from a memory grid filled from the first thread.
Fig. 3.28 presents the flow of data from ADC to host memory grid, and afterward to GPU for three 10-second-acquisition of AS before the ignition of acquisition, thread-I allocates two memory grid (Grid-I and Grid-II), and thread-II likewise starts the memory allocations in GPU. In the algorithm analysis below, the two bullet points of each acquisition present status of two thread simultaneously (graphical presentation given in Fig. 3.28).

1. First Acquisition

    - Thread-I: The ADC is having the analog input signal into digitized sample, sending a chunk of 10MS to Grid-I. The process takes approximately 10.01 seconds.
    - Thread-II: The thread and GPU are in idle mode, waiting for the first memory grid (Grid-I) to be filled.

2. Second Acquisition:

    - Thread-I: The ADC takes the new batch of data and fills the Grid-II. Before starting the second acquisition, thread-I has alerted thread-II via thread communication.
    - Thread-II: The buffer from the Grid-I is being copied to GPU. Until the final stack spectrum is exported, the total time is less than 4 seconds. The time break down is presented in Appendix B. After exporting the stack spectrum, the thread goes back to idle mode waiting for alert from thread-I.

3. Third Acquisition:

    - Thread-I: The ADC sends the sample directly and writes over Grid-I. Before starting the third acquisition, thread-I has alerted thread-II via thread communication.
    - Thread-II: After getting alerted by thread-I, thread-II, again, performs a similar task to the previous acquisition, but input data streamed from Grid-II.

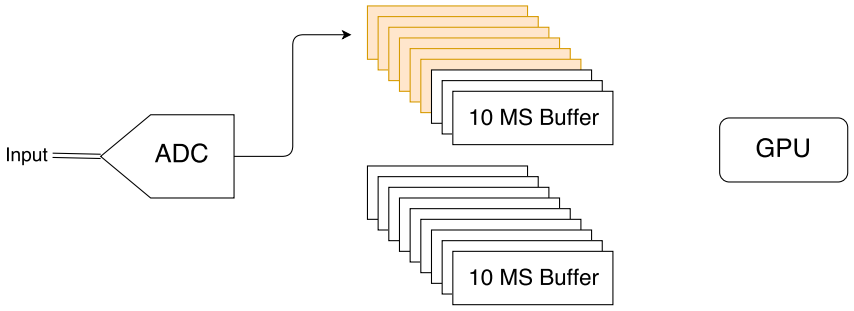

(A) The First Acquisiton.

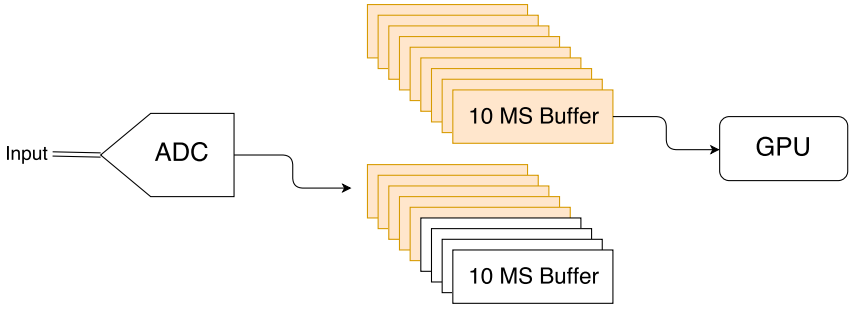

(B) The Second Acquisition.

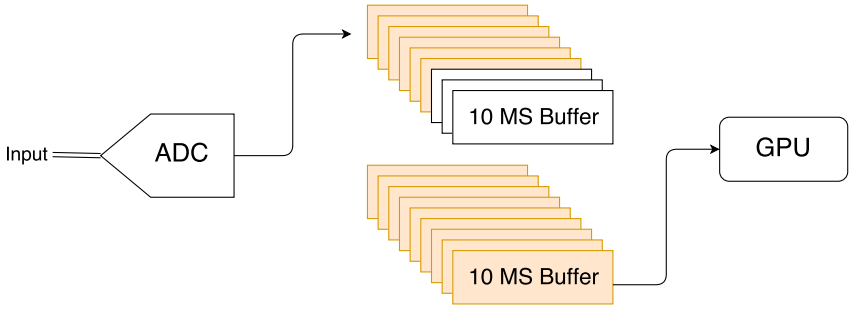

(C) The Third Acquisition.

FIGURE 3.28: The graphical representation on the application of multi-threading and memory management for the AS.

As one can see, the manipulation of the multi-threading and memory management has greatly increased the performance of the whole system with the starting point of a linear system. From an off-the-rack ADC, the ADC was revamped and tailored to a high-efficiency and approach a real-time system if one can get rid of the initialization process of ADC in each acquisition.

3.4.4 The GPU Acceleration

The combination of the ADC at a high sampling rate and GPU to yield a high-resolution broadband spectrum is **unique**. The acceleration is not solely from the multi-threading but also the advantages of the GPU. The Nvidia CUDA is

a parallel computing platform and programming model that enables a dramatic boost in computing performance. In the CUDA environment, a function must be initiated to divide the task and instruct thousand of CUDA cores, harnessing the parallelization computing power. In previous section, one has seen that thread-II transfers the samples from memory grids to GPU, after this step, it is necessary to decide the length of the FFT input. Depending on the designated resolution, the number of sample as an input for FFT must possess a particular length given by the formula:

$$\Delta f = \frac{f_S}{N}, \tag{3.8}$$

with f_S is the sampling rate, N is the number of samples. Therefore the sampling rate of 1 GS/S allows WISPDMX cover broadband range of 500 MHz. A 50 Hz to 10 Hz spectrum resolution requires an input of 20 MS to 100 MS. A more extended buffer can be constructed by accumulating multiple and sequential sample chunks. Fig. 3.29 shows the function "Buffer Assembling" creating a 20 MS buffer from two 10 MS chunks. The function instructs each CUDA core performs a "simple task" of copying samples from the chunks to the accumulating buffer.

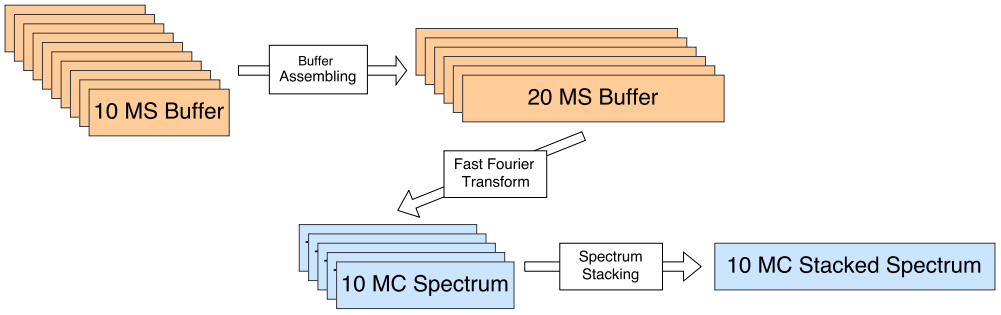

FIGURE 3.29: The algorithm chart of the processes in the GPU. There are three main CUDA-powered functions: The Buffer Assembling Function, CUDA-FFT Function, and The Spectrum Stacking Function.

After the assembling, the accumulated buffer is ready for transformation to frequency domain. The CUDA Fast Fourier Transform library (CUDA-FFT) provides the GPU-accelerated FFT implementations that perform up to 10-20 times faster than CPU-only alternatives. The CUDA-FFT transforms individually the expanded buffer into 10MC spectrums, as shown in Fig. 3.29 as the "CUDA-FFT Function".

Finally, the spectrums returned from CUDA-FFT are summed to form a stacked

one. The summing of multiple 10 MC arrays is a cumbersome task for a traditional CPU-based computation but simple for the GPU-type one. The function "Spectrum Stacking" (shown in Fig. 3.29) instructs the CUDA core to sum the value at the corresponding index from multiple spectrum. The stacked spectrum which contains the spectral information from input memory grid is exported to host-memory and saved to hard disk and ready for off-line analysing and signal scan. At this point, the full cycle of signal digitizer is completed and takes approximately 4.02 seconds (at conditions of 10 second acquisition and $\Delta f = 50$ Hz). A reader can reference Appendix B for the time break down of each GPU processes.

3.5 From Stacked Spectrum to Noise Reduction.

A radio receiver which is used to measure the average power of the noise coming from a radio telescope in a distinct frequency range is called a radiometer. The structure of WISPDMX receving system consists of a probe and acquisition system resembles a radiometer apparatus. The noise voltage recorded has zero mean and varies randomly on the short timescales. However, the noise power is always greater than zero and decreases when it is averaged over much longer times. The averaging of a considerable number of spectrums decreases the noise power following the Dicke Radiometry Equation:

$$\sigma_{\text{average}} = \frac{\sigma_{\text{single}}}{\sqrt{N}}, \tag{3.9}$$

with σ_{single}, σ_{average} are the noise power from a single spectrum and averaged spectrum respectively, and N is the number of single spectrums averaged. The Dicke Radiometry Equation can be applied to treat the noise in either time-domain (zero mean noise) and frequency domain. The averaged spectrum could be retrieved by dividing the stacked spectrum by the number of single spectrums. Hence the noise power of the average spectrum is $\sqrt{N}$ times lower than a single one. This is the main reason why the central signal digitizer of WISPDMX prefers to collects and stack multiple single spectrum for a lower noise in averaged spectrum. Fig. 3.30 shows the noise from a single spectrum, along with the averaged spectrums from averaging 100 and 500 single spectrums. One can see that the averaged noise floor decreases significantly by the averaging.

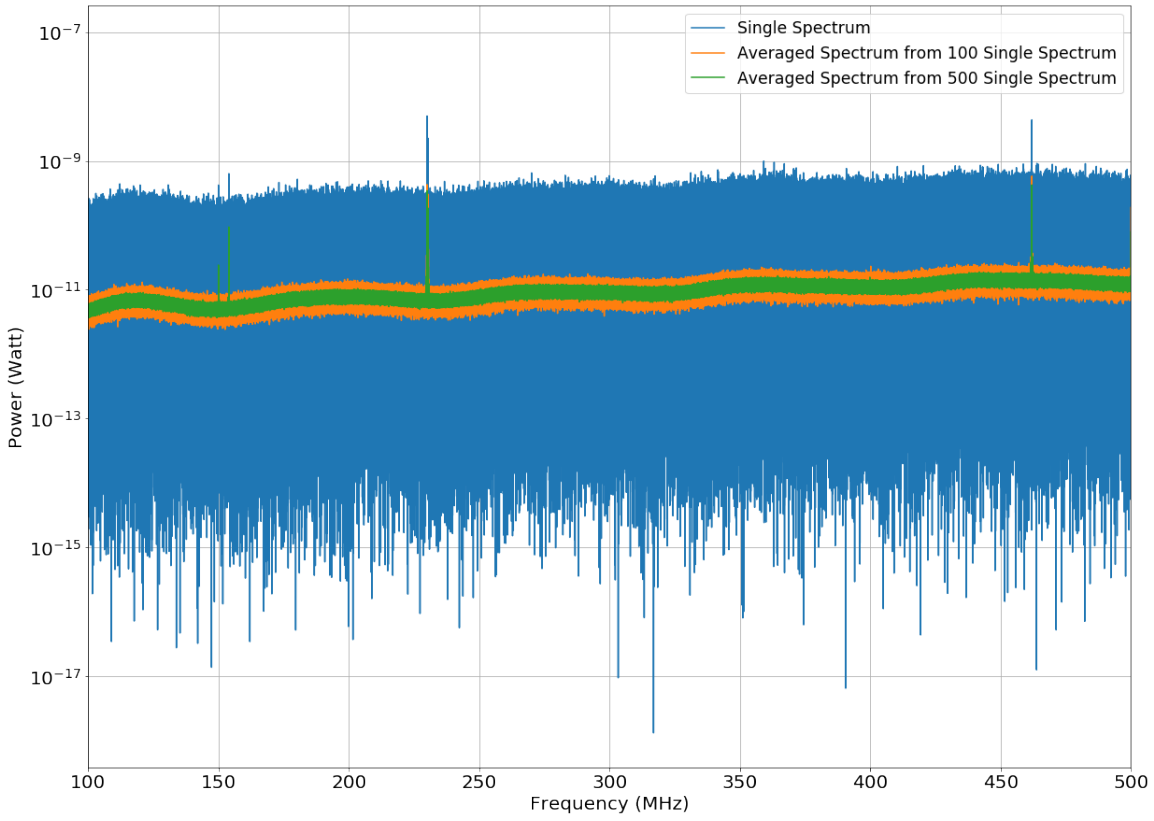

FIGURE 3.30: The power spectrum from a Single Spectrum, and two Averaged Spectrums created by averaging 100 and 500 Single Spectrums.

The noise power follows the Gaussian distribution. However, the noise distribution of a single spectrum has a long tail on the left due to the ADC quantization processes. This noise tail is eliminated during the averaging process, and noise power of averaged spectrum follows the Gaussian distribution nicely. Fig. 3.31 shows the distribution of the noise power of channels located within the range of 290 - 300 MHz. The noise power from averaging 100 and 500 single spectrums are $\sigma_{100} = 1.36 \times 10^{-12}$ Watt and $\sigma_{500} = 6.096 \times 10^{-13}$ Watt respectively. The fraction $\sigma_{100}/\sigma_{500} \sim \sqrt{5}$ follows equation 3.9.

WISPDMX does not only search for the hidden photon signal in the interest resonance but also the off-resonance and characterizes this frequency range. The spectrum of WISPDMX is a broadband spectrum with a range from approximately 0 Hz to 500 MHz, and with a resolution of 50 Hz or 10 Hz decides a single spectrum is 40 MBytes or 200 MBytes[7]. A science run of WISPDMX takes 22000 acquisitions, and at a current state of digitizing PC machine, storing a large number of high resolution spectrum is not efficient. Hence WISPDMX is limited to

[7]Table B.1 shows the results from several acquisition configuration is given in Appendix B.

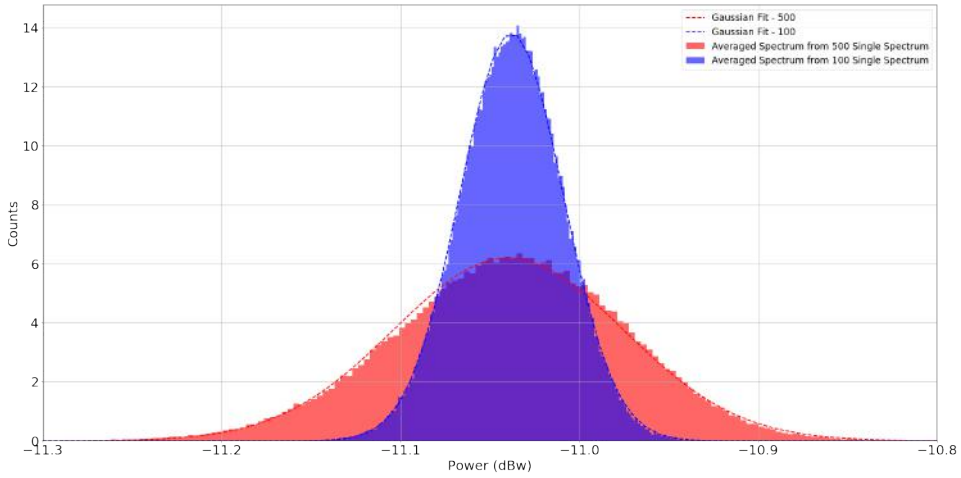

FIGURE 3.31: The noise distribution of the two spectrums obtained by averaging 100 and 500 independent single spectrums.

the frequency resolution of 50Hz, and an output spectrum is averaged from 500 single spectrums.

3.6 WISPDMX Data Taking

The designs and structures of the three main component groups have been presented. The final touch is to put these systems together to form the final apparatus ready for a science run. However, there is an important feature need to be presented. As mentioned in the previous section, one can see that FCS and AS use the same antenna and amplifier chain. Thus they share mutual output from the amplifier, a radio switch is added to alter the destination of the signal to ADC input of AS or spectrum analyzer input of FCS. There is an additional radio switch to cancel out the possible signal from the output of spectrum analyzer which could contaminate the cavity field. The control of three component system is assigned between two PC: an acquisition PC is the host system of AS, while other PC is managing MS, FCS, and radio switches. During the science run, after AS acquires data, MS tune the plunger to a new depth and the AS starts a new acqusition.
In previous section, the cavity tuning shifts the resonant frequency to a new value which is tracked by FCS. During the science run, FCS extracts the resonant frequency f_i and Q after a determined number of AS and MS run. The outputs of FCS and AS are stored into local hard drive and available for the offline signal scan and analyzing. Fig. 3.32 shows the grand structure of the three system previously mentioned. The executive module shows the recurrent loop of the first science run:

an FCS run after ten AS-MS iterations with MS tuning step-size of 10 microns, thus the FCS's step-size is 100 microns. By interpolation, the f_i and Q can be retrieved and field information on the resonances for each acquisition is obtained.

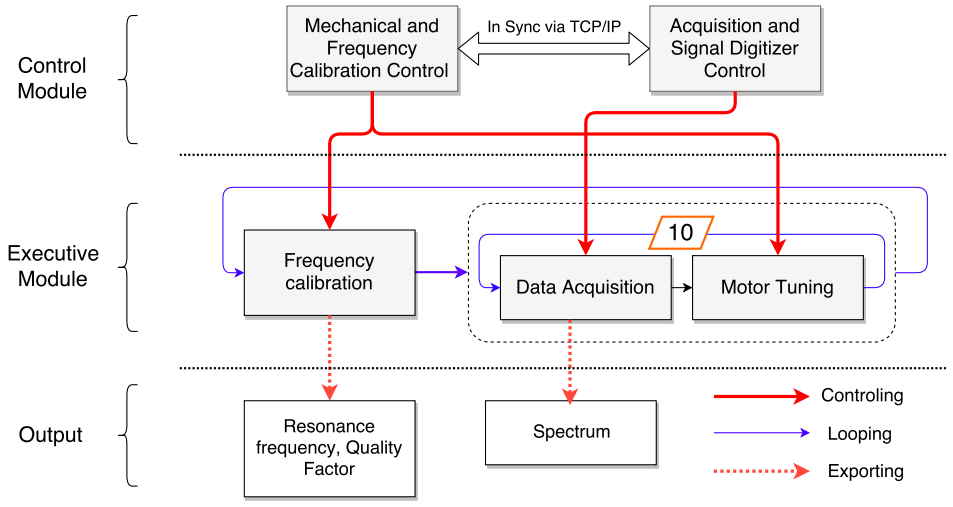

FIGURE 3.32: The final setup with the combination of the three system: MS, FCS, and MS.

Most of the electronic components in MS and FCS are routed back into a Windows desktop and controlled by the Labview. The Labview provides a wide variety of port communication library (GPIB, VISA, USB and Serial Communication), and smooth connections to multiple devices simultaneously. The Labview visual programming language is used to build the commanding and data handling VI for each device, these VIs are deployed into the central experiment controller. The central experiment controller in Labview not only includes most of the VIs developed for MS and FCS, but also establish the connection via TCP-IP with the Acquisition PC where the commands for each event are sent from thread-I. Fig. 3.33 shows the panel central experiment controler.

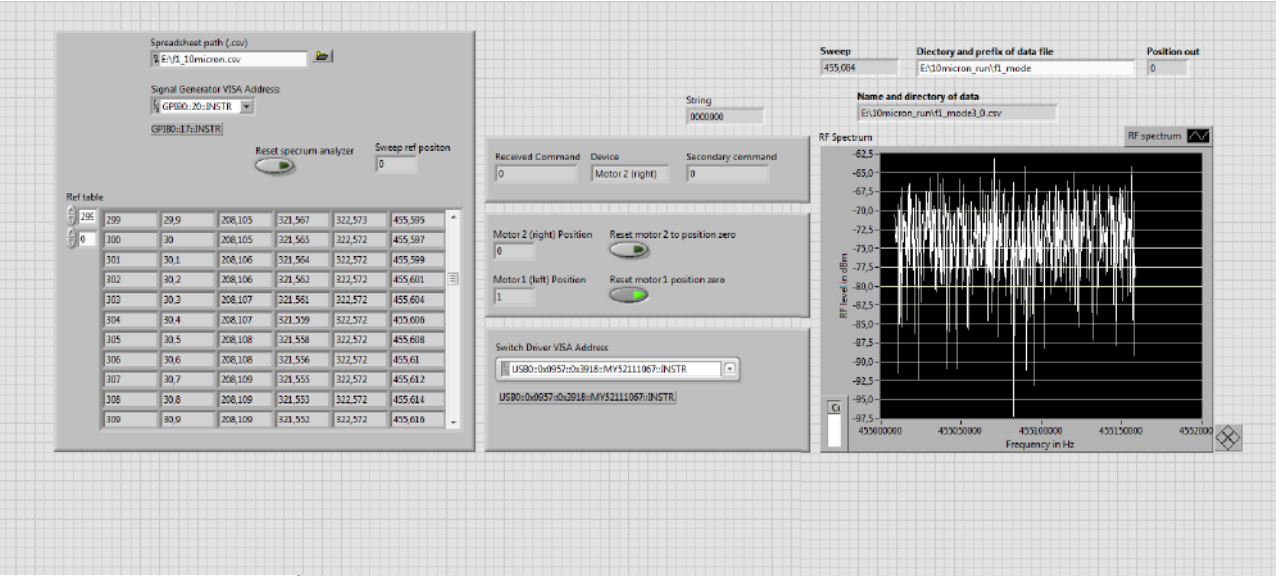

FIGURE 3.33: The panel of WISPDMX's central experiment controller. The Labview-programmed interface controls most of the electrical devices of the MS and FCS.

In conclusion, the three main component systems of WISPDMX and their related components have been created and developed. The final apparatus is ready for a science run and search for hidden photon signal. The development also results in a set of foundations for future development (antenna, central signal digitizer).

Chapter 4

The First Science Run of WISPDMX and Analysis

Abstract

The content of this chapter is about the data analysis techniques for detecting a hidden photon signal on- and off-resonance. The scan and analysis use the data taken from 23rd October 2017 to 2nd November 2017, as known as the first science run. The acquisition setup of the first science run is described in the first section. The second section will present the spectrum and noise characterization. The final section will discuss the scanning algorithm at on- and off-resonance regions of the single-acquisition spectrum and averaged spectrum from the first science run.

4.1 Dataset

The data used for the analysis and signal scan in this chapter are from the first science run of WISPDMX. The run was taken from 23rd October 2017 to 2nd November 2017 and contains a total of 22000 spectra. The first science run lasted for ten days, with 8 secondary runs, each comprise 2000 or 3000 acquisitions, the total acquisition time is 22000×10 seconds (2.46 days). The off acquisition time ($\sim$ 7 days) is spent for multiple activities: retake a secondary run because of a memory jam in the ADC, time for FCS and MS executions, electronic switch

operation, and break between two secondary runs. Each spectrum represents 10 seconds of acquisition at the sampling rate of 1 GS/S which leaves the broadband spectrum covering a range from 0 Hz to 500 MHz at a FFT resolution of 50 Hz for each channel.

On the first science run, WISPDMX was set at the controlled room temperature of $(20 \pm 1)^o$C. The step-size of the plunger is 10 μm with the tuning range from 0 mm to 110 mm. The signal from the cavity is picked up by the magnetic loop antenna AN-0, amplified with a factor of 80 dB before being recorded by the central signal digitizer. The FCS tracks the four hidden photon sensitive modes (TM_{010}, TE_{111-1}, TE_{111-2}, and TM_{020}) after every ten acquisitoion-mechanical runs. The dataset also contains 22000 spectra from AS, 2200×4 frequency calibration spectra from the FSC, and a log file that records events that occur during the science runs. Table 4.1 show the concise details on the setup of the first science run.

TABLE 4.1: General information on the first science run of WISPDMX.

Information on the first science run	
Name	**Value**
Duration	23rd Oct - 2nd Nov 2017
Acquisition time	61.11 hours
Secondary run	8 runs
Sampling rate	1 GS/s
Time per acquisition	10 seconds
Output resolution	50 Hz
Lab's temperature	$(20 \pm 1)^o$ C
Plunger range	0mm - 110mm
Plunger step size	10μm

TABLE 4.2: The dataset of the first science run.

Spectral Dataset from first science run				
Origin	**No. of Files**	**Format**	**Size**	**Structure**
AS	22000	Binary	40 MB	Header (String of 100 kB) + Data (10^7 Floats)
FCS	2200×4	CSV	11.5 kB	Frequency (500 Floats) + Power (500 Floats)

4.2 Data Processing

The processing and analysis of data are done using `Python2.7+Scipy+Numpy+Pandas`, the `Scipy` provides the statistical tools for the analyzing while `Numpy+Pandas` supports large array manipulation and calculation. WISPDMX does not follow any package for signal analysis, any new function is created for the purpose of each analyzing step. As mentioned in the previous section, the dataset contains two type of data (Table 4.2):

1. The broadband spectrum from the AS which has a high resolution where the signal scan is applied. The broadband spectrum is stored in the binary format with the structure of first 100-byte header, which contains the date and time of the acquisition, and 4×10^7 bytes of the 10^7 float numbers stands 10^7 channels of the spectrum.

2. The narrowband spectrum from the FCS which can be used to identify the resonant frequencies and quality factor (f_i, Q_i). The spectrum contains two arrays: an array provides the frequency channels and the other provides the power recorded by the spectrum analyzer on the equivalent channel.

The data processing prepares inputs for the signal scan, which are: the 10^7-channel spectrum from the AS ,and the resonant frequencies and quality factor (f_i, Q_i) of the four hidden photon sensitive modes of the acquisition where the broadband spectrum was acquired.

The extraction of (f_i, Q_i) from FCS's data has been mentioned in section 3.3.1 by fitting a Lorentzian function to the sweep spectrum exported from spectrum analyzer. With 2200 FCS executions in the first science run, there are a total of 2200×4 sweep spectra. After fitting the Lorentzian function to each spectrum and extracted f_i, Q_i of the resonances, one can follow the progression of f_i and Q_i during the tuning. Fig. 4.1 and Fig. 4.2 shows the variation of the f_i and Q_i during the tuning of plunger-I. In Fig. 4.1 one can observe the overshoot values from the smooth frequency curve of each mode. The ground mode TM_{010} is the most stable so one can see that the growth of the resonant frequency and quality factor are relatively steady. On the other hand, the other three higher modes have their field highly sensitive with the tuning, and at a particular plungers positions, their magnetic field turns out to be weaker or parallel with the probe's plane, the

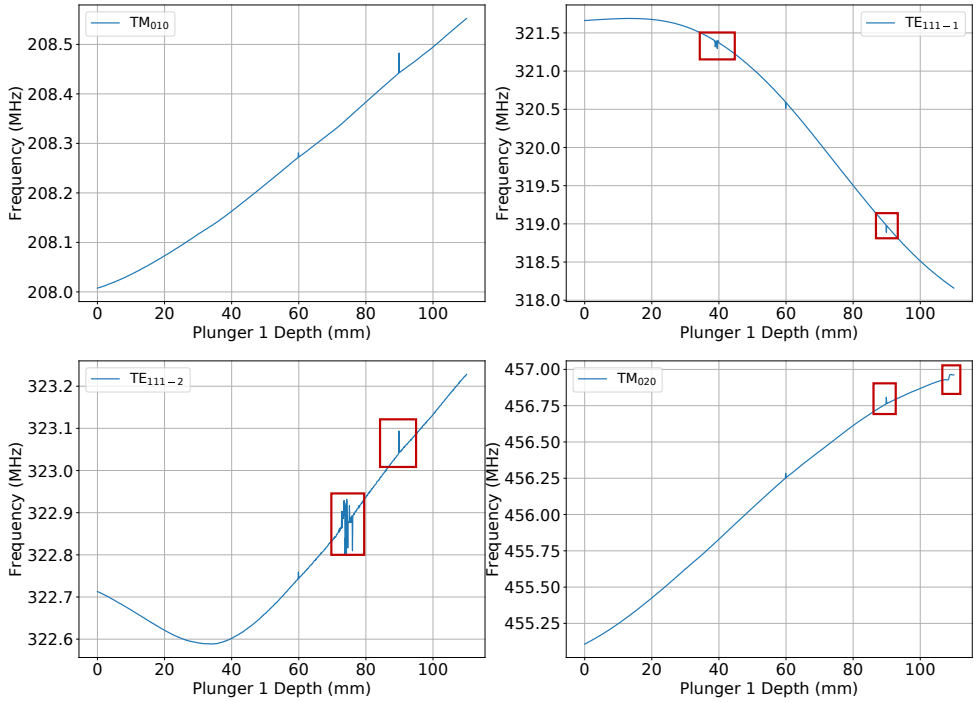

FIGURE 4.1: The evolution of resonant frequency (f_i) of TM_{010}, TE_{111-1}, TE_{111-2}, and TM_{020}. One can easily notice the overshot values during the evolution of the resonant frequeny, these values are also equivalent with the drop and high variation of quality factor in Fig. 4.2. These values are hightlighted for later treatment.

probe AN-0 could not pick up the magnetic fields related to these modes. As a consequence, the Lorentzian line could become more shallow and buried under the noise floor. The fit will not be efficient and return an incompatible (f_i, Q_i) in comparison with local values.

The treatment is blacklisting the resonant values at their equivalent plunger positions and neglecting them in the signal scan on the spectrum recorded by the AS, e.g., the mode TE_{111-2} is blacklisted at the plunger-I's positions of 72-75 mm. The spectrum recorded by the AS at this depth could be used to scan the signal at the other three resonant modes but TE_{111-2} is ignored.

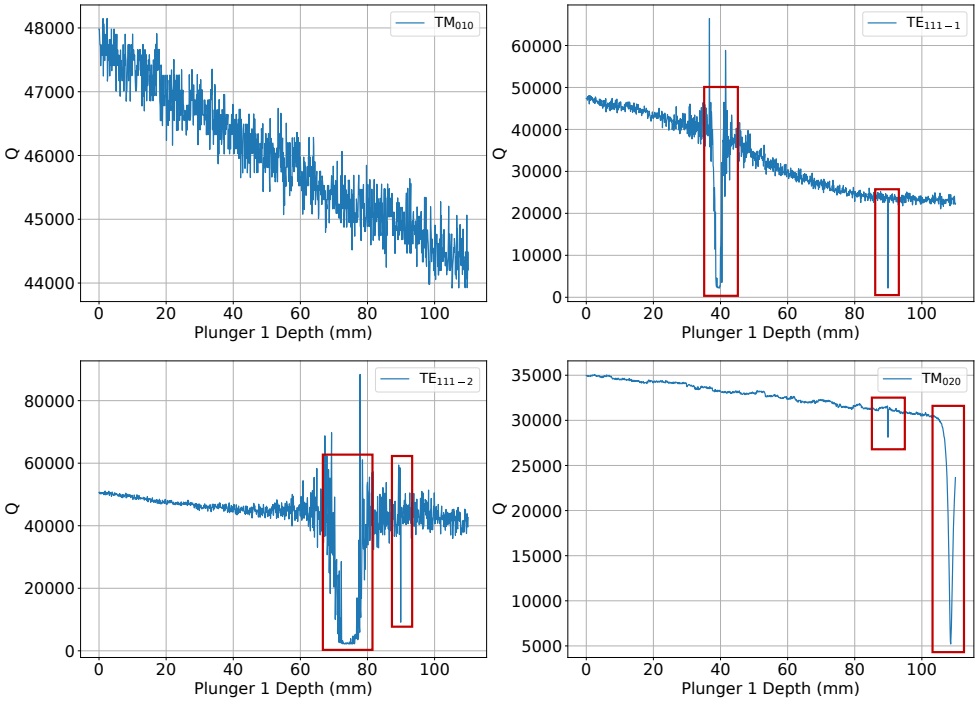

FIGURE 4.2: The evolution of the quality factor (Q_i) of TM_{010}, TE_{111-1}, TE_{111-2}, and TM_{020}.

Following the filtering of unrecognized resonant modes, the linear-interpolation is performed to obtain equivalent frequency and quality factor of the modes at the step-size of 10 microns. After this step, the information of the resonances in the spectrum at any position of the plungers could be retrieved.

4.3 Spectrum Characterization

Before starting the signal scan, it is useful to learn about some important details and issues of the spectrum from the acquisition. From now on, the term "single spectrum" stands for the 10 seconds worth of data from a single acquisition, while the "averaged spectrum" is obtained by averaging 22000 spectra from the first science run. Each type of spectrum carries diffrent which would be the object of each subsection.

4.3.1 Single Spectrum

Each single spectrum of the first science run of WISPDMX shows the same power level and distortion. Fig. 4.3 shows the spectrum of the first and the last acquisition (top and middle figure), and the stacked image of 50 spectra randomly picked from the 22000 spectra. Instead of the expected smooth thermal noise filled spectrum, there are several noise peaks distributed in the spectrum, and together the distortion from the 0-200 MHz is orginated from the amplifier which is most effective from the range 200-500 MHz. The noise peaks are suspected to originate from the electronic devices (amplifier, broken cable, radio switches) and the stray field penetrates the cavity (although the cavity is already heavily shielded) and the amplifier. Fortunately, most of the noise peaks appear off-resonance and cover multiple channels contrary with the possible shape of the signal (narrower or wider). These noise peaks disappear with an optimal setup of better shielding and transmitting cable.

The frequency ranges where the resonance resides are the most interesting regions, since they have the highest sensitivity to the hidden photon. The composite spectrum of the three regions are shown in the Fig. 4.4, Fig. 4.5, and Fig. 4.6 equivalent with the region of TM_{010}, TE_{111-1}, TE_{111-2}, and TM_{020} respectively. On the region of twin mode TE_{111} and TM_{010}, the noise is homogeneous and histogram of each channel show the smooth noise form following the Gaussian distribution as expected from thermal noise (Fig. 4.7 and Fig. 4.8). However, in the region of the ground mode TM_{010}, there is a mild level of stray field that leaked into the cavity (or electronic noise). Fig. 4.4 shows the heat map of the power spectra of 3000 acquisitions in the frequency band from 207 MHz to 209 MHz (a total of 40000 channels). The power level of the frequency band 207-208.5 MHz is mildly higher than the 208.5-209 MHz band, this is the stray field that leaked into the cavity. The stray field noise follows the Gaussian distribution and similar level of power to the thermal noise (208.5-209 MHz band) as shown in Fig. 4.9 at two frequency channels of 207.5 MHz and 208.9 MHz. Fig. 4.10 shows the histrograms of 40000 channels collected from 3000 spectrum. At a certain degree, one can treat the stray noise as the thermal noise during the signal scan.

The signal scan on the single spectrum is split into two scans: on- and off-resonance scan. The region where the on-resonance scan is active has been discussed, and they are relatively smooth and undisturbed by the electronic noise or stray field

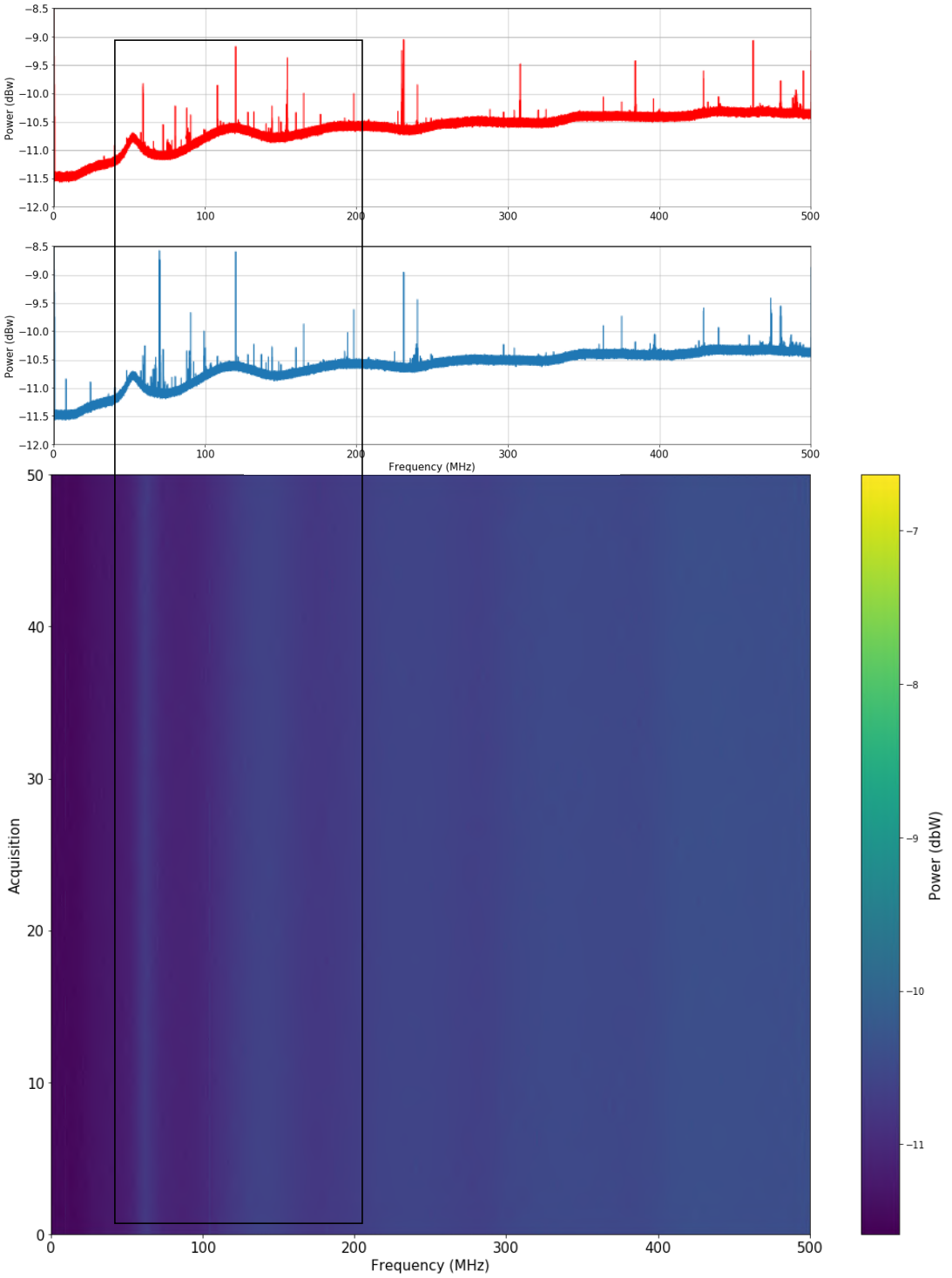

FIGURE 4.3: **Top**: the spectrum from the first acquisition, **Middle**: the single spectrum from the final acquisition, and **Bottom**: the stacked image of 50 single spectrum (randomly picked from 22000 spectra). The bottom image shows the wavy pattern identical with spectrum's shape of the top one. The black box highlights the frequency range where the spectrum has high distortion.

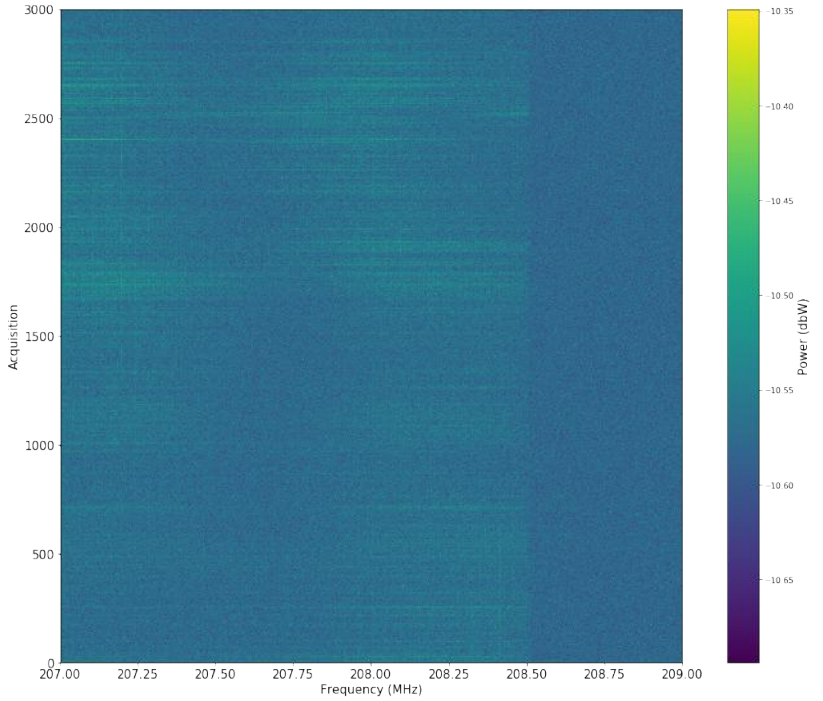

FIGURE 4.4: The composite power spectrum of 3000 acquisition in the frequency band 207-209 MHz. One can see that the frequency band of 207-208.5 MHz mildly higher power than the 208.5-209 MHz band, this is the stray field that leaked into the cavity. The stray field will become significant in the averaged spectrum from multiple acquisitions, which the averaging process reduces the thermal noise significantly.

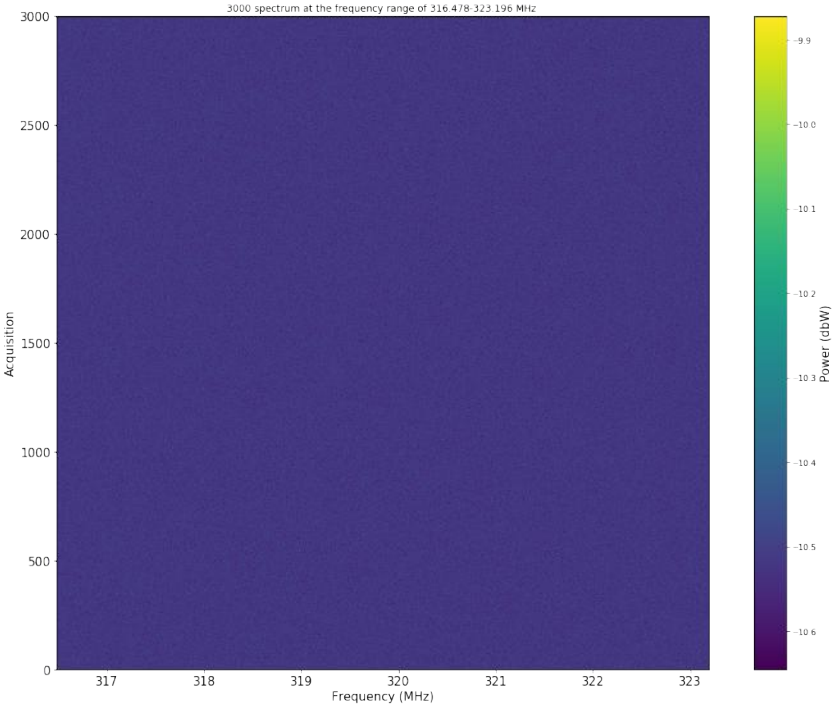

FIGURE 4.5: The composite power spectrum of 3000 acquisition in the frequency band 316.478-323.196 MHz equivalent with 134360 channels.

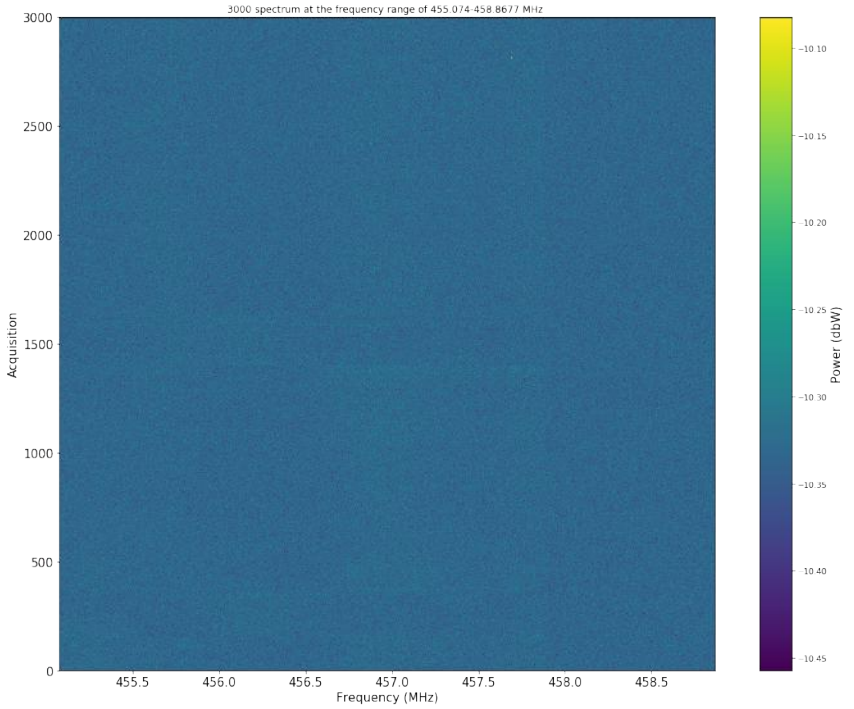

FIGURE 4.6: The composite power spectrum of 3000 acquisition in the frequency band 455.074-458.868 MHz equivalent with 75880 channels.

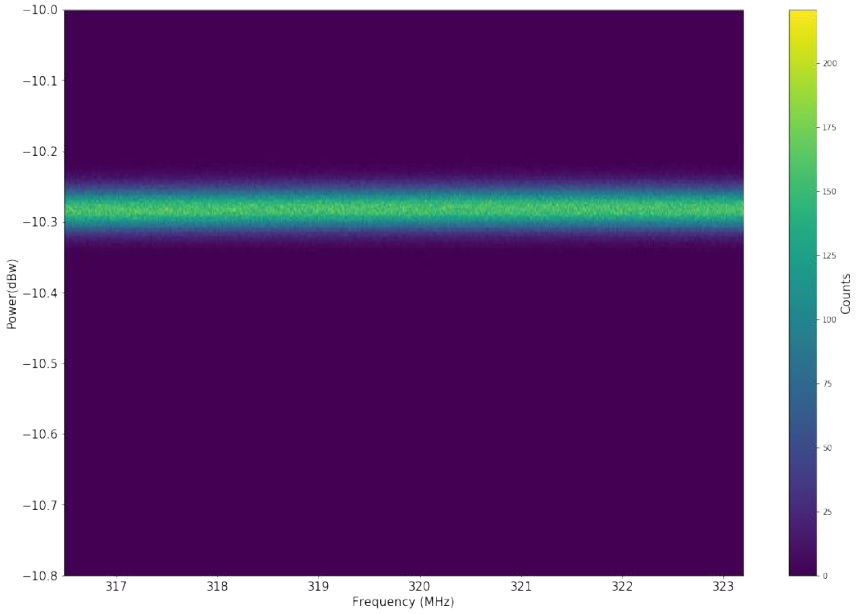

FIGURE 4.7: The heat map of 134360 channel histogram, collected in 3000 spectrum and in the range of 316.478-323.196 MHz.

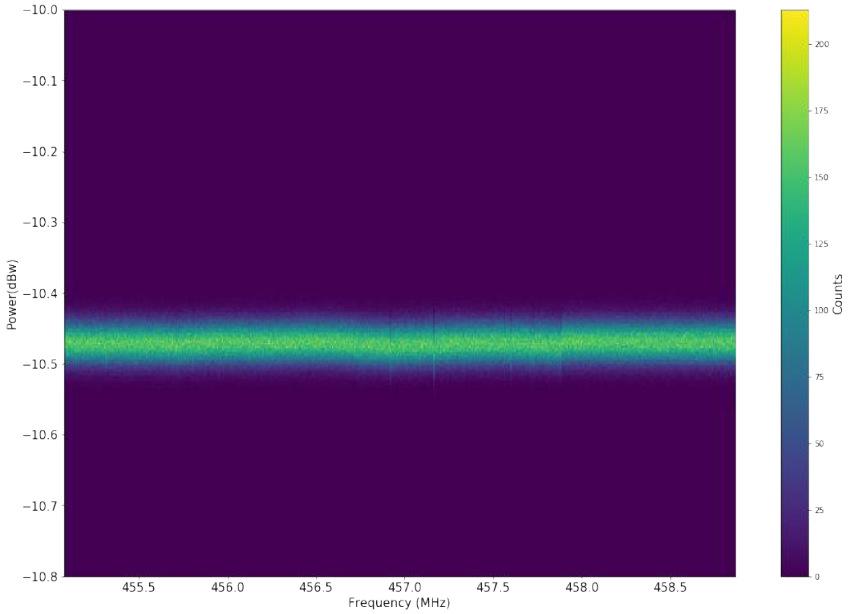

FIGURE 4.8: The heat map of 75880 channel histogram, collected in 3000 spectrum and in the range of 455.074-458.868 MHz.

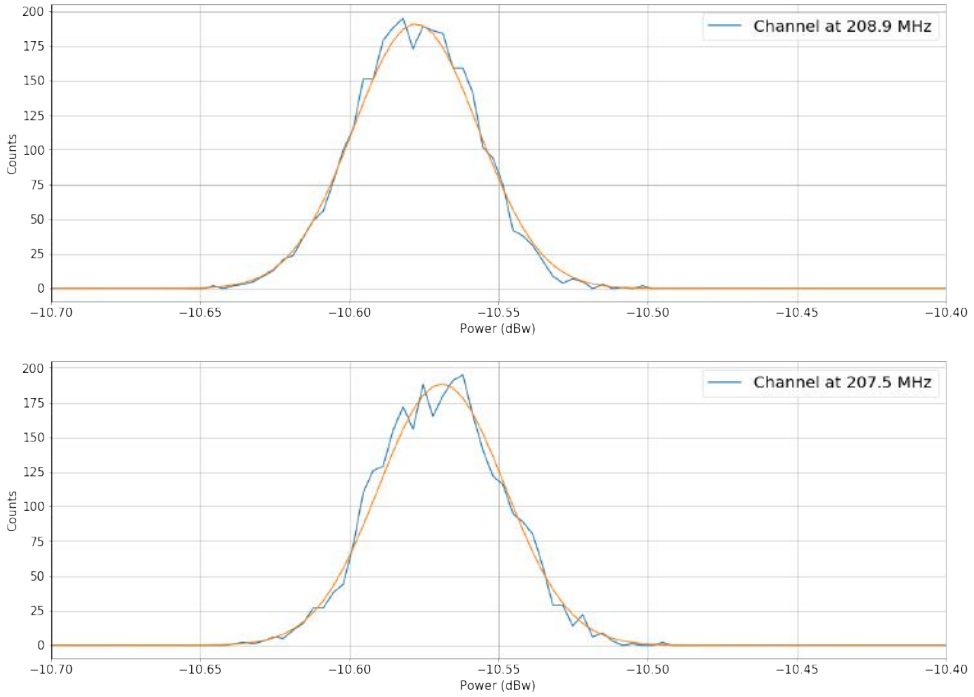

FIGURE 4.9: The distribution of thermal noise (channel at 208.9 MHz) and the stray field noise (channel at 207.5 MHz) with their equivalent Gaussian fit. Either noise types follow the Gaussian distribution. To some extent, one can treat the wideband Gaussian-like noise as the thermal noise during the scan for the signal.

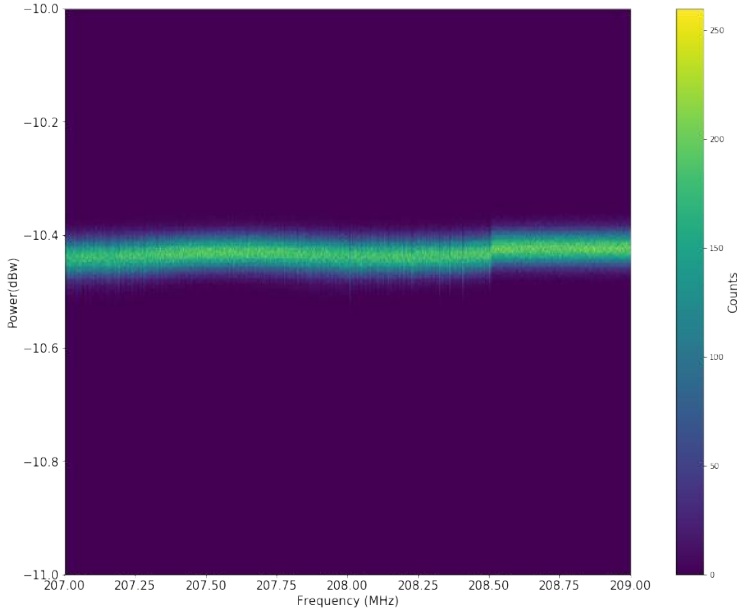

FIGURE 4.10: The heat map of 40000 channel histograms, collected in 3000 spectrum and in the range of 207-209 MHz. The stray noise band shows a mild different to the thermal noise band which follows the Gaussian distribution. Fig. 4.9 shows two slides at the channel of 207.5 MHz and 209 MHz.

with the ground mode is an exception. However, the stray noise field level at the ground mode is similar and shares a same properties with the thermal noise so one can apply the same scanning algorithm on the ground mode.
The off-resonance scan focus on the off-resonance region, which is broad, noisy and distorted. The distortion of the noise under 200 MHz can be simply solved by fitting a polynomial function and then flatten the spectrum. The noise, which is electronic noise and stray field noise, can be cataloged into two types:

1. Noise band: this noise spreads over a wide frequency band, and several high peaks distributed evenly along the band. Fig. 4.11a shows the typical noise band in the spectrum which covers a wide band of frequency and has significantly higher power than the local thermal noise. Fig. 4.11b shows another type of noise band which shows peaks with equal distance. This type of noise band usually has the base of dense noise similar to the one in 4.11a but buried under the thermal noise.

2. Noise peak: a single noise peak which can be mistaken for a signal. However, the width of the peak is broader or narrower than the allowed signal width of hidden photon particles in the region (mentioned in section 2.4). Fig. 4.11a shows a single noise peak which spreads over a high number of channel

width in the region where the signal shape should be narrow, e.g., the one in the figure spans 20 bins in the region only allows 2-channel signal width. In the contrary with broad noise peak, there is a type a single noise peak which spreads over a narrow channel width in the region where the signal shape should be wider. The one in the Fig. 4.11d spans five bins in the region allows 10-channel signal width. However, this narrow noise peak can become a signal candidate on the averaged spectrum, the thermal noise reducing from the averaging process could reveal the broader base of the noise and tackle more channel to become a signal candidate.

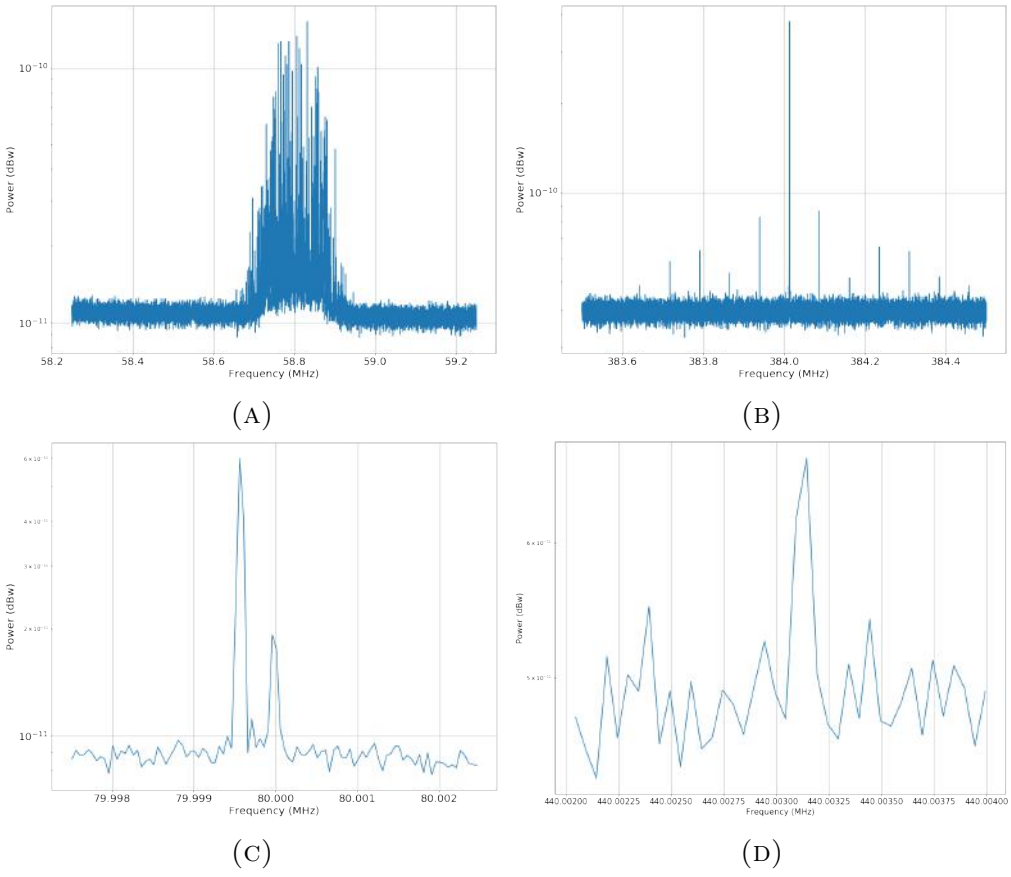

(A) (B)

(C) (D)

FIGURE 4.11: The two type of noise which can be found in the off-resonance region in the spectrum.

4.3.2 Averaged Spectrum

The averaged spectrum is generated from the 22000 single spectrum. The thermal noise floor is reduced with the factor of $\sqrt{22000}$ and reveals a tremendous amount of sub-structure buried under the single spectrum's noise floor. Fig. 4.12 shows

the averaged spectrum and the single spectrum over the full frequency range from 0 to 500 MHz, one can see that there is the surging of the in number of peaks and sub-structure distributed in the averaged spectrum.

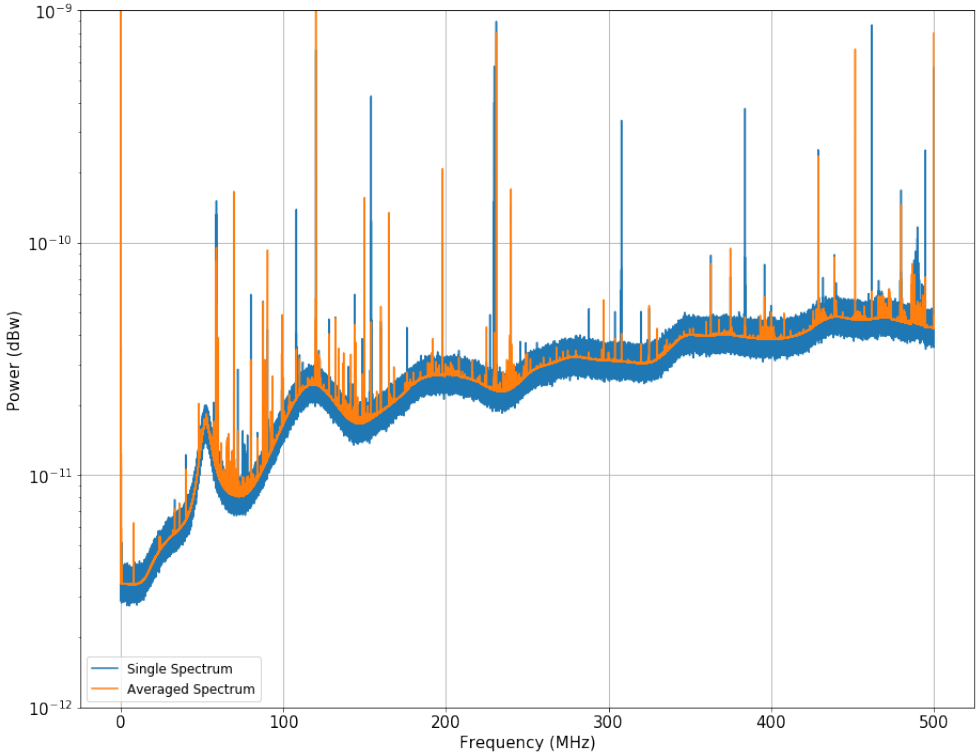

FIGURE 4.12: The single spectrum in comparison with the averaged spectrum.

In the averaged spectrum, the resonance regions suffer from the "new noise" where the new noise floor appears and contaminates these regions. In the ground mode, the stray field noise at 207-208.5 MHz becomes more visible than the single spectrum level (Fig. 4.13), similar to the TM_{020} where the noise contaminates 2/3 of the band shown in Fig. 4.14. Fortunately, the twin mode TE_{111} is is almost noise free and shows no sub noise structure (Fig. 4.15).

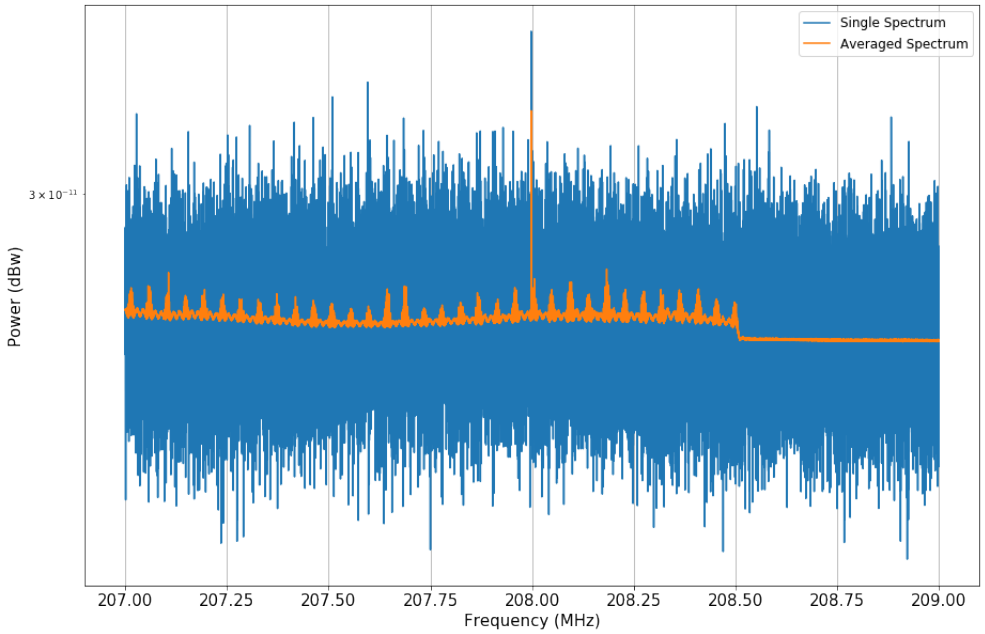

FIGURE 4.13: The region of the TM_{020}. The averaging process makes the stray field noise become more visible than in a single spectrum.

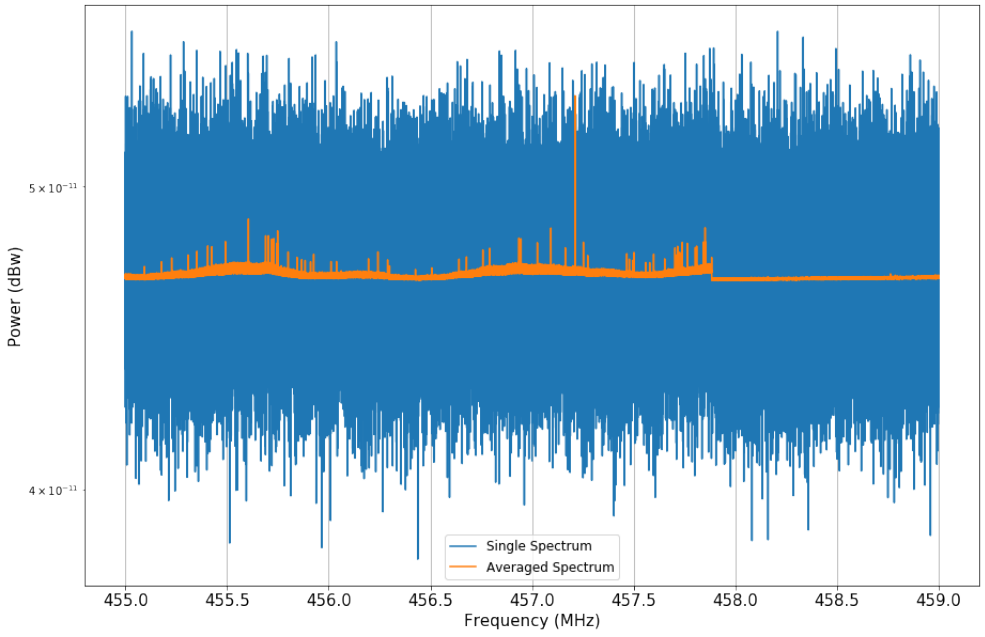

FIGURE 4.14: The region of the TM_{020}. A sub-noise-struture is revealed through the averaging process and contaminates 2/3 of the region.

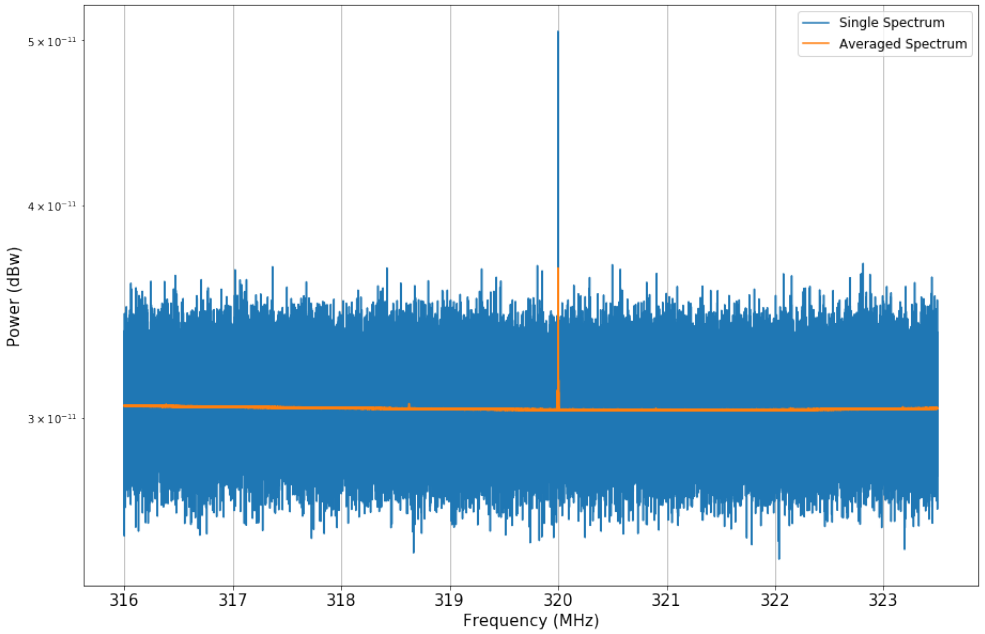

FIGURE 4.15: The single spectrum in compare with the averaged spectrum. This region is smooth and does not contain much of the stray and electronic noise.

4.4 Signal Scan

4.4.1 Signal Scan on a Single Acqusition Spectrum

The signal scan presented here is a single channel under the assumption that the the hidden photon signal is concentrated. In the case of a signal that spread on many channels in which the hidden photon at a higher mass range covers multiple channels. One strategy of multiple channel scan is selecting the consecutive channels with each of them has high significance level. The consecutive channels condition is a strong cut and effective in filtering out the stray or electronic noise.

4.4.1.1 Resonance Signal Scan

The resonant signal scan is limited in the tuning range of the four resonant modes (TM_{010}, TE_{111-1}, TE_{111-2}, and TM_{020}) with the information of the resonance given by the FCS. The scan of the signal follows primarily three steps:

1. Choosing a Region of Interest (ROI) which is centered at the position of the resonance and the width of 100 kHz ROI = $\{f_i - 50$ kHz, $f_i + 50$ kHz$\}$. The significance level is given by

$$S = \frac{P_{1 \text{ channel}} - \mu_{\text{ROI}}}{\sigma_{\text{ROI}}}, \tag{4.1}$$

   with μ_{ROI} and σ_{ROI} are the mean power and noise power of the ROI. If the power excess in a channel (within the ROI) provides a $S > 3$, the channel is recorded and become a level-I signal candidate.

2. If any of the level-I signal candidates is located in the area of central resonance which is much narrower than the ROI ($\{f_i - 10$kHz, $f_i + 10$kHz$\}$), the channel becomes a level-II candidate signal.

3. Tracking the position of the level-II candidate signal in multiple consecutive spectra: The channel's position of the candidate signal must reside in the same channel with the allowed range of 3 channels. E.g., a level 2 candidate signal is located in the channel 1000 of the first spectrum scan, if this candidate is found in the next three spectra within the bin 997 to 1003. This signal will become level-III signal candidate.

The level-III signal candidates are inspected manually by testing the expected variation of the amplitude during the tuning. In the haloscope experiment, the hidden photon signal is amplified by a Q factor at the resonant frequency. The tuning of the cavity shifts the resonances to another resonant frequency, in this scenario, the signal's amplitude decreases. Vice versa, a signal amplitude will increase if the resonance approaches its position. Hence, the level-III signal candidate must vary concerning the distance between itself and the resonant peaks. Fig. 4.16 shows the illustration of the evolution of the hidden photon signal by the relative position between the signal and the resonant frequency. The amplitude decreases when the resonance moves to a new frequency range which caused by the cavity tuning.

4.4.1.2 Off-Resonance Signal Scan

WISPDMX is the only haloscope experiment that is acquiring broadband spectra which cover not only the resonant range where the hidden photon signal is strongest

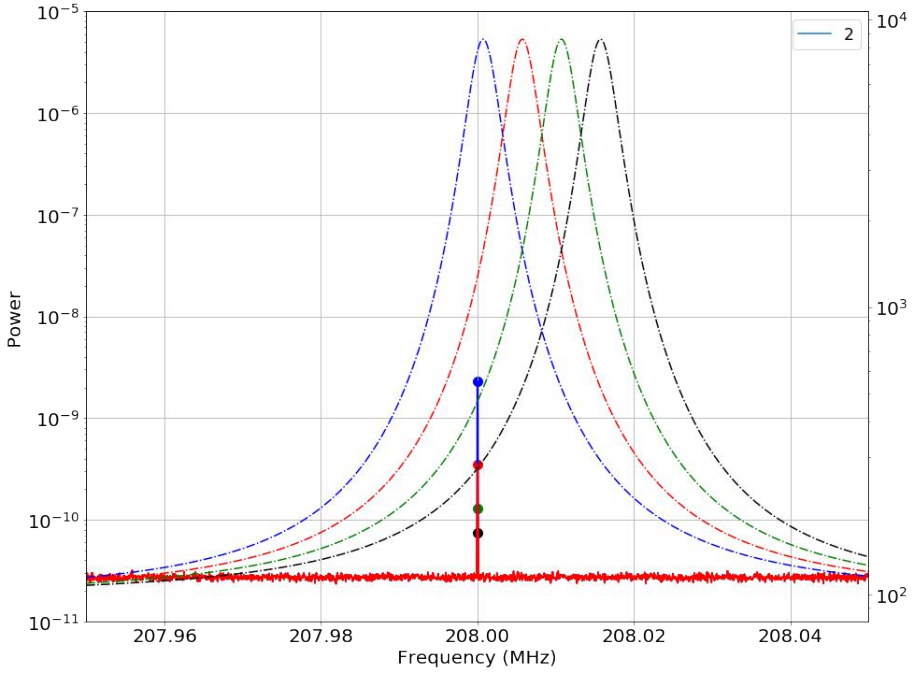

FIGURE 4.16: An illustration of the hidden photon signal's amplitude inside the resonant region. The point indicates the amplitude of the signal and different color represents the different state where the position of the resonant frequency. One can see that with the hidden photon amplitude is highest if they are in the center of the resonance and decrease if the resonant shifting to another position by the cavity tuning.

but also could be used to constrain the off-resonance hidden photon sensitivity. The off-resonant range covers a much larger band than the resonance scan, with a total range of 488.4 MHz. One important feature of the off-resonance signal is: the hidden photon signal must attain the same amplitude for every spectrum even with the shifting of resonance during cavity tuning, which is contrary to the behavior of the signal in resonance.

The full spectrum is separated into smaller bands with a width of 1 MHz. Due to the decrease of the amplification profile of the amplifier chain under 200 MHz, the power spectrum below 200 MHz has a steep background. Hence, before the signal search one must flatten the band by fitting a first-order polynomial function to the spectrum, the fitting function corresponds to the average power spectrum of each channel which follows a steep background. Fig. 4.17 shows a spectrum where the noise power is over the flatten background. The signal scan algorithm is defines as follows:

1. From a single acquisition spectrum. The signal candidate is the channel with $S > 2$. The position of the signal candidate is recorded into a candidate

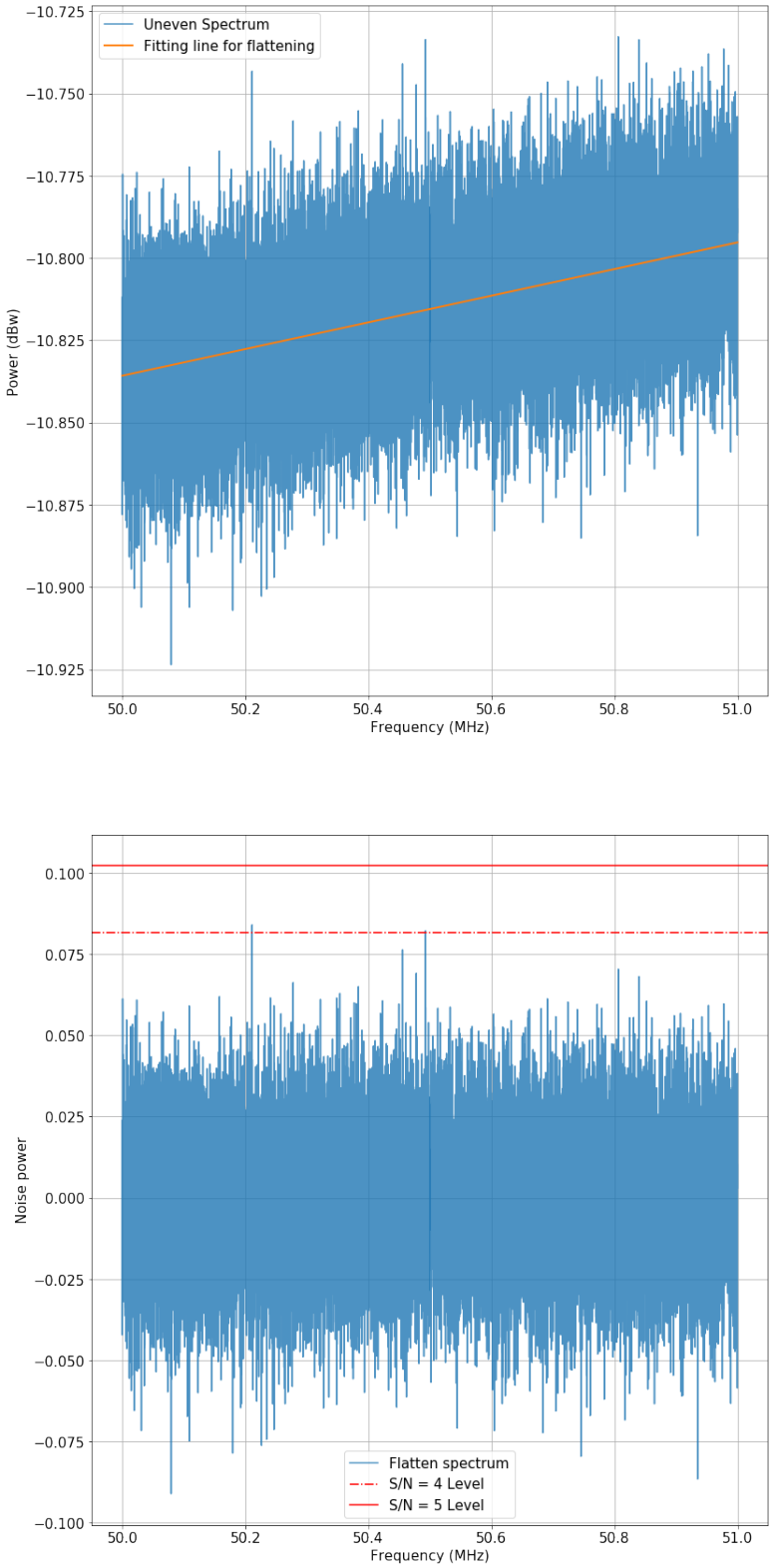

FIGURE 4.17: The flatting process to treat an uneven spectrum band. The band's width is chosen to have the flattening line is the first order polynomial function.

counting table which given a value "1" if in that channel $S > 2$ or "0" is $S < 2$.

2. Repeat the previous step with 22000 spectra. However, after each spectrum scan, the candidate counting table is accumulated into the stacked counting table. The stacked counting table records the channels with $S > 2$. At the significance of two sigmas, the false alarm rate is 1 of 20. Hence a thermal noise channel should produce at least 1100 counts in 22000 spectra. If the number of counts in a channel is higher than 1100, one can assure that the source that causes the surging has the distribution with the mean greater than the thermal noise which could be signal or stray and electronic noise.

One can expect that after the two previous steps, the number of single channel candidates would be numerous. It is better to apply the multi channel search on these single channel candidates. One can restrict the condition for the signal to satisfy the linewidth's requirement expected from equivalent frequency range, e.g., from the range of 0-59.059 MHz, the hidden photon line width is limited in one channel. If two or more consecutive channels have high significance, these channels are rejected. A similar method applies for the range of 467.967-500 MHz, where the line width spans over 12 channels, one can reject the candidate if its span is less or more than 12 channels. A conditional function for the signal could be fomulat as follow

$$n_{\text{candidate}} = \begin{cases} \neq n_{\text{HP}}(f) & \rightarrow \text{reject} \\ = n_{\text{HP}}(f) & \rightarrow \text{accepted as a strong signal candidate} \end{cases}, \tag{4.2}$$

with $n_{\text{candidate}}$ is the width of the candidates, $n_{\text{HP}}(f)$ is the linewidth of the hidden photon signal equivalent with the frequency range (given in Table 2.1).

4.4.2 The Scan on the Averaged Spectrum

For the reason that the averaged spectrum has the thermal noise reduced with the factor of $\sqrt{22000}$ and contains complex sub-structure which has been exhibited in section 4.3.2. The algorithm used in the single spectrum scan becomes impractical because the averaged spectrum is unique and does not permit cross spectrum comparison. The single channel scan would return a large number of single channels which has the significance level larger than 5 ($S > 5$). It is better to use the

single channel scan on the resonant regions where the noise floor is much milder and smoother than the off-resonant region. The multiple channel scan would be more practical to search for the signal candidate with the tight condition of the line width. The signal scan is given as follows:

1. Single channel search: similar to the off-resonance scan. The list of single channel candidates is retrieved after spectrum flattening and application of the significance level threshold on each channel. With the list of candidates, one could constrain the on-resonance regions if the candiate is located in the stray or electronic noise area or the candidate belongs to the wide noise peak.

2. The multiple channel search is similar to the one mentioned in section 4.4.1.2 with the condition given by the equation 4.2.

In conclusion, the signal scan on the averaged spectrum shares many mutual features from the on- and off-resonance scan algorithm at single spectrum level. However, the scan on the level of the averaged spectrum would return a large set of candidates because there are no other spectra to compare. Lastly, throughout the presentation on the signal scan's algorithm, one can see that the signal linewidth conditions is a strong cut to filter out the bad candidates.

Chapter 5

Result from the First Science Run

Abstract

This chapter will present the result from the signal scan of the first science run. The first section will show the detectable power of the WISPDMX in the first science run. The second section will show the result of the signal scan, and the final section will present the exclusion limit generation from the result of the first science run.

5.1 Detectable Power, Noise Power

The signal from the antenna before arriving to the central digitizer is amplified by the amplifier chain with the amplification factor of $\sim$ 80 dB. The power output $P_{\text{output}}(f)$ of the cavity picked up by the antenna can be retrieved by the following equation:

$$P_{\text{output}}(f) = P(f) \times 10^{-g(f)/10}, \tag{5.1}$$

where $g(f)$ is the amplification factor of the amplifier chain as a function of frequency (Fig. 5.1), $P(f)$ is the power in the bandwidth of 50 Hz. With the given amplification factor, one can calculate the lowest power detectable of WISPDMX at two level: single spectrum and averaged spectrum. With the current WISPDMX's setup for the first science run, even without cooling, the detectable

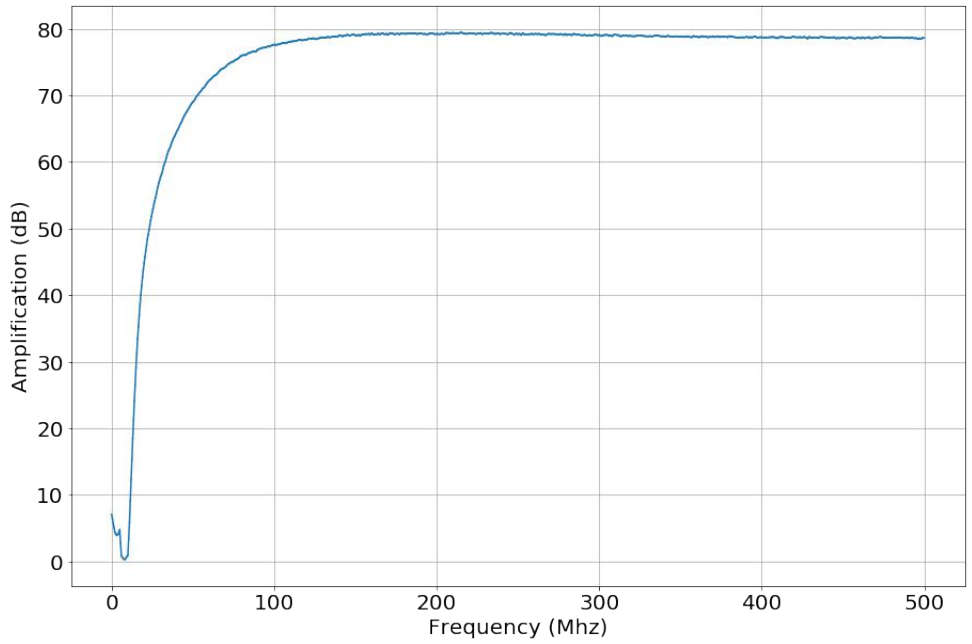

FIGURE 5.1: Amplification factor of the amplifier chain.

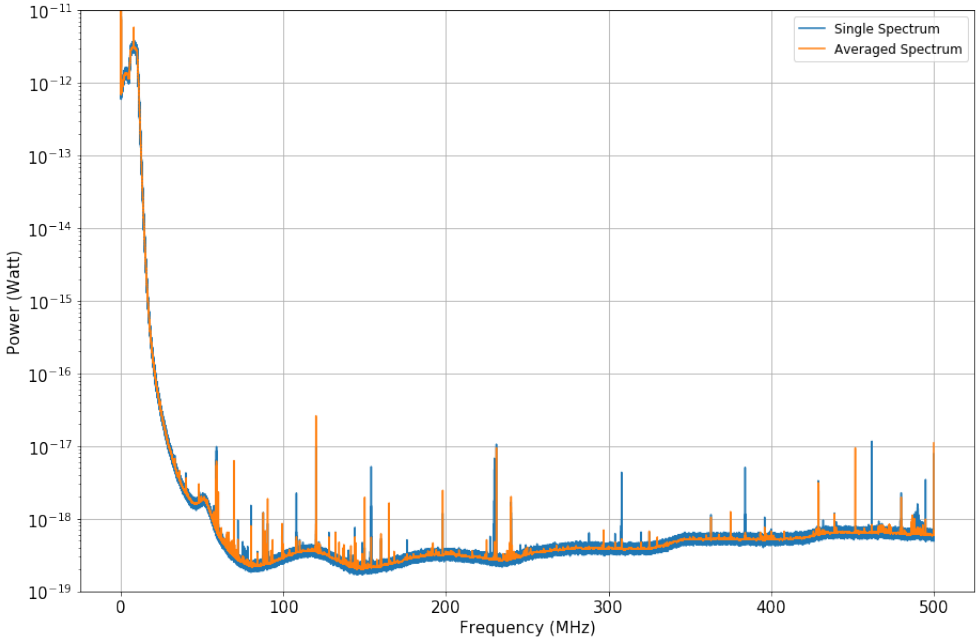

FIGURE 5.2: The lowest detectable power of WISPDMX with the setup of the first science run.

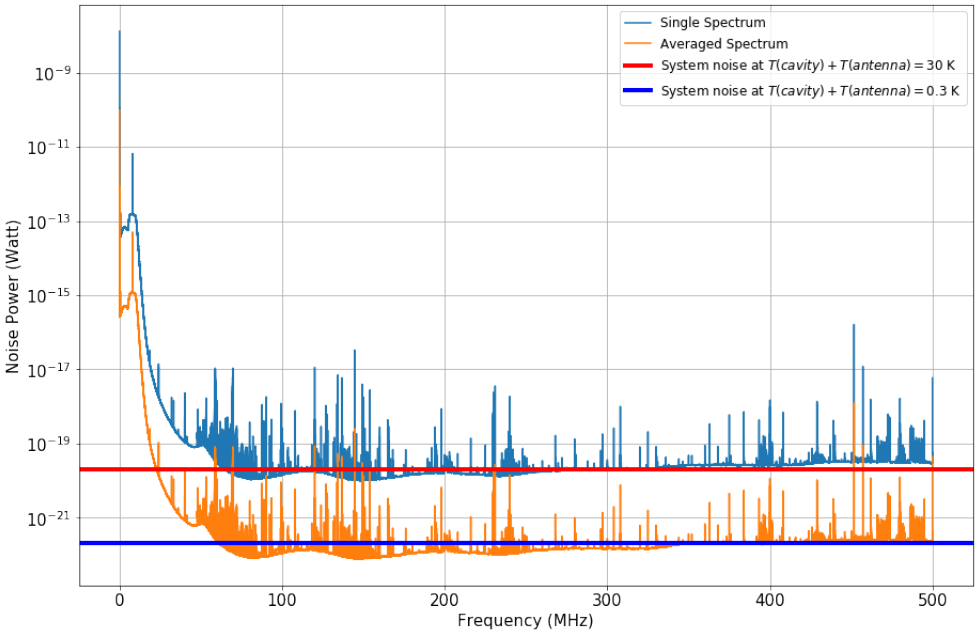

FIGURE 5.3: The noise power of the single spectrum and averaged spectrum in the bandwidth of 50 Hz.

power is $10^{-19} - 10^{-18}$ Watt. The noise power σ_{single} of the single spectrum is calculated by averaging the noise spectrum of each single spectrum from dataset, while the noise power of the averaged spectrum σ_{averaged} is calculated from the σ_{single} by:

$$\sigma_{\text{averaged}} = \frac{\sigma_{\text{single}}}{\sqrt{22000}}. \tag{5.2}$$

The noise power at the level of the single spectrum and averaged spectrum are $\sim 8 \times 10^{-19}$ Watt and $\sim 5 \times 10^{-22}$ Watt. Fig. 5.2 and Fig. 5.3 show the lowest detectable power level and the noise power level of the single spectrum and averaged spectrum. One can see that at the level of single spectrum the effective system temperature is ~ 30 Kelvin while the averaged spectrum has the effective temperature of ~ 0.3 Kelvin.

5.2 Result from Single Spectrum Scan

On the single channel scan at the resonances of four hidden photon sensitive modes (TM_{010}, TE_{111-1}, TE_{111-2}, and TM_{020}) with the equivalent mass range are: 0.8602-0.86461 μeV, 1.3088-1.3358 μeV, 1.8820-1.8977 μeV. The number of level-I signal

candidates with significance level larger than 3 ($S > 3$) is approximately 5 to 8 candidates in the ROI of 100 kHz. At the level-II test, all of these candidates are located outside the region of the resonance (20 kHz).

However, the level-III test is extended to the level-I candidates. To pass the level-III test, in a consecutive spectra and at the region of 6 channels around the frequency of the candidates, there must be a channel which has high significance. The result is negative for all of the candidates, in the consecutive spectrums, these candidates show the significance level lower than three $S < 3$ in the expected region.

On the multiple channel scan for hidden photon signal with linewidth, the 5-channel scan is apply for the TM_{010}, 8-channel on the twin modes TE_{111}, and 11-channel on the TM_{020}. On every single scan, there are no consecutive channels which have a significance level larger than two. In conclusion, there is no detection in the region of the resonance above the level of $2\sigma_{\text{single}}$.

In the off-resonance search, the counting table exported from the scan of 22000 spectra gives a total of 72724 single channels which give the count larger than 1100 (including the resonant region). The signal width condition is applied to detect the consecutive channels and reduces the total candidates down to 1439 which cover 3523 channels. Table 5.1 shows the number of candidates in their respective frequency range.

TABLE 5.1: The candidates from the off-resonance search at single spectrum level with the condition of signal linewidth.

No. of Chs	**Range (MHz)**	**No. of Candidate**	**No. of Channels**	**Range (MHz)**	**No. of Candidate**
1	0 - 59.059	444	7	263.763 - 304.804	0
2	59.059 - 100.600	652	8	304.804 - 345.345	4
3	100.600 - 141.641	68	9	345.345 - 386.386	1
4	141.641-182.182	62	10	386.386 - 426.926	3
5	182.182 - 223.223	156	11	426.926 - 467.967	14
6	223.223 - 263.763	17	12	467.967-500	18

These are the final candidates of the off-resonance scan, but it is impossible to distinguish these candidates from the noise or signal. These candidates are recorded to compare to the result of the next science run, if any of these candidates are still resident in the same frequency they would be a strong candidate for hidden photon signal.

5.3 Result from Averaged Spectrum Scan.

During the signal scan on the averaged spectrum, there a total of 21295 single channel candidates with significance level larger than $5\sigma_{\text{averaged}}$. The signal width condition is applied again to detect the consecutive channels, the condition reduces the total channels down to 634 candidates and cover 1573 channels. Table 5.2 shows the number of candidates in their respective frequency range.

TABLE 5.2: The candidates from the signal search at averaged spectrum level with the condition of signal linewidth.

No. of Channels	Range (MHz)	No. of Candidate	No. of Channels	Range (MHz)	No. of Candidate
1	0 - 59.059	275	7	263.763 - 304.804	9
2	59.059 - 100.600	159	8	304.804 - 345.345	1
3	100.600 - 141.641	83	9	345.345 - 386.386	14
4	141.641-182.182	32	10	386.386 - 426.926	5
5	182.182 - 223.223	21	11	426.926 - 467.967	1
6	223.223 - 263.763	28	12	467.967-500	6

Once again, the result previously presented shares the same situation with the result from the off-resonance scan at the single spectrum level. These candidates are recorded and compared with the candidates of the next science run.

5.4 Exclusion Limit from the First Science Run

While the result in the signal scan at two levels of the single spectrum and averaged spectrum show a large number of signal candidates, it would not be compelling to conclude these candidates were signal or not. The second science run is necessary and provides good opportunities to have a longer record track for these candidates. In another word, if these candidates prevail in the result of the second run, there would be firmly conclusion on the characteristic of the candidate: signal or noise. In the end, the result from the signal scan by analysing the data set of the first science run does not yield any hidden photon signal but many prominent candidates. These are conclusions on the result of the scan:

1. At the level of the single spectrum, the resonance region and off-resonance region show no track of hidden photon signals at the level above $2\sigma_{\text{single}}$.

2. At the level of averaged spectrum, the averaged spectrum also shows no track of hidden photon signal at the level above $5\sigma_{\text{averaged}}$.

5.4.1 Limit Generation

From equation 2.27, one could retrieve the exclusion limit for the mixing constant between the hidden photon and photon. One could divide two sides of the equation to the noise power σ

$$S = \frac{P_{\text{output}}}{\sigma} = \frac{1}{\sigma} 1.632 \times 10^{-16} \left(\frac{\chi}{10^{-12}}\right)^2 \frac{\kappa}{0.1} \frac{Q}{50000} \frac{V}{447 \text{ liter}} \frac{\mathcal{G}_{\gamma'}}{0.3} \frac{m_{\gamma'}}{\mu eV} \frac{\rho_0}{\text{GeV/cm}^3}. \tag{5.3}$$

The first term ($\frac{P_{\text{output}}}{\sigma}$) is the significance level S of not detecting any hidden photon signal, given in the section 5.2. The exclusion limit of χ at the significance level S can be retrieved from the equation 5.3

$$\chi = 7.8 \times 10^{-12} \sqrt{\text{S}\sigma} \left(\frac{\kappa(m_{\gamma'})}{0.1} \frac{(Q \cdot \mathcal{G})(m_{\gamma'})}{50000 \cdot 0.3} \frac{V}{447 \text{ liter}} \frac{m_{\gamma'}}{\mu eV} \frac{\rho_0(m_{\gamma'})}{\text{GeV/cm}^3} \right)^{-1/2}. \tag{5.4}$$

In this equation, $(Q \cdot \mathcal{G})(m_{\gamma'})$ and $\rho_0(m_{\gamma'})$ are functions of frequency or the mass of the hidden photon explained in section 2.5. The κ is extracted by measuring the reflection parameter of AN-0 given in section 3.3.3. The exclusion limit of the single spectrum and averaged spectrum at their equivalent significance level of $2\sigma_{\text{single}}$ and $5\sigma_{\text{averaged}}$ is given in the Fig. 5.4. The exclusion limit in the resonant region is given in Fig. 5.5.

The exclusion limit at the region of the resonance is barely greater than the single spectrum because the averaged gain ($\frac{\sum_j \sum_i (Q_{i,j} \mathcal{G}_{i,j})}{N}$) is worse than the gain from a single spectrum. The tuning of the resonance causes a frequency offset, which significantly modifies the Lorentzian profile which is the main reason that the averaged gain is lower than the single spectrum's gain. However, the averaged gain at the off-resonance region is close to the gain of a single spectrum because the tuning does not alter the Lorentzian curve here. Fig. 5.6 shows an example on the averaged gain calculated from two single acquisition gains at two different positions of the plungers.

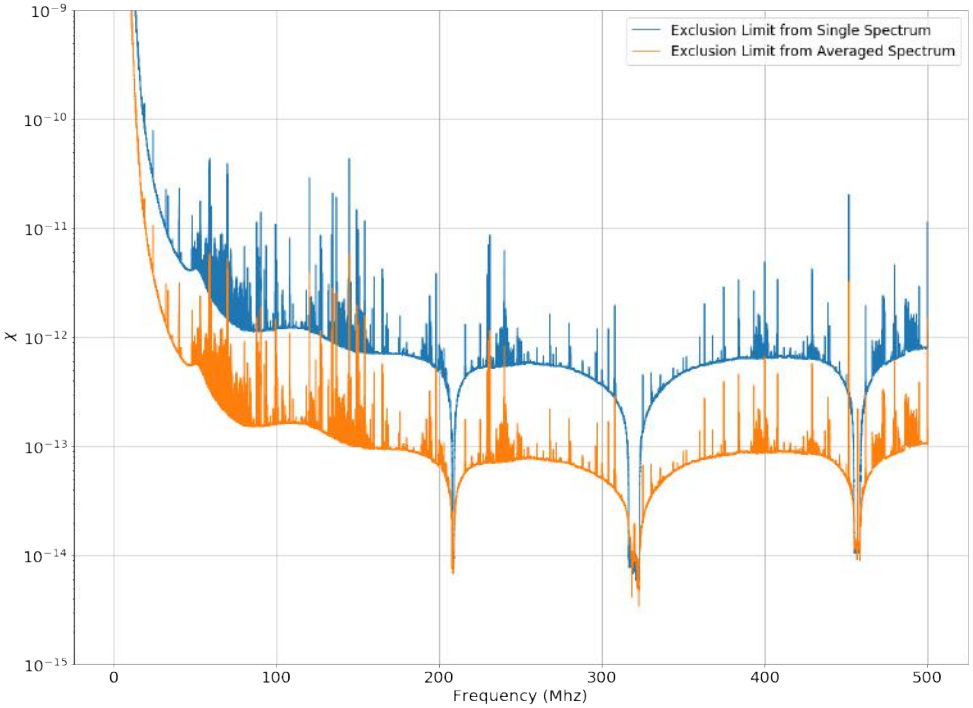

FIGURE 5.4: The exclusion limit of the mixing constant χ as a function of frequency for two spectrum levels: single spectrum and averaged spectrum. The exclusion limit for the single spectrum is generated at the significance level of $2\sigma_{\text{single}}$ while the averaged spectrum is generated at $5\sigma_{\text{averaged}}$.

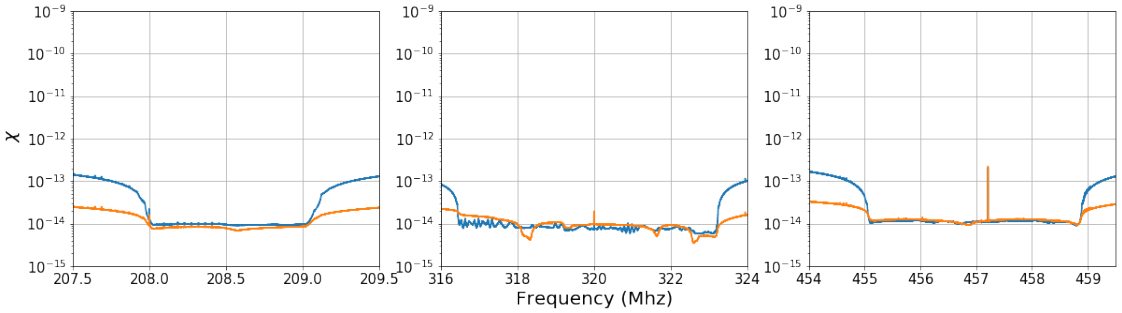

FIGURE 5.5: The exclusion limit of the mixing constant χ at the resonant region.

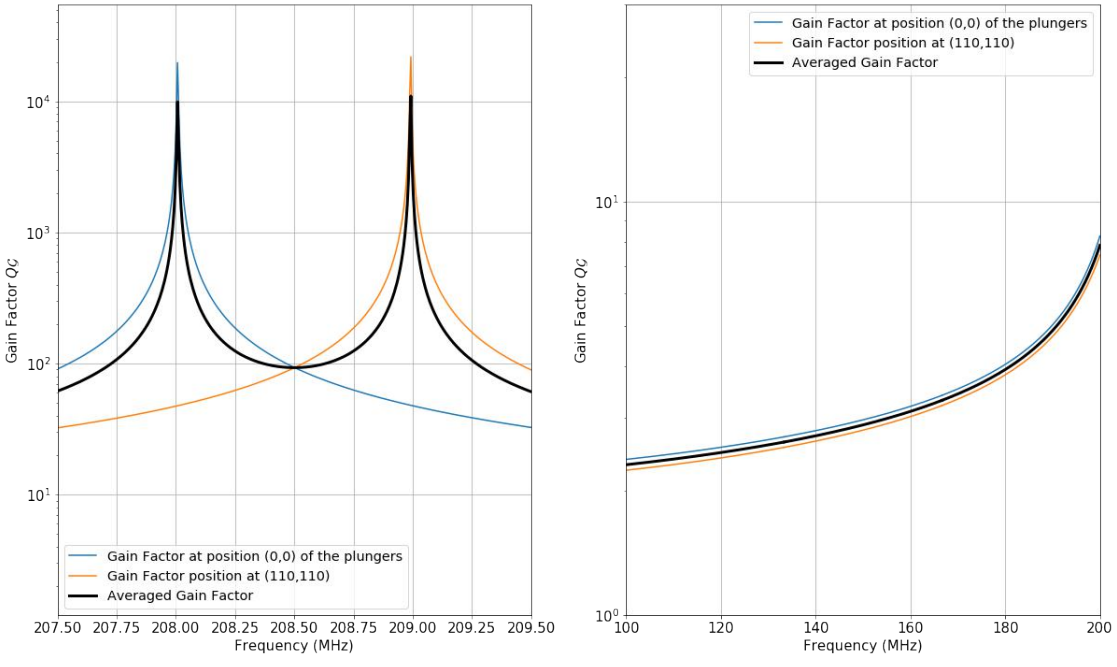

In conclusion, the scan at the level of the averaged spectrum increases the sensitivity at the off-resonance region and set stronger exclusion limit at the off resonance region but the exclusion limit at the resonant region is almost unchanged[1].

[1] it is important to remember that the exclusion limit of the single spectrum is set at 5σ

Chapter 6

Conclusion and Future Development

6.1 Conclusion

The primary objective of the WISPDMX is the search for hidden photons which are a theoretical candidate for dark matter. During the last three years, from a simple setup and an inefficient acquisition system, WISPDMX has been put under intense developments and significant upgrades, resulting in the three optimized systems: the Frequency Calibration System, the Mechanical System, and the Acquisition System. The three systems have been brought together to form the final form of the WISPDMX as the most sensitive experiment in performing searches for the hidden photon particle in the mass range of 10^{-7} to 10^{-6} eV. In chapter 2, the theoretical foundation of the experiment is presented, from the axion haloscope type experiment to its application as a hidden photon haloscope using the resonant cavity which WISPDMX is the first experiment implementing such a system. The power developed of the hidden photon haloscope experiment has also been shown and accompanied by the studies on the broadband gain and hidden photon linewidth. These studies are essential to the WISPDMX as a haloscope experiment but acquires broadband data at the frequency nearly 0 Hz to 500 MHz, it means that the WISPDMX be able to search for the hidden photon mass and exotic light particle with the mass below 2 μeV. The analysing and signal scan technique on the dataset of the first science run have been presented in chapter 5. The scan on the data set of the first science run shows no signal on both the

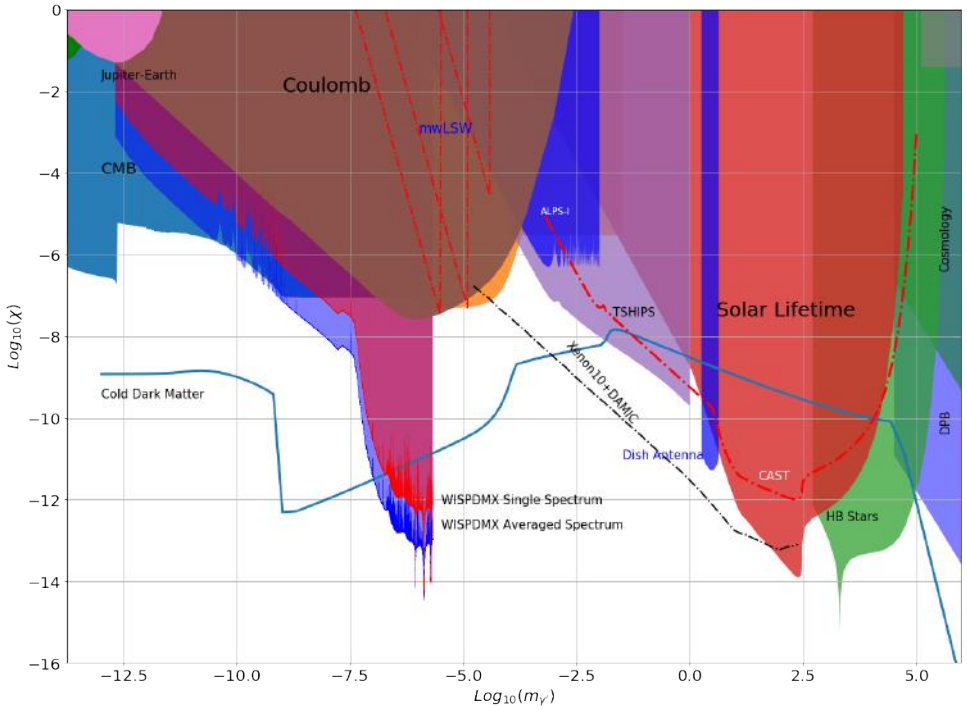

FIGURE 6.1: The exclusion limit of the mixing constant χ to the mass of hidden photon. The exclusion is draw from the result of WISPDMX's first science run. One can see that WISPDMX is the first experiment which could put some constraints on the χ below the line drawn by the Cold Dark Matter.

single spectrum and averaged spectrum level at 2σ and 5σ respectively. The limit for the mixing constant of hidden photon and photon with respect to the mass of the hidden photon is shown in Fig. 6.1 and Fig. 6.2 together with exclusion limit from other studies.

The result from the first science run search also contains many signal candidates which, at the stage and information from the first science run, could not be distinguished from the stray/electronic noise or a signal. The information and details of these candidates are stored and put under the scope for the next science run to have a better conclusion on the nature of the candidates.

6.2 Future Development

With the current setup of WISPDMX, the experiment suffers strongly from the electronic noise and stray field noise. In order to reduce this noise, it is ideal to have the cavity and devices shielded from the ambient environment. A new

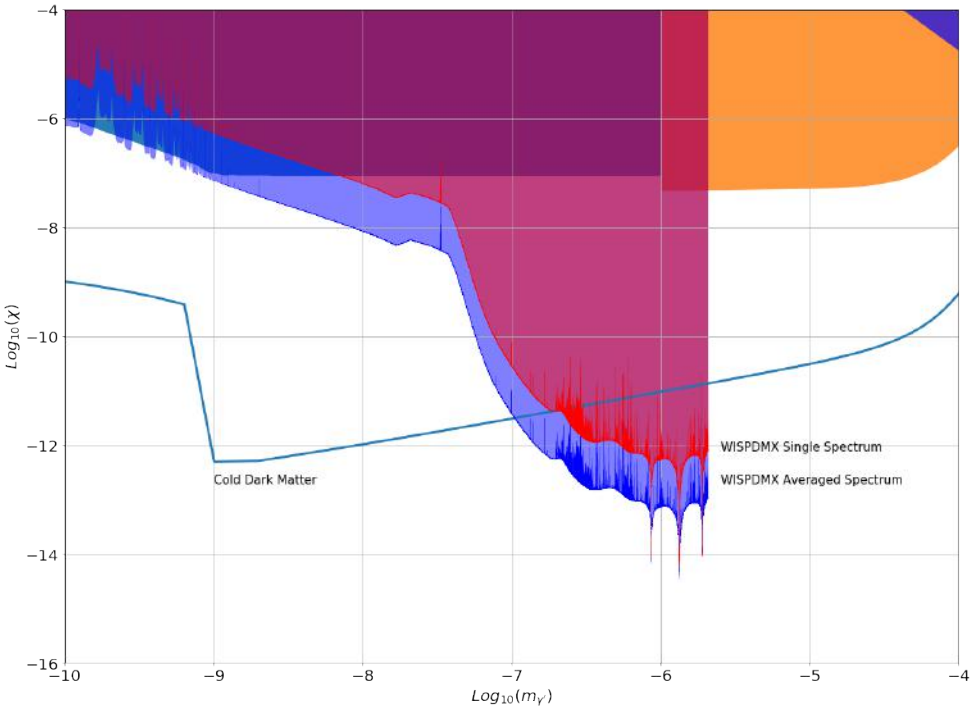

FIGURE 6.2: The exclusion limit of the mixing constant χ to the mass of hidden photon at smaller scale from Fig. 6.1.

science run from with the shielded apparatus would return a smooth spectra and reduce the external noise. There is a huge space for development for WISPDMX, and WISPDMX itself also plays a role as a testbench for multiple developments for future experiments, e.g. the unique central acquisition system of WISPDMX which could be apply for different experiment which require a high resolution broadband spectra. At the moment of writing this thesis, there are several ongoing developments are being executed:

1. New antenna: The AN-3 antenna is the foundation of the new antenna development stage with the higher coupling with the cavity and less internal noise like the AN-0.

2. High-resolution Central Digitizer: one can have the central acquisition system to get into very high resolution, in theory, as low as 0.1 Hz, with could be done by extending the 20 MS buffer into 10 GS buffer, with FFT is accelerated by the GPU as mentioned in section 3.4.4.

3. Acquisition System 2: with the lock-in amplifier with an inverse dynamic range of 120 dB, the alternative acquisition could probe into even lower energy than 10^{-18} Watt of the current setup.

Certainly, there are plans for the next science run which would define WISPDMX itself as one of the most sensitive direct experiment searches for the hidden photon in the sub-eV mass range. If there are hidden photons as light cold dark matter particles, there is a possibility that WISPDMX may find it.

Appendix A

Measurement of Noise Figure

A.1 Noise Figure and Noise Factor

Noise Figure (NF) and Noise Factor (F) are measures of degradation of the signal-to-noise ratio of the input (SNR_i) to the output's SNR (SNR_o), caused by components in a radio-frequency (RF) signal chain. The noise figure is the difference in decibels (dB) between the noise output of the receiver to the noise output of an ideal receiver with the same overall gain and bandwidth when the receivers are connected to matched sources at the standard noise temperature T_0 (290 K at room temperature). The noise power density from a simple load is equal to kT, where k is Boltzmann's constant, T is the absolute temperature of the load. The noise factor is described as:

$$F = \frac{\mathrm{SNR}_i}{\mathrm{SNR}_o}. \tag{A.1}$$

The NF is defined as the noise factor in dB unit

$$\mathrm{NF} = 10 \cdot \log(F) = 10 \cdot \log(\frac{\mathrm{SNR}_i}{\mathrm{SNR}_o}) \tag{A.2}$$

the signal to noise ratio of input and output is given by

$$\mathrm{SNR}_i = \frac{S_i}{N_i} \tag{A.3}$$

$$\mathrm{SNR}_o = \frac{S_o}{N_o} = \frac{GS_i}{GN_i + N_x} \tag{A.4}$$

the input energy density, $S_i + N_i$, is amplified by a power gain of G and adds a certain amount of internal noise from the device N_x to the input, $G(S_i + N_i) + N_x$. The noise factor can be reduced into

$$F = \frac{GN_i + N_x}{GN_i} = \frac{G \cdot kTB + N_x}{G \cdot kTB} = \frac{N_x}{GkTB} + 1. \tag{A.5}$$

In the previous equation, B is the frequency bandwidth, the reference input noise is the thermal noise at the room temperature (290 Kelvin) with the power density of -174 dBm.

A.1.1 Noise Factor of a Cascade of Amplifier Chain

A simple amplifier chain is a combination of at least two amplifiers with gain G_1, G_2, noise factor F_1, F_2, and injected device noise N_{x1}, N_{x2}. With the input energy density of S_i and N_i, the output energy density after the first amplification stage is

$$S_{o1} = G_1 S_i, \tag{A.6}$$
$$N_{o1} = G_1 N_i + N_{x1}. \tag{A.7}$$

After the second stage the energy density is given by

$$S_{o1} = G_1 G_2 S_i, \tag{A.8}$$
$$N_{o1} = G_2(G_1 N_i + N_{x1}) + N_{x2}. \tag{A.9}$$

The noise factor of the amplifer chain can be written by replace the internal noise term with noise factor using (A.5)

$$F = F_1 + \frac{F_2 - 1}{G_1}. \tag{A.10}$$

From the equation (A.10), when assembling an amplifier chain, the noise factor of the chain can be reduced by increasing the gain and decreasing the noise factor of the first stage.

A.1.2 Noise Figure Measurement by Gain Method.

A simple method to measure the Noise Factor of an amplifier is gain method using a spectrum analyzer. The input port of the amplifer is left open or connected to a 50 Ohm dummy load to eliminate the interference from stray field while the output is connect directly to the spectrum analyzer. Figure (A.1) shows the schematic digram of the setup with denotation of the input and output power density.

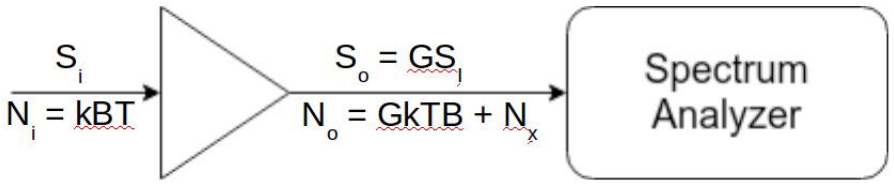

FIGURE A.1: Gain method setup: the amplifier connects directly with the spectrum analyzer to measure the noise figure.

The noise figure is given by

$$NF = 10\log(F) = 10\log N_o - 10\log G - 10\log(kT), \tag{A.11}$$

at the room temperature the noise density of the input is -174 dBm/Hz, the output noise density N_o could be obtained by using the spectrum analyzer.

A.2 Amplifier chain of WISPDMX

. The amplifier chain of WISPDMX consist of two WanTcom amplifer, the WBA0105B and the WBA0105-45R, their specifications are given in the table below:

TABLE A.1: specifications summary of two amplifiers used in WISPDMX.

	Frequency Constraints (Mhz)	Gain (dB)	Noise Figure	Noise Factor
WBA0105B	100-550	35	0.80	1.202
WBA0105-45R	150-550	44	0.50	1.122

The first stage of the amplifier chain is the WBA0105-45R due to the high gain and low noise figure, while the last stage is the WBA0105B. Using the equation (A.10), we can obtain the theoretical noise factor $F = 1.1266$ and equivalent with $NF = 0.518$.

The gain method with the spectrum analyzer can be used for the evaluation of the previous theoretical result. The noise density measured at 208 MHz give the value of $10 \log N_o = -94.40$ dBm/Hz, input noise density at the room temperature (296.35 K) $10 \log(kT) = -174$ dBm/Hz the gain at 208 Mhz is $10 \log G = 79.22$.

$$\begin{aligned} NF &= -94.40 + 174 - 79.22 \\ &= 0.38 \end{aligned}$$

The noise figure measured by the gain method is false because its value is lower than the noise figure of the first stage amplifier. The main reason is the gain method is inaccurate due to the unstable noise source.

Appendix B

Additonal Tables and Charts

TABLE B.1: The table shows different configuration of acquisition time and frequency resolution affect to the number of extended spectrum or single spectrum and output file's size.

Total Acquisition Time (seconds)	$\sum$ Samples	$\sum$ Chunks from ADC	Resolution δf(Hz)	Required Length for FFT	**N**/$\sum$ Extended Buffer/$\sum$ Single Spectrum	Noise Reducing Level by Averaging	Noise Reducing Level by δf	Total Noise Reducing Level	Output File Size
1	1 GS	100	50	20MS	50	$\sqrt{50}$	2	14.14	40 MBytes
			10	100MS	10	$\sqrt{10}$	10	31.62	200 Mbytes
10	**10GS**	**1000**	**50**	**20MS**	**500**	$\sqrt{500}$	**2**	**141.4**	**40 Mbytes**
			10	100MS	100	$\sqrt{100}$	10	316.2	200 Mbytes

TABLE B.2: The break down of time for the GPU processes.

Process	**Task**	**Time (ms)**	**Total Time (ms)**
MemcpyHtoD	Copy memory buffer from host memory to GPU	~ 2	986.6
add2array	Assembling two 10MS arrays to 20MS array	~ 0.64	322.8
cudaFFT	FFT on 20MS array under CUDA architecture	~ 1.7	851.8
add	Spectrum Stacking	~ 0.33	168
MemcpyDtoH	Copy memory buffer from GPU to host	~ 6.8	6.8
		Total time of all GPU processes	**2336**

Appendix C

Decive Specification

C.1 The Analog Digital Converter

The analog-digital converter used in WISPDMX experiment is the ATS9360[1] produced by Alazar Tech. This is a fast 12-bit waveform digitizer based on the 8-lane PCI Express Gen2 interface. The card is equipped with an onboard FPGA-FFT and boasting data throughput as fast as 3.5 GB/s (3500 MB/s) and sample rate of 1.8 GS/s across two simultaneous inputs. The primary features are listed below:

- 1.8 Giga-sample per second real-time sampling per channel
- 3.5 Gigabytes per second throughput across x8 PCIe Gen2
- 2 channels sampled at 12-bit resolution
- 4096-point on-FPGA FFT Engine
- 8 gigabytes of on-board dual-port Memory
- Variable frequency external clock capable
- Up to 800 MHz full power bandwidth
- Fixed ± 400 mV input range
- 57.1 dB SNR

[1] `http://www.alazartech.com/product/ats9360`

- Continuous streaming mode
- Trigger input and trigger output connectors
- Half-length PCIe Gen2 x8 Card
- AlazarDSO Software allows quick start-up
- Support for Windows and Linux

C.2 The Graphical Processing Unit

In our modified setup for the acquisition system, the GPU plays a role of performing a massive amount of fast Fourier transformations and returns the spectra to the memory. The graphical processing unit acquired in WISPDMX is the Nvidia GeForce GTX TITAN X[2]. The Table C.1 shows the main specification information of the GPU which are essential for the development of the acquisition. Noteworthy to mention that the GPU of 12 GB, the GPU could be able to handle a massive sample array to result in a high-resolution FFT.

[2] `https://www.geforce.com/hardware/desktop-gpus/geforce-gtx-titan-x/specifications`

Table C.1: The Nvidia TitanX Specification

Engine Specs	
CUDA Cores	3072
Base Clock (MHz)	1000
Memory Specs	
Memory Clock	7.0 Gbps
Standard Memory Config	12 GB
Memory Interface	GDDR5
Memory Bandwidth (GB/sec)	336.5
Technology Support	
OpenGL	4.5
CUDA	Yes
Bus Support	PCI Express 3.0
Thermal and Power Specs	
Maximum GPU Tempurature (in C)	91
Graphics Card Power (W)	250 W

List of Figures

List of Tables

Abbreviations

WISPDMX	**W**eakly **I**nteracting **S**lim **P**artcle **D**ark **M**atter **Ex**periment
AS	**A**cquisition **S**ystem
FCS	**F**requency **C**alibration **S**ystem
MS	**M**echanical **S**ystem
SM	The **S**tandard **M**odel of Particle Physics
BSM	**B**eyond **S**tandard **M**odels
CDM	**C**old **D**ark **M**atter

Bibliography

[1] F. Zwicky. Die Rotverschiebung von extragalaktischen Nebeln. *Helvetica Physica Acta*, 6:110–127, 1933.

[2] J. H. Oort. Some Problems Concerning the Structure and Dynamics of the Galactic System and the Elliptical Nebulae NGC 3115 and 4494. *Astrophys. J.*, 91:273, April 1940. doi: 10.1086/144167.

[3] Gianfranco Bertone, Dan Hooper, and Joseph Silk. Particle dark matter: Evidence, candidates and constraints. *Phys.Rept.*, 405:279–390, 2005. doi: 10.1016/j.physrep.2004.08.031.

[4] V. C. Rubin, Jr. W. K. Ford, and N. Thonnard. Rotational properties of 21 SC galaxies with a large range of luminosities and radii, from NGC 4605 /R = 4kpc/ to UGC 2885 /R = 122 kpc/. *Astrophys. J.*, 238:471–487, June 1980. doi: 10.1086/158003.

[5] V. C. Rubin, D. Burstein, Jr. W. K. Ford, and N. Thonnard. Rotation velocities of 16 SA galaxies and a comparison of Sa, Sb, and SC rotation properties. *Astrophys. J.*, 289:81–98, February 1985. doi: 10.1086/162866.

[6] W. Forman, E. Kellogg, H. Gursky, H. Tananbaum, and R. Giacconi. Observations of the Extended X-Ray Sources in the Perseus and Coma Clusters from UHURU. *Astrophys. J.*, 178:309–316, December 1972. doi: 10.1086/151791.

[7] H. Gursky, A. Solinger, E. M. Kellogg, S. Murray, H. Tananbaum, R. Giacconi, and A. Cavaliere. X-Ray Emission from Rich Clusters of Galaxies. *Astrophys. J. Letters*, 173:L99, May 1972. doi: 10.1086/180926.

[8] E. Kellogg, S. Murray, R. Giacconi, T. Tananbaum, and H. Gursky. Clusters of Galaxies with a Wide Range of X-Ray Luminosities. *Astrophys. J. Letters*, 185:L13, October 1973. doi: 10.1086/181311.

[9] S. W. Allen, R. W. Schmidt, H. Ebeling, A. C. Fabian, and L. van Speybroeck. Constraints on dark energy from Chandra observations of the largest relaxed galaxy clusters. *Month. Not. Roy. Astr. Soc.*, 353:457–467, September 2004. doi: 10.1111/j.1365-2966.2004.08080.x.

[10] L. J. King et al. A Complete infrared Einstein ring in the gravitational lens system B1938+666. *Mon. Not. Roy. Astron. Soc.*, 295:41, 1998. doi: 10.1046/j.1365-8711.1998.295241.x.

[11] M. Bradač, D. Clowe, A. H. Gonzalez, P. Marshall, W. Forman, C. Jones, M. Markevitch, S. Randall, T. Schrabback, and D. Zaritsky. Strong and Weak Lensing United. III. Measuring the Mass Distribution of the Merging Galaxy Cluster 1ES 0657-558. *Astrophys. J.*, 652:937–947, December 2006. doi: 10.1086/508601.

[12] D. Clowe, A. Gonzalez, and M. Markevitch. Weak-Lensing Mass Reconstruction of the Interacting Cluster 1E 0657-558: Direct Evidence for the Existence of Dark Matter. *Astrophys. J.*, 604:596–603, April 2004. doi: 10.1086/381970.

[13] George F. Smoot. The CMB spectrum. In *Current topics in astrofundamental physics. Proceedings, International School of Astrophysics *D. Chalonge*, 5th Course, Erice, Italy, September 7-15, 1996*, pages 407–440, 1997.

[14] D. J. Fixsen, E. S. Cheng, J. M. Gales, John C. Mather, R. A. Shafer, and E. L. Wright. The Cosmic Microwave Background spectrum from the full COBE FIRAS data set. *Astrophys. J.*, 473:576, 1996. doi: 10.1086/178173.

[15] C. L. Bennett, A. Banday, K. M. Gorski, G. Hinshaw, P. Jackson, P. Keegstra, A. Kogut, George F. Smoot, D. T. Wilkinson, and E. L. Wright. Four year COBE DMR cosmic microwave background observations: Maps and basic results. *Astrophys. J.*, 464:L1–L4, 1996. doi: 10.1086/310075.

[16] G. Hinshaw et al. Nine-year Wilkinson Microwave Anisotropy Probe (WMAP) Observations: Cosmological Parameter Results. *The Astrophys. J. Supp.*, 208:19, October 2013. doi: 10.1088/0067-0049/208/2/19.

[17] D. J. Fixsen, E. S. Cheng, J. M. Gales, J. C. Mather, R. A. Shafer, and E. L. Wright. The Cosmic Microwave Background Spectrum from the Full COBE FIRAS Data Set. *Astrophys. J.*, 473:576, December 1996. doi: 10.1086/178173.

[18] P. A. R. Ade et al. Planck 2015 results. XIII. Cosmological parameters. *Astron. Astrophys.*, 594:A13, 2016. doi: 10.1051/0004-6361/201525830.

[19] G. Bertone. *Particle Dark Matter*. Cambridge University Press, 2010.

[20] M.E. Peskin and D.V. Schroeder. *Introduction to Quantum Field Theory*. Westview Press, 1995.

[21] A. Zee. *Quantum Field Theory in a Nutshell*. Princeton University Press, 2 edition, 2010.

[22] W.N. Cottingham and D.A. Greenwood. *An Introduction to the Standard Model of Particle Physics*. Cambridge University Press, 2 edition, 2007.

[23] Hironari Miyazawa. Baryon Number Changing Currents*. *Progress of Theoretical Physics*, 36(6):1266–1276, 1966. doi: 10.1143/PTP.36.1266. URL `http://dx.doi.org/10.1143/PTP.36.1266`.

[24] Yu. A. Golfand and E. P. Likhtman. Extension of the Algebra of Poincare Group Generators and Violation of p Invariance. *JETP Lett.*, 13:323–326, 1971. [Pisma Zh. Eksp. Teor. Fiz.13,452(1971)].

[25] Jean-Loup Gervais and B. Sakita. Field Theory Interpretation of Supergauges in Dual Models. *Nucl. Phys.*, B34:632–639, 1971. doi: 10.1016/0550-3213(71)90351-8.

[26] J. Wess and B. Zumino. Supergauge Invariant Extension of Quantum Electrodynamics. *Nucl. Phys.*, B78:1, 1974. doi: 10.1016/0550-3213(74)90112-6.

[27] H.E. Haber and G.L. Kane. The search for supersymmetry: Probing physics beyond the standard model. *Physics Reports*, 117(2): 75–263, 1985. ISSN 0370-1573. doi: 10.1016/0370-1573(85)90051-1. URL http://www.sciencedirect.com/science/article/pii/0370157385900511.

[28] Melissa van Beekveld, Wim Beenakker, Sascha Caron, Ruud Peeters, and Roberto Ruiz de Austri. Supersymmetry with Dark Matter is still natural. *Phys. Rev.*, D96(3):035015, 2017. doi: 10.1103/PhysRevD.96.035015.

[29] Gerard Jungman, Marc Kamionkowski, and Kim Griest. Supersymmetric dark matter. *Phys. Rept.*, 267:195–373, 1996. doi: 10.1016/0370-1573(95)00058-5.

[30] Leanne D. Duffy and Karl van Bibber. Axions as Dark Matter Particles. *New J. Phys.*, 11:105008, 2009. doi: 10.1088/1367-2630/11/10/105008.

[31] Steven Weinberg. A New Light Boson? *Phys. Rev. Lett.*, 40:223–226, Jan 1978. doi: 10.1103/PhysRevLett.40.223. URL https://link.aps.org/doi/10.1103/PhysRevLett.40.223.

[32] R. D. Peccei and Helen R. Quinn. Constraints Imposed by CP Conservation in the Presence of Instantons. *Phys. Rev.*, D16:1791–1797, 1977. doi: 10.1103/PhysRevD.16.1791.

[33] R. D. Peccei and Helen R. Quinn. CP Conservation in the Presence of Instantons. *Phys. Rev. Lett.*, 38:1440–1443, 1977. doi: 10.1103/PhysRevLett.38.1440.

[34] A.A. Anselm and N.G. Uraltsev. A second massless axion? *Physics Letters B*, 114(1):39–41, 1982. ISSN 0370-2693. doi: 10.1016/0370-2693(82)90011-9. URL http://www.sciencedirect.com/science/article/pii/0370269382900119.

[35] Laura Baudis. Direct dark matter detection: the next decade. 2012. doi: 10.1016/j.dark.2012.10.006.

[36] Teresa Marrodán Undagoitia and Ludwig Rauch. Dark matter direct-detection experiments. *J. Phys.*, G43(1):013001, 2016. doi: 10.1088/0954-3899/43/1/013001.

[37] XENON100 Collaboration. The XENON100 Dark Matter Experiment. 2011. doi: 10.1016/j.astropartphys.2012.01.003.

[38] XENON100 Collaboration. Dark Matter Results from 225 Live Days of XENON100 Data. 2012. doi: 10.1103/PhysRevLett.109.181301.

[39] E. Aprile et al. The XENON1T Dark Matter Experiment. 2017.

[40] R. Agnese et al. Silicon detector results from the first five-tower run of CDMS II. *Phys. Rev. D*, 88:031104, Aug 2013. doi: 10.1103/PhysRevD.88.031104. URL `https://link.aps.org/doi/10.1103/PhysRevD.88.031104`.

[41] R. Bernabei, P. Belli, F. Montecchia, W. di Nicolantonio, A. Incicchitti, D. Prosperi, C. Bacci, C. J. Dai, L. K. Ding, H. H. Kuang, and J. M. Ma. Searching for WIMPs by the annual modulation signature. *Physics Letters B*, 424:195–201, April 1998. doi: 10.1016/S0370-2693(98)00172-5.

[42] R. Bernabei et al. Dark matter search. *Riv. Nuovo Cim.*, 26N1:1–73, 2003.

[43] R. Cerulli, P. Villar, F. Cappella, R. Bernabei, P. Belli, A. Incicchitti, A. Addazi, and Z. Berezhiani. DAMA annual modulation and mirror Dark Matter. *Eur. Phys. J.*, C77(2):83, 2017. doi: 10.1140/epjc/s10052-017-4658-3.

[44] R. Bernabei et al. DAMA/LIBRA results and perspectives. *Bled Workshops Phys.*, 17(2):1–7, 2016. doi: 10.1051/epjconf/201713605001. [EPJ Web Conf.13,60500(2017)].

[45] C. E. Aalseth et al. Results from a Search for Light-Mass Dark Matter with a P-type Point Contact Germanium Detector. 2010. doi: 10.1103/PhysRevLett.106.131301.

[46] C. E. Aalseth et al. Search for an Annual Modulation in a P-type Point Contact Germanium Dark Matter Detector. 2011. doi: 10.1103/PhysRevLett.107.141301.

[47] CDMS Collaboration. Silicon Detector Dark Matter Results from the Final Exposure of CDMS II, 2013.

[48] A. Wagner et al. A Search for Hidden Sector Photons with ADMX. *Phys. Rev. Lett.*, 105:171801, 2010. doi: 10.1103/PhysRevLett.105.171801.

[49] S. Andriamonje et al. An Improved limit on the axion-photon coupling from the CAST experiment. *JCAP*, 0704:010, 2007. doi: 10.1088/1475-7516/2007/04/010.

[50] K. Zioutas et al. First results from the CERN Axion Solar Telescope (CAST). *Phys. Rev. Lett.*, 94:121301, 2005. doi: 10.1103/PhysRevLett.94.121301.

[51] M. Arik, T. Vafeiadis, J. A. Villar, J. K. Vogel, S. C. Yildiz, et al. Search for Sub-eV Mass Solar Axions by the CERN Axion Solar Telescope with ^{3}He Buffer Gas. *Phys. Rev. Lett.*, 107:261302, Dec 2011. doi: 10.1103/PhysRevLett.107.261302. URL `https://link.aps.org/doi/10.1103/PhysRevLett.107.261302`.

[52] Matthias Schwarz, Ernst-Axel Knabbe, Axel Lindner, Javier Redondo, Andreas Ringwald, Magnus Schneide, Jaroslaw Susol, and Günter Wiedemann. Results from the Solar Hidden Photon Search (SHIPS). *JCAP*, 1508(08): 011, 2015. doi: 10.1088/1475-7516/2015/08/011.

[53] M. Ackermann et al. Limits on Dark Matter Annihilation Signals from the Fermi LAT 4-year Measurement of the Isotropic Gamma-Ray Background. *JCAP*, 1509(09):008, 2015. doi: 10.1088/1475-7516/2015/09/008.

[54] J. Majumdar, F. Calore, and D. Horns. Gamma-ray spectral modulations of Galactic pulsars caused by photon-ALPs mixing. *ArXiv e-prints*, January 2018.

[55] Knut Morå. Dark Matter Searches with H.E.S.S. In *27th Rencontres de Blois on Particle Physics and Cosmology Blois, France, May 31-June 5, 2015*, 2015. URL `https://inspirehep.net/record/1407811/files/arXiv:1512.00698.pdf`.

[56] S. Lombardi, J. Aleksic, J. A. Barrio, A. Biland, M. Doro, D. Elsaesser, M. Gaug, K. Mannheim, M. Mariotti, M. Martinez, D. Nieto, M. Persic, F. Prada, J. Rico, M. Rissi, M. A. Sanchez-Conde, L. S. Stark, F. Zandanel, and for the MAGIC Collaboration. Search for Dark Matter signatures with MAGIC-I and prospects for MAGIC Phase-II. *ArXiv e-prints*, July 2009.

[57] B. Zitzer. The VERITAS Dark Matter Program. In *5th International Fermi Symposium Nagoya, Japan, October 20-24, 2014*, 2015. URL `https://inspirehep.net/record/1347106/files/arXiv:1503.00743.pdf`.

[58] M. G. Aartsen et al. First search for dark matter annihilations in the Earth with the IceCube Detector. *Eur. Phys. J.*, C77(2):82, 2017. doi: 10.1140/epjc/s10052-016-4582-y.

[59] M. G. Aartsen et al. Search for Neutrinos from Dark Matter Self-Annihilations in the center of the Milky Way with 3 years of IceCube/DeepCore. *Eur. Phys. J.*, C77(9):627, 2017. doi: 10.1140/epjc/s10052-017-5213-y.

[60] J. D. Zornoza and C. Toennis. Results of dark matter searches with the ANTARES neutrino telescope. *J. Phys. Conf. Ser.*, 888(1):012206, 2017. doi: 10.1088/1742-6596/888/1/012206.

[61] V. Barger, Wai Yee Keung, D. Marfatia, and G. Shaughnessy. PAMELA and dark matter. *Phys. Lett.*, B672:141–146, 2009. doi: 10.1016/j.physletb.2009.01.016.

[62] B Beischer, P von Doetinchem, H Gast, T Kirn, and S Schael. Perspectives for indirect dark matter search with AMS-2 using cosmic-ray electrons and

positrons. *New Journal of Physics*, 11(10):105021, 2009. URL http://stacks.iop.org/1367-2630/11/i=10/a=105021.

[63] P. Aguilar and C. Zurbach. First Result from the Alpha Magnetic Spectrometer on the International Space Station: Precision Measurement of the Positron Fraction in Primary Cosmic Rays of 0.5˘350 GeV. *Phys. Rev. Lett.*, 110:141102, Apr 2013. doi: 10.1103/PhysRevLett.110.141102. URL https://link.aps.org/doi/10.1103/PhysRevLett.110.141102.

[64] Anne M. Green. Astrophysical uncertainties on direct detection experiments. *Mod. Phys. Lett.*, A27:1230004, 2012. doi: 10.1142/S0217732312300042.

[65] F. J. Kerr and D. Lynden-Bell. Review of galactic constants. *Month. Not. Roy. Astr. Soc.*, 221:1023–1038, August 1986. doi: 10.1093/mnras/221.4.1023.

[66] Martin C. Smith et al. The RAVE Survey: Constraining the Local Galactic Escape Speed. *Mon. Not. Roy. Astron. Soc.*, 379:755–772, 2007. doi: 10.1111/j.1365-2966.2007.11964.x.

[67] J I Read. The local dark matter density. *Journal of Physics G: Nuclear and Particle Physics*, 41(6):063101, 2014. URL http://stacks.iop.org/0954-3899/41/i=6/a=063101.

[68] A. Pillepich, M. Kuhlen, J. Guedes, and P. Madau. The Distribution of Dark Matter in the Milky Way's Disk. *ApJ*, 784:161, April 2014. doi: 10.1088/0004-637X/784/2/161.

[69] Diemand J., Kuhlen M., Madau P., Zemp M., Moore B., Potter D., and Stadel J. Clumps and streams in the local dark matter distribution. *Nature*, 454:735, aug 2008. doi: 10.1038/nature07153. URL https://www.nature.com/articles/nature07153#supplementary-information.

[70] Joachim Stadel, Doug Potter, Ben Moore, Jurg Diemand, Piero Madau, Marcel Zemp, Michael Kuhlen, and Vicent Quilis. Quantifying the heart of

darkness with GHALO - a multi-billion particle simulation of our galactic halo. *Mon. Not. Roy. Astron. Soc.*, 398:L21–L25, 2009. doi: 10.1111/j.1745-3933.2009.00699.x.

[71] Julio F. Navarro, Carlos S. Frenk, and Simon D. M. White. The Structure of cold dark matter halos. *Astrophys. J.*, 462:563–575, 1996. doi: 10.1086/177173.

[72] Volker Springel et al. Simulating the joint evolution of quasars, galaxies and their large-scale distribution. *Nature*, 435:629–636, 2005. doi: 10.1038/nature03597.

[73] Julio F. Navarro, Vincent R. Eke, and Carlos S. Frenk. The cores of dwarf galaxy halos. *Mon. Not. Roy. Astron. Soc.*, 283:L72–L78, 1996.

[74] M. Tremmel, M. Karcher, F. Governato, M. Volonteri, T. R. Quinn, A. Pontzen, L. Anderson, and J. Bellovary. The Romulus cosmological simulations: a physical approach to the formation, dynamics and accretion models of SMBHs. *Month. Not. Roy. Astr. Soc.*, 470:1121–1139, September 2017. doi: 10.1093/mnras/stx1160.

[75] Joerg Jaeckel. A force beyond the Standard Model - Status of the quest for hidden photons. *Frascati Phys. Ser.*, 56:172–192, 2012.

[76] L. B. Okun. LIMITS OF ELECTRODYNAMICS: PARAPHOTONS? *Sov. Phys. JETP*, 56:502, 1982. [Zh. Eksp. Teor. Fiz.83,892(1982)].

[77] Bob Holdom. Two U(1)'s and Epsilon Charge Shifts. *Phys. Lett.*, 166B: 196–198, 1986. doi: 10.1016/0370-2693(86)91377-8.

[78] Joerg Jaeckel and Sabyasachi Roy. Spectroscopy as a test of Coulomb's law: A Probe of the hidden sector. *Phys. Rev.*, D82:125020, 2010. doi: 10.1103/PhysRevD.82.125020.

[79] E. R. Williams, J. E. Faller, and H. A. Hill. New Experimental Test of Coulomb's Law: A Laboratory Upper Limit on the Photon Rest Mass. *Phys.*

Rev. Lett., 26:721–724, Mar 1971. doi: 10.1103/PhysRevLett.26.721. URL https://link.aps.org/doi/10.1103/PhysRevLett.26.721.

[80] V. Popov. On the experimental search for photon mixing. *Turkish Journal of Physics*, 23:943–950, May 1999.

[81] S. G. Karshenboim. Constraints on a long-range spin-independent interaction from precision atomic physics. *Phys. Rev.*, D82:073003, 2010. doi: 10.1103/PhysRevD.82.073003.

[82] S. G. Karshenboim. Precision physics of simple atoms and constraints on a light boson with ultraweak coupling. *Phys. Rev. Lett.*, 104:220406, 2010. doi: 10.1103/PhysRevLett.104.220406.

[83] Maurizio Giannotti, Igor Irastorza, Javier Redondo, and Andreas Ringwald. Cool WISPs for stellar cooling excesses. *JCAP*, 1605(05):057, 2016. doi: 10.1088/1475-7516/2016/05/057.

[84] Howard Georgi, Paul H. Ginsparg, and S. L. Glashow. Photon Oscillations and the Cosmic Background Radiation. *Nature*, 306:765–766, 1983. doi: 10.1038/306765a0.

[85] L. Wolfenstein. Neutrino Oscillations in Matter. *Phys. Rev.*, D17:2369–2374, 1978. doi: 10.1103/PhysRevD.17.2369.

[86] Alessandro Mirizzi, Javier Redondo, and Gunter Sigl. Microwave Background Constraints on Mixing of Photons with Hidden Photons. *JCAP*, 0903:026, 2009. doi: 10.1088/1475-7516/2009/03/026.

[87] Cameron Mahoney, Adam K. Leibovich, and Andrew R. Zentner. Updated Constraints on Self-Interacting Dark Matter from Supernova 1987A. *Phys. Rev.*, D96(4):043018, 2017. doi: 10.1103/PhysRevD.96.043018.

[88] H. Merkel et al. Search for Light Gauge Bosons of the Dark Sector at the Mainz Microtron. *Phys. Rev. Lett.*, 106:251802, 2011. doi: 10.1103/PhysRevLett.106.251802.

[89] S. Abrahamyan et al. Search for a New Gauge Boson in Electron-Nucleus Fixed-Target Scattering by the APEX Experiment. *Phys. Rev. Lett.*, 107: 191804, 2011. doi: 10.1103/PhysRevLett.107.191804.

[90] Sarah Andreas. Hidden Photons in beam dump experiments and in connection with Dark Matter. *Frascati Phys. Ser.*, 56:23–32, 2012.

[91] Sarah Andreas, Carsten Niebuhr, and Andreas Ringwald. New Limits on Hidden Photons from Past Electron Beam Dumps. *Phys. Rev.*, D86:095019, 2012. doi: 10.1103/PhysRevD.86.095019.

[92] T. Mizumoto, R. Ohta, T. Horie, J. Suzuki, Y. Inoue, and M. Minowa. Experimental search for solar hidden photons in the eV energy range using kinetic mixing with photons. *JCAP*, 1307:013, 2013. doi: 10.1088/1475-7516/2013/07/013.

[93] R. Horvat, D. Kekez, M. Krcmar, Z. Krecak, and A. Ljubicic. Constraining solar hidden photons using HPGe detector. *Phys. Lett.*, B721:220–223, 2013. doi: 10.1016/j.physletb.2013.03.014.

[94] Javier Redondo. Helioscope Bounds on Hidden Sector Photons. *JCAP*, 0807: 008, 2008. doi: 10.1088/1475-7516/2008/07/008.

[95] M. Ahlers, H. Gies, J. Jaeckel, J. Redondo, and A. Ringwald. Laser experiments explore the hidden sector. *Phys. Rev.*, D77:095001, 2008. doi: 10.1103/PhysRevD.77.095001.

[96] A. Afanasev, O. K. Baker, K. B. Beard, G. Biallas, J. Boyce, M. Minarni, R. Ramdon, M. Shinn, and P. Slocum. New Experimental Limit on Photon Hidden-Sector Paraphoton Mixing. *Phys. Lett.*, B679:317–320, 2009. doi: 10.1016/j.physletb.2009.07.055.

[97] Klaus Ehret et al. New ALPS Results on Hidden-Sector Lightweights. *Phys. Lett.*, B689:149–155, 2010. doi: 10.1016/j.physletb.2010.04.066.

[98] Rhys Povey, John Hartnett, and Michael Tobar. Microwave cavity light shining through a wall optimization and experiment. *Phys. Rev.*, D82:052003, 2010. doi: 10.1103/PhysRevD.82.052003.

[99] Dieter Horns, Joerg Jaeckel, Axel Lindner, Andrei Lobanov, Javier Redondo, and Andreas Ringwald. Searching for WISPy Cold Dark Matter with a Dish Antenna. *JCAP*, 1304:016, 2013. doi: 10.1088/1475-7516/2013/04/016.

[100] Jun'ya Suzuki, Yoshizumi Inoue, Tomoki Horie, and Makoto Minowa. Hidden photon CDM search at Tokyo. In *Proceedings, 11th Patras Workshop on Axions, WIMPs and WISPs (Axion-WIMP 2015): Zaragoza, Spain, June 22-26, 2015*, pages 145–148, 2015. doi: 10.3204/DESY-PROC-2015-02/junya_suzuki. URL `https://inspirehep.net/record/1391489/files/arXiv:1509.00785.pdf`.

[101] R. Engel et al. Search for hidden-photon Dark Matter with FUNK. In *13th Patras Workshop on Axions, WIMPs and WISPs (AXION-WIMP 2017) CHALKIDIKI TBC, GREECE, May 15-19, 2017*, 2017. URL `https://inspirehep.net/record/1634977/files/arXiv:1711.02961.pdf`.

[102] Paola Arias, Davide Cadamuro, Mark Goodsell, Joerg Jaeckel, Javier Redondo, and Andreas Ringwald. WISPy Cold Dark Matter. *JCAP*, 1206:013, 2012. doi: 10.1088/1475-7516/2012/06/013.

[103] P. Sikivie. Experimental Tests of the "Invisible" Axion. *Phys. Rev. Lett.*, 51:1415–1417, Oct 1983. doi: 10.1103/PhysRevLett.51.1415. URL `https://link.aps.org/doi/10.1103/PhysRevLett.51.1415`.

[104] M. S. Turner. Periodic signatures for the detection of cosmic axions. *Pys. Rev. D*, 42:3572–3575, November 1990. doi: 10.1103/PhysRevD.42.3572.

[105] C. A. J. O'Hare and A. M. Green. Axion astronomy with microwave cavity experiments. *Phys. Rev. D*, 95(6):063017, March 2017. doi: 10.1103/PhysRevD.95.063017.

[106] K. Griest. Effect of the Sun's gravity on the distribution and detection of dark matter near the Earth. *Phys. Rev. D*, 37:2703–2713, May 1988. doi: 10.1103/PhysRevD.37.2703.

[107] P. R. Kafle, S. Sharma, G. F. Lewis, and J. Bland-Hawthorn. On the Shoulders of Giants: Properties of the Stellar Halo and the Milky Way Mass Distribution. *ApJ*, 794:59, October 2014. doi: 10.1088/0004-637X/794/1/59.

[108] G Rogner. *Study of the mechanical design of 200 MHz single-cell cavities for application in the SPS*. CERN, Geneva, 1980. URL `http://cds.cern.ch/record/125024`.

[109] V Rödel. Higher-order modes and tuning of the SPS 200 MHz single-cell cavity. Technical Report CERN-SL-RFS-Note-91-08. SL-RFS-Note-91-08, CERN, Geneva, Nov 1991. URL `http://cds.cern.ch/record/703160`.

[110] Alexander Gamp. THE RADIOFREQUENCY SYSTEMS AND CONTROL OF THE HERA PROTON BEAM. *Part. Accel.*, 29:65–70, 1990.

[111] P. J. Petersan and S. M. Anlage. Measurement of resonant frequency and quality factor of microwave resonators: Comparison of methods. *Journal of Applied Physics*, 84:3392–3402, September 1998. doi: 10.1063/1.368498.

Acknowledgements

My sincere gratitude is to my supervisor, Prof. Dr. Dieter Horns, for his ideas on the experiment development, opportunities to additional projects and studies. They do help me to amass new knowledge, skills, and make me a better experimentalist. I have to thank Dieter again for pushing me down into the labyrinth so that I know I have to make wings.

My thanks to Dr. Andrei Lobanov for his discussions and contributions on the theoretical aspects which make WISPDMX "great again" with the ability to constrain the off-resonance regions. Especially for his endless patience in explaining and showing me what should be done rightly.

On the experimental side, my great thank to Dr. Martin Tluczykont for his supports and discussions about the technical obstacles in the lab, his advice on how to deal with academic problems, and for always reminding me to shock my muscles.

My super-super-super huge thank to the members of the working group for always helping and supporting me for the last three years, without you guys, my Ph.D. student's life would not be lively. My special thanks to Jhilik Majumdar for the being the best conference-mate and her openness on technical problems, without them I would not learn something new. An "okay, thank you!" to the two bright bachelor students Ali and Henrik for their presence and lame jokes during the thesis writing breaks.

Kudos to Martin and Jhilik for proofreading my thesis, you guys did a fantastic job!

My deepest and sincere thank to my family, for reminding me that I always have a home to come back, and encouraging me from 10000 miles away. For constantly pushing me away so I could define myself and follow my plan without looking back. Because I know they are here with me, in my heart. Always.

Thank you, em.

Eidesstattliche Versicherung

Declaration on oath

Hiermit erklare ich an Eides statt, dass ich die vorliegende Dissertationsschrift selbst verfasst und keine anderen als die angegebenen Quellen und Hilfsmittel benutzt habe.
I hereby declare, on oath, that I have written the present dissertation by my own and have not used other than the acknowledged resources and aids.

Hamburg
5th March, 2018
Unterschrift

Le Hoang Nguyen